

71-7337

TURNER, Jr., Charles Edward, 1940-  
LIFETIMES OF THE FIRST EXCITED STATES IN  $TM^{169}$ ,  
 $TM^{171}$ , AND  $CS^{134}$ .

Iowa State University, Ph.D., 1970  
Physics, nuclear

University Microfilms, Inc., Ann Arbor, Michigan

LIFETIMES OF THE FIRST EXCITED  
STATES IN  $\text{TM}^{169}$ ,  $\text{TM}^{171}$ , AND  $\text{CS}^{134}$

by

Charles Edward Turner, Jr.

A Dissertation Submitted to the  
Graduate Faculty in Partial Fulfillment of  
The Requirements for the Degree of  
DOCTOR OF PHILOSOPHY

Major Subject: Nuclear Physics

Approved:

Signature was redacted for privacy.

In Charge of Major Work

Signature was redacted for privacy.

Head of ~~Major~~ Department

Signature was redacted for privacy.

~~Dean~~ of Graduate College

Iowa State University  
Of Science and Technology  
Ames, Iowa

1970

## TABLE OF CONTENTS

|  | Page |
|--|------|
| I. INTRODUCTION  | 1    |
| II. THEORY   | 6    |
| III. EXPERIMENTAL TECHNIQUES   | 14   |
| A. Principal Constituents of Delayed-Coincidence Apparatus                   | 15   |
| B. Review of Delayed-Coincidence Systems Used With Very-Low-Energy Radiation | 18   |
| 1. Back-to-back scintillation detectors                                      | 18   |
| 2. Avalanche counter opposite scintillation detector                         | 18   |
| 3. Magnetic spectrometer opposite scintillation detector                     | 19   |
| 4. Back-to-back magnetic spectrometers                                       | 20   |
| C. Apparatus   | 21   |
| D. Experimental Procedure  | 32   |
| 1. Source preparation  | 33   |
| 2. Preacceleration technique   | 37   |
| 3. Energy resolution   | 44   |
| 4. Electron detection  | 47   |
| 5. Time pickoff method   | 49   |
| 6. Time resolution   | 55   |
| 7. Time calibration  | 61   |
| 8. Nonlinearity measurement and correction                                   | 64   |
| 9. Data analysis   | 66   |
| IV. EXPERIMENTAL HALF-LIFE RESULTS   | 71   |
| A. The 8.4-keV Level in $\text{Tm}^{169}$                                    | 71   |
| B. The 5.0-keV Level in $\text{Tm}^{171}$                                    | 90   |
| C. The 11-keV Level in $\text{Cs}^{134}$                                     | 107  |

|  |     |
|--|-----|
| D. Indication of a Systematic Discrepancy  | 116 |
| V. DISCUSSION OF THE RESULTS   | 119 |
| A. The $K = 1/2$ Rotational Bands  | 119 |
| 1. The 8.4-keV level in $\text{Tm}^{169}$  | 121 |
| 2. The 5.0-keV level in $\text{Tm}^{171}$  | 124 |
| 3. The utility of better accuracy  | 125 |
| 4. Some especially desirable measurements  | 129 |
| B. The Odd-Odd Nucleus $\text{Cs}^{134}$   | 130 |
| VI. BIBLIOGRAPHY   | 131 |
| VII. ACKNOWLEDGEMENTS  | 138 |
| VIII. APPENDIX A: CALIBRATION OF THE SPECTROMETER                                | 140 |
| IX. APPENDIX B: CALIBRATION OF THE HIGH VOLTAGE SUPPLY                           | 143 |
| X. APPENDIX C: ESTIMATION OF TRANSIT TIME DISPERSION IN A CYLINDRICAL LIGHT PIPE | 145 |
| XI. APPENDIX D: DEPENDENCE OF THE HALF-LIFE ON PREACCELERATION VOLTAGE           | 148 |

## LIST OF FIGURES

|  | Page |
|--|------|
| Fig. 1. Schematic cross section of the intermediate-image beta-ray spectrometers.  | 22   |
| Fig. 2a. Delayed-coincidence system.   | 23   |
| Fig. 2b. Delayed-coincidence system (continued).   | 24   |
| Fig. 2c. Delayed-coincidence system (continued).   | 25   |
| Fig. 3. Schematic diagram of the source end of the insulated source holder rod.  | 41   |
| Fig. 4. Low energy portions of the electron spectra obtained from the $\text{Yb}^{169}$ (a), $\text{Er}^{171}$ (b), and $\text{Cs}^{134\text{m}}$ (c) decays.  | 42   |
| Fig. 5. Comparison of the influence of the source shield screen on spectrometer transmission at different energies.  | 43   |
| Fig. 6. Pulse height distributions obtained with electrons of different energy.  | 50   |
| Fig. 7. Pulse height distributions in the low energy channel with different gating modes.  | 52   |
| Fig. 8. Pulse height distributions in the high energy channel with different gating modes.   | 53   |
| Fig. 9. Optimum low energy $e^- - e^-$ prompt coincidence distribution.  | 58   |
| Fig. 10. A portion of the electron spectrum obtained from the $\text{Yb}^{169}$ decay and a partial decay scheme of the $\text{Yb}^{169}$ and $\text{Er}^{169}$ decays.                                  | 72   |
| Fig. 11. Delay curve for the 8.4-keV level in $\text{Tm}^{169}$ via the 8N and 110K transitions in the $\text{Yb}^{169}$ decay.  | 76   |
| Fig. 12. Delay curve for the 8.4-keV level in $\text{Tm}^{169}$ via the 8M and 110K transitions in the $\text{Yb}^{169}$ decay.  | 77   |
| Fig. 13. Delay curve for the 8.4-keV level in $\text{Tm}^{169}$ via the 8M and 110L transitions in the $\text{Yb}^{169}$ decay.  | 78   |
| Fig. 14. Delay curve for the 8.4-keV level in $\text{Tm}^{169}$ via the 8M transition and betas in the $\text{Er}^{169}$ decay.  | 79   |
| Fig. 15. Delay curve for the 8.4-keV level in $\text{Tm}^{169}$ via the 8M and 110L transitions in the $\text{Yb}^{169}$ decay and a corresponding prompt curve via the 110K and 198K transitions in the | 80   |

|          |  |     |
|----------|--|-----|
|          | $\text{Yb}^{169}$ decay.   |     |
| Fig. 16. | Delay curve for the 8.4-keV level in $\text{Tm}^{169}$ via the 8M transition and betas in the $\text{Er}^{169}$ decay and a corresponding prompt curve via the 110K and 198K transitions in the $\text{Yb}^{169}$ decay. | 81  |
| Fig. 17. | Comparison of the half-life values of the 8.4-keV level in $\text{Tm}^{169}$ reported by different experimenters.  | 87  |
| Fig. 18. | A portion of the electron spectrum obtained from the $\text{Er}^{171}$ decay and a partial decay scheme of the $\text{Er}^{171}$ decay.  | 91  |
| Fig. 19. | Delay curve for the 5.0-keV level in $\text{Tm}^{171}$ via the 5N and 112K transitions in the $\text{Er}^{171}$ decay.   | 95  |
| Fig. 20. | Delay curve for the 5.0-keV level in $\text{Tm}^{171}$ via the 5M and 112K transitions in the $\text{Er}^{171}$ decay.   | 96  |
| Fig. 21. | Delay curve for the 5.0-keV level in $\text{Tm}^{171}$ via the 5M and 112L transitions in the $\text{Er}^{171}$ decay.   | 97  |
| Fig. 22. | Delay curve for the 5.0-keV level in $\text{Tm}^{171}$ via the 5N and 112L transitions in the $\text{Er}^{171}$ decay.   | 98  |
| Fig. 23. | A "worst case" delay curve for the 5.0-keV level in $\text{Tm}^{171}$ via the 5N and 112K transitions in the $\text{Er}^{171}$ decay.  | 99  |
| Fig. 24. | Delay curve for the 5.0-keV level in $\text{Tm}^{171}$ via the 5M and 112K transitions in the $\text{Er}^{171}$ decay and a corresponding prompt curve via the 21L and 110K transitions in the $\text{Yb}^{169}$ decay.  | 100 |
| Fig. 25. | Comparison of the half-life values of the 5.0-keV level in $\text{Tm}^{171}$ reported by different experimenters.  | 106 |
| Fig. 26. | An electron spectrum obtained from the $\text{Cs}^{134m}$ decay  | 108 |
| Fig. 27. | Delay curve for the 11-keV level in $\text{Cs}^{134}$ via the 11L and 127L transitions in the $\text{Cs}^{134m}$ decay.  | 110 |
| Fig. 28. | Comparison of the half-life values of the 11-keV level in $\text{Cs}^{134}$ reported by different experimenters.   | 114 |
| Fig. 29. | Discrepancies between the measurements by Blechschmidt <u>et al.</u> and the present measurements.   | 117 |

Fig. 30. Low-energy-channel spectrometer energy-calibration spectrum.

142

## LIST OF TABLES

|   | Page |
|---|------|
| Table 1. Source, conversion line, and preacceleration voltage information for the prompt- and delay-data tags associated with the 8-keV level in $\text{Tm}^{169}$  | 74   |
| Table 2. Summary of quantities calculated in the maximum-likelihood unfolding analysis of delayed-coincidence distributions involving the lifetime of the 8-keV level in $\text{Tm}^{169}$ obtained from the $\text{Yb}^{169}$ and $\text{Er}^{169}$ decays   | 75   |
| Table 3. Summary of quantities calculated in the maximum-likelihood fit of an exponential plus constant background to the tail portion of delayed-coincidence distributions involving the lifetime of the 8-keV level in $\text{Tm}^{169}$ obtained from the $\text{Yb}^{169}$ and $\text{Er}^{169}$ decays                       | 83   |
| Table 4. Summary of quantities calculated in the linear least-squares fit to the logarithms of the tail portion, after subtraction of a constant background, of delayed-coincidence distributions involving the lifetime of the 8-keV level in $\text{Tm}^{169}$ obtained from the $\text{Yb}^{169}$ and $\text{Er}^{169}$ decays | 84   |
| Table 5. Comparison of the average half-life values and statistical quantities associated with the different analysis procedures for the ten delayed-coincidence distributions involving the lifetime of the 8-keV level in $\text{Tm}^{169}$   | 85   |
| Table 6. Half-life values of the 8.4-keV level in $\text{Tm}^{169}$ reported by different experimenters   | 88   |
| Table 7. Source, conversion line, and preacceleration voltage information for the prompt- and delay-data tags associated with the 5-keV level in $\text{Tm}^{171}$  | 93   |
| Table 8. Summary of quantities calculated in the maximum-likelihood unfolding analysis of delayed-coincidence distributions involving the lifetime of the 5-keV   | 94   |



|           |  |     |
|-----------|--|-----|
|           | level in $\text{Tm}^{171}$ obtained from the $\text{Er}^{171}$ decay   |     |
| Table 9.  | Summary of quantities calculated in the maximum-likelihood fit of an exponential plus constant background to the tail portion of delayed-coincidence distributions involving the lifetime of the 5-keV level in $\text{Tm}^{171}$ obtained from the $\text{Er}^{171}$ decay                                | 101 |
| Table 10. | Summary of quantities calculated in the linear least-squares fit to the logarithms of the tail portion, after subtraction of a constant background, of delayed-coincidence distributions involving the lifetime of the 5-keV level in $\text{Tm}^{171}$ obtained from the $\text{Er}^{171}$ decay          | 103 |
| Table 11. | Comparison of the average half-life values and statistical quantities associated with the different analysis procedures for the eleven delayed-coincidence distributions involving the lifetime of the 5-keV level in $\text{Tm}^{171}$  | 104 |
| Table 12. | Half-life values of the 5.0-keV level in $\text{Tm}^{171}$ reported by different experimenters   | 105 |
| Table 13. | Summary of quantities calculated in the maximum-likelihood fit of an exponential plus constant background to the tail portion of delayed-coincidence distributions involving the lifetime of the 11-keV level in $\text{Cs}^{134}$ obtained from the $\text{Cs}^{134\text{m}}$ decay                       | 109 |
| Table 14. | Summary of quantities calculated in the linear least-squares fit to the logarithms of the tail portion, after subtraction of a constant background, of delayed-coincidence distributions involving the lifetime of the 11-keV level in $\text{Cs}^{134}$ obtained from the $\text{Cs}^{134\text{m}}$ decay | 109 |
| Table 15. | Comparison of the average half-life values and statistical quantities associated with the different analysis procedures for the four delayed-coincidence   | 112 |

|           |   |     |
|-----------|---|-----|
|           | distributions involving the lifetime of the 11-keV level in Cs <sup>134</sup>   |     |
| Table 16. | Half-life values of the 11-keV level in Cs <sup>134</sup> reported by different experimenters   | 115 |
| Table 17. | Ratios of the half-life values obtained by Blechschmidt <u>et al.</u> (94) to the corresponding values obtained in the present investigation  | 118 |
| Table 18. | The "best-fit" electromagnetic parameters of the $K = 1/2$ ground state rotational band in Tm <sup>169</sup> and Tm <sup>171</sup> obtained by Kaufmann <u>et al.</u> (99) with no quadrupole moment correction | 123 |

## I. INTRODUCTION

It is not presently feasible to formulate a unified microscopic theory of nuclear matter from which the structure and properties of all nuclei can be calculated since the quantum mechanical many-body problem is not exactly soluble even if the exact internucleonic forces were available. Nuclear physicists have, therefore, resorted to the macroscopic approach of developing models having limited accuracy and applicability due to strong simplifying assumptions about nuclear structure. Such models not only are capable of systematizing a large amount of the experimental information but also give information about the relative importance of various possible physical mechanisms which can influence nuclear structure.

The fundamental problem in the formulation of a quantum mechanical model for a particular class of nuclei is the choice of a Hamiltonian which reflects the most important physical mechanisms responsible for the energy of the nuclear system in its principal modes of excitation and for which the energy eigenvalue problem expressed by the Schroedinger equation is solvable. It often happens that the excitation spectra predicted by models emphasizing different plausible physical mechanisms give comparable agreement with the observed excited states. In order to decide which model is more suitable it is necessary to compare with experimental values the theoretically predicted expectation values of operators corresponding to physically observable quantities such as electric and magnetic multipole moments or transition probabilities between the excited states. Such a comparison provides a critical test of

the validity of a particular nuclear model since the calculated values of such observables depend intimately on the nature of the wave functions which are obtained from the solution of the eigenvalue problem and which, therefore, contain the detailed nuclear structure information. The gamma-decay transition probability is particularly important for model validity determination because the experimental data are generally more numerous, more accurate, and more easily obtained and because the interaction operator responsible for emission of electromagnetic radiation is well known (in contrast to beta decay, for example). Thus a very important element in the testing of nuclear models is the measurement of nuclear lifetimes from which the gamma-ray transition probabilities can be calculated if the total internal conversion coefficients, mixing ratios, and branching ratios are known.

The unified nuclear model developed by Bohr, Mottelson, and Nilsson has generally been considered to be the most powerful model for description of the collective and intrinsic excitations of deformed nuclei. Of special interest are odd mass nuclei possessing rotational bands with  $K = 1/2$  since in these cases additional matrix elements originating from the "Coriolis" interaction and depending on the intrinsic nuclear structure appear in the expressions for the rotational energy spectrum and intraband magnetic-dipole transition probability.

$^{169}\text{Tm}$  and  $^{171}\text{Tm}$  are among the best candidates for testing the rotational model since:

- 1) they are in the center of the deformed region ( $150 \leq A \leq 190$ ),
- 2) they both possess  $K = 1/2$  rotational bands based on the in-

trinsic Nilsson orbital  $1/2 + [411]^1$ , which is also the ground state thereby making experimental investigation easier,

3)  $\text{Tm}^{169}$  is one of the most intensively studied odd nuclei, and

4)  $\text{Tm}^{171}$ , which is less well studied because of the short parent half-life ( $\text{Er}^{171}$ ,  $T_{1/2} = 7.5\text{h}$ ), has been subjected to more careful investigation recently. In addition the structure of these nuclei, which have considerable similarity, differs in some details which are not easily explained by a simple change in deformation. These differences may possibly be used to investigate the interaction of the odd proton and the added neutrons. It is, therefore, desirable to have the most accurate experimental information possible concerning the electromagnetic properties of these two nuclei. Unfortunately there was annoying disagreement for a long time among at least seven independent determinations of the half-life of the first excited state in  $\text{Tm}^{169}$ . In addition there was disagreement between two determinations, both of which were suspected to be erroneous, of the half-life of the first excited state in  $\text{Tm}^{171}$ .

The present investigation deals primarily with the measurement of the lifetimes of the very-low-energy ( $< 11\text{ keV}$ ) first excited states in  $\text{Tm}^{169}$  and  $\text{Tm}^{171}$ . The experimental objective was to investigate, estimate,

---

<sup>1</sup>The notation  $K\pi[N, n_z, \Lambda]$  is used to designate the single-particle states in a non-spherical well. The projection of the total angular momentum on the nuclear symmetry axis is indicated by  $K$ . The parity is  $\pi = \pm$ . The quantum numbers inside the square brackets are the "asymptotic" quantum numbers which would characterize these states in the limit where the nuclear potential becomes a very anisotropic, axially symmetric, harmonic oscillator. These quantum numbers are  $N$ , the total number of modes in the wave function,  $n_z$ , the number of nodal planes perpendicular to the symmetry axis, and  $\Lambda$ , the component of the particle's orbital angular momentum along the symmetry axis.

and/or eliminate as far as possible the most likely sources of systematic error in order to be able to make accurate and convincing determinations of these lifetimes. The observation of an apparent systematic discrepancy with the measurements of one group of experimenters led to the determination of the lifetime of the 11-keV first excited state in  $\text{Cs}^{134}$  as well.

In Section II are presented the basic assumptions and results of the unified nuclear model which are relevant to the discussion of the  $\text{Tm}^{169}$  and  $\text{Tm}^{171}$  lifetime measurements. In addition the relationship between the gamma-ray transition probability and experimental half-life is discussed.

In Section III, experimental techniques are discussed. Subsection A. gives a brief consideration of the constituents of a general delayed-coincidence apparatus. In Subsection B. examples are given for comparison purposes of a few experimental configurations that have been applied to cases similar to those investigated in this work. Subsection C. describes the apparatus used in the present work. The specifications of important elements of the system are given. The rather sophisticated electronic logic system which provided the pileup rejection, digital stabilization, and semiautomatic electronic calibration in conjunction with the basic time-interval measurement capability is described. Finally, Subsection D. describes the experimental procedure used. Several aspects of the measurement process are examined and the considerable care exercised to avoid systematic errors is indicated.

Section IV presents the experimental results of the measurement of the lifetimes of the first excited states in  $\text{Tm}^{169}$ ,  $\text{Tm}^{171}$  and  $\text{Cs}^{134}$ .

Electron spectra and typical delayed-coincidence distributions are displayed. The results obtained by different analysis techniques are compared. The assignment of the adopted values and their errors is discussed. The final results are compared to those of previous investigations and possible causes for the observed discrepancies are mentioned. One indication of systematic discrepancy which reinforces the validity of the present measurements is indicated.

In Section V the experimental results for  $\text{Tm}^{169}$  and  $\text{Tm}^{171}$  are compared to those predicted on the basis of the theoretical parameters determined by a recent least-squares fit to the experimental data. The general utility of more accurate determination of the electromagnetic properties of the  $K = 1/2$  rotational band to other theoretical calculations is indicated. Furthermore, the desirability and feasibility of measurements of better accuracy for the lifetimes of the higher excited states in the two Tm isotopes is noted. Also a recent calculation of the lifetime of the 11-keV level in  $\text{Cs}^{134}$  is summarized.

## II. THEORY

In this section a brief presentation of the basic assumptions of the unified nuclear model is given to define the context for the discussion in Section V of the lifetime measurements in  $Tm^{169}$  and  $Tm^{171}$ . The angular momentum coupling scheme is described in order to define some of the important quantum numbers. The predictions of the model for the energies, static moments, and reduced gamma-ray transition probabilities within a rotational band in an odd-A nucleus are given in terms of parameters which depend on the intrinsic nuclear structure. Also, the extraction of the experimental value of the reduced gamma-ray transition probability from the various required data is exhibited. The material considered is restricted to that which is directly related to the present investigation.

Fundamental contributions to the development of the unified nuclear model which combines collective and intrinsic or individual particle motion were made by Bohr and Mottelson (1) and Nilsson (2). Considerable expansion of the original work has occurred (3).

The unified model considered by Nilsson is based upon the following assumptions:

- 1) the nucleus possesses an axially symmetric equilibrium deformation so that each individual nucleon moves in a deformed potential, and
- 2) the frequency of the intrinsic motion of the individual nucleon in the deformed well is large compared to that of the collective (rotational and/or vibrational) motion of the nucleus as a whole so that the wave function of the system can be separated into intrinsic and collective



parts (the adiabatic approximation). The wave function  $\psi$  is then expressed as the product

$$\psi = \chi_{\text{int}} \cdot \phi_{\text{vib}} \cdot \mathcal{D}_{\text{rot}} \quad (1)$$

In the cases of interest in this investigation one may assume the nucleus to be in the vibrational ground state and ignore  $\phi_{\text{vib}}$ .

For axial symmetry the intrinsic motion is characterized by the quantum number  $\Omega$  which is the projection of the intrinsic angular momentum on the nuclear symmetry axis, i.e., the sum of the individual contributions of all the particles,  $\sum \Omega_p$ .

The rotational motion is characterized by the quantum numbers  $I$ ,  $M$ , and  $K$ , which correspond to the total angular momentum, its projection on the space-fixed axis, and its projection on the nuclear symmetry axis, respectively. Here

$$\vec{I} = \vec{j} + \vec{R} \quad (2)$$

where  $\vec{I}$ ,  $\vec{j}$ , and  $\vec{R}$  are the total angular momentum, the intrinsic angular momentum, and the rotational angular momentum, respectively. In the case of highly-deformed axial symmetry  $\vec{R}$  is perpendicular to the symmetry axis so that  $K$  is equal to  $\Omega$ . A group of rotational states which all have the same intrinsic wave function are referred to as a rotational band.

The intrinsic Hamiltonian used by Nilsson to describe the single particle motion is

$$H = H_0 + C \vec{\ell} \cdot \vec{s} + D \ell^2 \quad (3)$$

where  $H_0$  is the ellipsoidal harmonic oscillator potential,  $C \vec{\ell} \cdot \vec{s}$  is the spin-orbit coupling term analogous to that used in the spherical shell model, and  $D \ell^2$  is a term added to depress the high angular

momentum states. The constants C and D are chosen to reproduce the isotropic shell model levels in the limit of zero deformation.

The details of the determination of the eigenvalues and eigenvectors for the intrinsic Hamiltonian are not important for the present investigation since attention is confined to transitions within a single  $K = 1/2$  rotational band. In this case the intrinsic states enter only into matrix elements which can be treated as parameters to be determined from experiment. The objective here is simply to see if a single set of overdetermined parameters can satisfactorily predict the present experimental data. The theoretical calculation of such intrinsic matrix elements is another aspect of model testing which is simply mentioned.

The excitation energies of a rotational band in an odd-A nucleus obtained from the rotational Hamiltonian and a general appropriately symmetrized wave function are

$$E_K(I) = E_K^0 + \frac{\hbar^2}{2\mathcal{I}} [I(I+1) + \delta_{K,1/2} a(-1)^{I+1/2}(I+1/2)] \quad (4)$$

where  $E_K^0$  is a constant depending only on the intrinsic structure,  $\mathcal{I}$  is the moment of inertia of the nucleus, and  $\hbar$  is Planck's constant. The decoupling factor  $a$ , which has its origin in "Coriolis" effects, gives rise to a partial decoupling of the intrinsic motion from the rotational motion and is defined by  $a = -\langle K = 1/2 | j_+ | K = -1/2 \rangle$ . (5)

The magnetic moment within an odd-A rotational band is given by

$$\mu = g_R I + (g_K - g_R) \frac{K^2}{I+1} [1 + \delta_{K,1/2} (2I+1)(-1)^{I+1/2} b_0]. \quad (6)$$

Here  $g_R$  is the collective gyromagnetic ratio which gives the contribution of the rotational angular momentum  $\vec{R}$  to the magnetic moment. In the review

of Nathan and Nilsson (3) the intrinsic parameter  $g_K$  is given by

$$g_K = \frac{1}{K} [Kg_\ell + (g_s - g_\ell)\langle K | s_3 | K \rangle] \quad (7)$$

and  $b_o$  is defined by

$$(g_K - g_R)b_o = -(g_\ell - g_R)a + (g_s - g_\ell)\langle K = 1/2 | s_+ | K = 1/2 \rangle \quad (8)$$

where the orbital and spin g-factors of a free nucleon are

$$g_\ell = \begin{cases} 1 \\ 0 \end{cases} \quad g_s = \begin{cases} +5.58; \text{ proton} \\ -3.82; \text{ neutron} \end{cases} \quad (9)$$

However, it is apparent that the odd particle cannot be considered as a free nucleon. Bochnacki and Ogaza (4) have pointed out that the nucleons in the saturated core are polarized by the spin-dependent interaction with the odd nucleon. Their theoretical investigations (5) of longitudinal and transverse spin polarization indicate that Equations 7 and 8 should be rewritten with longitudinal and transverse effective spin g-factors (for  $K = 1/2$ ) as:

$$g_K = g_\ell + 2(g_{s_\ell}^{\text{eff}} - g_\ell)\langle K = 1/2 | s_3 | K = 1/2 \rangle \quad (10)$$

$$(g_K - g_R)b_o = -(g_\ell - g_R^o)a + (g_{s_t}^{\text{eff}} - g_\ell)\langle K = 1/2 | s_+ | K = -1/2 \rangle \quad (11)$$

where  $g_R^o$  is the rotational g-factor of the even core. A simple relation exists between the matrix elements of  $s_+$  and  $s_3$ , which has the form

$$\langle K = 1/2 | s_+ | K = -1/2 \rangle = -\pi(1/2 + \langle K = 1/2 | s_3 | K = 1/2 \rangle) \quad (12)$$

where  $\pi$  is the parity of the odd-particle state. Equation 12 allows equations 10 and 11 to be combined in a manner which is independent of the detailed nuclear wave function for a self-consistency check.

The static quadrupole moment  $Q$  which enters into spectroscopically measurable interaction energies is related to the intrinsic quadrupole moment  $Q_0$  with respect to the nuclear axis in a manner that depends on the nuclear coupling scheme. For strong coupling

$$Q = \frac{3K^2 - I(I+1)}{(I+1)(2I+3)} Q_0 \quad (13)$$

In the unified model  $Q_0$  appears in the electric quadrupole transition probabilities and should be constant within a rotational band.

Moszkowski (6) has reviewed the general theory of multipole radiation which gives the transition probability for gamma radiation of multipole order  $\sigma L$  ( $\sigma L = ML$  or  $EL$  for magnetic or electric multipoles, respectively) as  $T(\sigma L; i \rightarrow f) = \frac{8\pi}{h} \frac{L+1}{L[(2L+1)!!]^2} \left(\frac{\omega}{c}\right)^{2L+1} B(\sigma L; i \rightarrow f)$  (14)

where  $h\omega$  is the gamma-ray energy,  $c$  is the velocity of light,  $(2L+1)!! = 1 \cdot 3 \cdot 5 \cdots (2L+1)$ , and  $B(\sigma L; i \rightarrow f) = |\langle \psi_f | m_{LM}^\sigma | \psi_i \rangle|^2$  is the reduced transition probability. The operator  $m_{LM}^\sigma$  is the appropriate electric or magnetic multipole operator describing the interaction between the nucleus and electromagnetic field. The final and initial state wave functions are represented by  $\psi_f$  and  $\psi_i$ , respectively.

The general formulas for the reduced transition probabilities have been derived by Nilsson (2) for the unified model. These formulas simplify considerably for transitions within a rotational band. For intraband E2 radiation in odd-A nuclei they have been given by Bohr and

Mottelson (1) for arbitrary  $K$  as follows:

$$B(E2; I+1 \rightarrow I) = \frac{15}{16\pi} e^2 Q_0^2 \frac{K^2 (I+1-K)(I+1+K)}{I(I+1)(2I+3)(I+2)} \quad (15)$$

$$B(E2; I+2 \rightarrow I) = \frac{15}{32\pi} e^2 Q_0^2 \frac{(I+1-K)(I+1+K)(I+2-K)(I+2+K)}{(I+1)(2I+3)(I+2)(2I+5)} . \quad (16)$$

The  $B(M1)$  for intraband transitions in odd- $A$  nuclei has been given by Bohr and Mottelson (1) for  $K \neq 1/2$  and by Nilsson (2) for  $K = 1/2$ .

Combining their equations (with  $K = \Omega$ ) gives

$$B(M1; I + 1 \rightarrow I) = \frac{3}{4\pi} \left( \frac{e\hbar}{2Mc} \right)^2 (g_K - g_R)^2 K^2 \frac{(I+1-K)(I+1+K)}{(I+1)(2I+3)} \\ \cdot \left| 1 + \delta_{K, 1/2} b_0 (-1)^{I-1/2} \right|^2 . \quad (17)$$

In the above equations  $e$  and  $M$  are, of course, the proton charge and mass, respectively.

Ordinarily a nuclear excited state has more than one decay mode available and the total decay probability  $\lambda$  is equal to the sum of all the partial decay probabilities  $\lambda_i$  for the various decay modes, i.e.

$$\lambda = \sum_i \lambda_i . \quad (18)$$

The relationship between the experimentally determinable total decay probability  $\lambda$ , the mean life  $\tau$ , and the half-life  $T_{1/2}$  is

$$\lambda = \frac{1}{\tau} = \frac{\ln 2}{T_{1/2}} . \quad (19)$$

Ignoring the possibility of beta decay, an excited nuclear state generally

decays via one or more gamma branches each of which may involve an admixture of more than one multipole type of radiation. In addition each of the transitions may in general, have internal conversion electron emission competing with gamma-ray emission.

The gamma-ray transition probability associated with the  $j^{\text{th}}$  transition can be expressed in terms of the half-life of the level if other quantities, which are normally obtained experimentally, are known, namely, the transition energy, the total internal conversion coefficient  $\alpha_j$  and mixing ratio  $\delta_j^2$  of the  $j^{\text{th}}$  transition, and the total transition intensities  $I_i$  for the various decay branches. Letting  $\lambda_i^{\text{tot}}$  represent the total decay probability associated with the  $i^{\text{th}}$  transition one has

$$\lambda = \sum_i \lambda_i^{\text{tot}} \quad (20)$$

and

$$I_i \equiv \frac{\lambda_i^{\text{tot}}}{\lambda} \quad (21)$$

Obviously

$$I_i \leq 1 \quad (22)$$

and

$$\sum I_i = 1 \quad (23)$$

The total decay probability associated with the  $j^{\text{th}}$  transition is the sum of the probability for gamma-ray emission  $\lambda_j^{\gamma}$  and the probability for internal conversion  $\lambda_j^e$ , i.e.,

$$\lambda_j^{\text{tot}} = \lambda_j^{\gamma} + \lambda_j^e \quad (24)$$

Hence

$$\lambda = \lambda_j^\gamma [1 + \alpha_j] \cdot \frac{1}{I_j} \quad (25)$$

since

$$\alpha_j \equiv \lambda_j^e / \lambda_j^\gamma. \quad (26)$$

Assuming, for example, that the  $j^{\text{th}}$  gamma transition is primarily M1 with an E2 admixture, as is frequently the case within a rotational band in an odd-A nucleus,

$$\lambda_j^\gamma = \lambda_j^\gamma(\text{M1}) + \lambda_j^\gamma(\text{E2}) \quad (27)$$

and one has

$$\lambda = \lambda_j^\gamma(\text{M1}) [1 + \delta_j^2(\text{E2/M1})] [1 + \alpha_j] \frac{1}{I_j} \quad (28)$$

where

$$\delta_j^2\left(\frac{\text{E2}}{\text{M1}}\right) \equiv \lambda_j^\gamma(\text{E2}) / \lambda_j^\gamma(\text{M1}). \quad (29)$$

The gamma decay probability  $\lambda_j^\gamma(\sigma_L)$  is identical to the gamma-ray transition probability  $T(\sigma_L; i \rightarrow f)$  given in Equation 14. Combining Equations 14, 19, and 28 gives the relationship for the experimentally determined reduced magnetic-dipole transition probability for comparison with Equation 17, namely,

$$B(\text{M1}; I+1 \rightarrow I) = \frac{9\hbar}{16\pi} (\hbar c)^3 \{ \tau E_\gamma^3 (1 + \delta_j^2)(1 + \alpha) \cdot \frac{1}{I_j} \}^{-1} \quad (30)$$

where the subscript  $j$  has been dropped except on  $I_j$ .

### III. EXPERIMENTAL TECHNIQUES

The measurement of nuclear lifetimes can be accomplished either directly via time measurements or indirectly via level width measurements. The latter approach makes use of the uncertainty relation,  $\Gamma\tau = \hbar$ , where  $\Gamma$  is the energy width of the level and  $\tau$  is the mean life of the level.

These two categories comprise a host of methods having varying degrees of applicability, accuracy, and technical sophistication. A brief summary of the general methods available for lifetime measurements and references to suitable review articles are contained in reference (7). Also useful in this regard is reference (8).

This work will consider only direct time measurements by the delayed-coincidence method which is generally applicable for lifetimes from  $10^{-5}$  sec to  $10^{-11}$  sec. The objective of the method is to measure the time delays between electronic pulses indicating the formation and decay of a particular nuclear excited state and to extract from these data the lifetime of the nuclear level. Normally these timing pulses are provided by detectors which are sensitive to the radiations indicating the birth or death of the nuclear level. However, in some cases, state formation is indicated by a trigger signal synchronized with a pulsed accelerator beam. Many other variations of the delayed-coincidence method are also possible depending on the method of production and lifetime of the radioactive parent isotope or resonant state, the type and energies of the radiations to be detected and the lifetime of the level to be measured.

The methods used in this investigation were especially suited to measurements involving a parent radioisotope with a half-life in the



neighborhood of two hours or longer produced by thermal neutron irradiation in a reactor, transitions (in nuclei with suitable atomic number  $Z$ ) whose energy and multipolarity are such that the internal conversion process is the principal decay mode, and level lifetimes  $\gtrsim 1$  nsec. After brief consideration of the constituents of a general delayed-coincidence apparatus, examples will be given for comparison purposes of a few configurations which have been applied to cases similar to that described above. Then a more detailed discussion of the apparatus and experimental procedure used in the present investigation will be presented. The references listed should not be considered as complete. They often present the latest unreviewed articles and one or two comprehensive reviews where possible. The intent is to provide an appropriate starting point for further literature retrieval by the interested individual.

#### A. Principal Constituents of Delayed-Coincidence Apparatus

The typical delayed-coincidence apparatus basically consists of a radioactive source and two radiation detector assemblies which provide timing pulses to the two channels of the time-difference-measurement electronics. Some form of energy discrimination is usually desirable in each channel in order to select only those radiations associated with the level under investigation.

The choice of suitable radiations is dependent on accurate knowledge of the decay scheme for unambiguous results although the delayed-coincidence method can be used as a tool in deducing the decay scheme.

The type of detection and energy discrimination used depends on the type and energy of the radiation involved as well as the lifetimes

to be measured. Ordinarily one is concerned with  $\gamma$  rays having energies from a tenth to a few MeV, internal conversion electrons below a few keV, or  $\beta$  rays up to a few MeV. Although solid-state detectors are being used more, as detectors and electronic techniques improve, the best time resolutions<sup>1</sup> are still obtained with scintillator-photomultiplier detection assemblies ( 7 ). The parallel-plate avalanche counter ( 9, 10) has been considerably improved as a detector for low-energy electrons (insensitive to  $\gamma$  rays) in delayed-coincidence measurements although its fundamental fault of no energy resolution capability remains.

The most popular photomultiplier tubes (PMT) have been the 56 AVP (11, 12, 13, 14, 15), the slightly faster XP1020 or XP1021 (11, 16, 17, 18, 19), and more recently the RCA8575 which has lower noise but also lower gain.

The choice of scintillator is dictated by the relative importance of light output (20, 21, 22, 23, 24), energy resolution (25, 26), and scintillation decay time (27, 28, 29, 30, 31, 32). Plastic scintillators have poor energy resolution and less light output compared to anthracene or NaI(Tl) but have much shorter decay times and are, therefore, preferable for timing measurements if the first two characteristics are tolerable.

For  $\gamma$  rays energy resolution is accomplished electronically by accepting only those pulses within a specified amplitude interval. With plastic scintillators there is essentially no energy discrimination possible except with the highest energy  $\gamma$  ray since energy loss in low Z material is predominantly due to Compton scattering. Better energy

---

<sup>1</sup>The time resolution,  $2\tau_0$ , is defined as the full width at half maximum (FWHM) of the delayed-coincidence distribution obtained with simultaneous radiations (prompt curve).

discrimination can be achieved with NaI(Tl) or Ge(Li) detectors with concomitant loss of time resolution ( 7 ).

Electronic energy discrimination can also be used with electrons directly incident on a scintillator or solid-state device; however, much better energy resolution ( $\lesssim 5\%$  in momentum) is possible by use of magnetic-spectrometer energy selection between the source and one or both detectors in delayed-coincidence measurements (33,34,35,36,37, 38). In some cases such energy resolution is necessary to eliminate unwanted coincidences associated with close-lying transitions originating from different nuclear states and is capable of providing the most unambiguous results when knowledge of the decay scheme is incomplete. Magnetic spectrometers do have the disadvantages of considerably reducing the geometrical efficiency (a few % of  $4\pi$ ) and increasing the time dispersion due to spectrometer path length differences. In some cases it is necessary to use light pipes (25, 34, 36, 37) between the scintillator and photomultiplier to avoid magnetic interference with photomultiplier operation and this can also increase the time dispersion. The decreased efficiency and time resolution is not troublesome for sufficiently strong sources and lifetimes  $\gtrsim 1$  nsec. It should also be noted that thin sources (39) are necessary to maintain good magnetic energy-discrimination at low electron energies.

The time measurement electronics is, in principle, very similar for most delayed-coincidence experiments except for the details of time calibration and auxiliary features (8) such as logical requirements, pileup rejection, pulse-height compensation, and time stabilization, if used. The essential elements are a time-to-amplitude converter (TAC),

which converts the detector-pulse time-differences to an electrical signal having an amplitude proportional to the time difference, and a multi-channel pulse-height analyzer (MCPHA) which measures the amplitude distribution of these analog time signals. A. Ogata et al. (40) have reviewed many such systems. Further references will be given later with the discussion of the electronic apparatus used in this investigation.

## B. Review of Delayed-Coincidence Systems Used With Very-Low-Energy Radiation

### 1. Back-to-back scintillation detectors

A survey was made of the tables of Lederer et al. (41) for half-life measurements involving a transition of energy  $\lesssim 40$  keV which gave a result  $\lesssim 20$  nsec.

The Brookhaven group (42, 43, 44) achieved significantly better time resolution ( $\lesssim 1.5$  nsec) than others in conversion-electron versus gamma-ray delayed-coincidence measurements. The conversion electrons were detected in thin (insensitive to  $\gamma$  rays) disks of Naton or Pilot B while the  $\gamma$  rays were detected by Naton cylinders ( $\gtrsim 2$  cm. thick). Both scintillators were mounted on photomultipliers and placed opposite the radioactive source. The best time resolution obtained was about 1 nsec for 35-keV electrons versus 370-keV  $\gamma$  rays. However, for 22-keV electrons versus 175-keV  $\gamma$  rays the  $2\tau_0$  was 3.8 nsec. The poor energy resolution available in either channel limits the applicability of this arrangement.

### 2. Avalanche counter opposite scintillation detector

The time resolution obtainable with the parallel-plate avalanche-counter has been significantly improved (9). Such a counter has the advantage that, in principle, its inherent time resolution should be

independent of the energy of the ionizing particle whereas the ordinary scintillation detector has an energy dependence varying roughly as the inverse square root of the energy loss in the scintillator (8) for a sufficiently large number of primary photoelectrons ( $\gtrsim 100$ ).

An avalanche counter for low-energy electron detection opposite a scintillator-photomultiplier assembly for detection of 200-keV beta rays has been used (45) to measure the 1.9-nsec half-life of the 31-keV level in  $\text{Al}^{28}$  with a  $2\tau_0$  of about 0.6 nsec. Earlier measurements using parallel-plate avalanche counters (46, 47) with time resolutions of from two to three nsec is in serious disagreement with the results of the present investigation.

Due to the lack of any energy discrimination capability in the avalanche counter and only poor resolution in the scintillation detector care must be exercised in the use of this apparatus. The presence of unresolved low-energy Auger electrons and conversion electrons associated with different levels can lead to a composite delayed-coincidence distribution which is due to more than one half-life.

### 3. Magnetic spectrometer opposite scintillation detector

Geiger et al. (38) have employed a  $\pi\sqrt{2}$  spectrometer, focusing the 203K conversion line, opposite a scintillator detecting the K x rays to measure the 1.0-nsec half-life of the 39-keV level in  $\text{Xe}^{129}$  with a  $2\tau$  of 2 nsec. It should be noted that the path length differences in a  $\pi\sqrt{2}$  spectrometer can contribute considerably to time resolution broadening especially at low energies. This is the reason for selecting the higher energy transition in the magnetic spectrometer. Path length differences are not nearly as serious with intermediate-image spectrometers such as

used in the present work.

#### 4. Back-to-back magnetic spectrometers

Various groups have used back-to-back lens spectrometers (33, 48) of the Gerholm type (36, 37) or intermediate-image type (34) for lifetime measurements. The latter type has a U-shaped axial field which is symmetric about the mid-plane of the spectrometer. This field produces an intermediate-image focus at the midplane of the spectrometer (see Fig. 1) and results in considerably less spherical aberration at the detector. Thus the transit-time spread might be expected to be less than for the Gerholm type. Specially shaped scintillators (49) may help reduce this time spread. One might expect the shorter path length of the Gerholm spectrometer to be advantageous with regard to transit time spread but this is not certain. Calculations (50, 51) of transit time differences for unaccelerated and accelerated electrons having the same final energy in a Gerholm spectrometer for electron energies less than 45 keV where such effects would be greatest lead one to believe that transit time dispersion is probably less than two-to three-hundred picoseconds in almost any lens spectrometer. In any case the best time resolutions obtained with the two spectrometer types operating with low energy electrons are to the author's knowledge comparable. The Studsvik group has recently measured (52) the half-life of the 39-keV level in  $\text{Hg}^{193}$  to be 0.6 nsec using 14 kV of preacceleration on the source. The effective electron energies striking the detectors for the 39L and 101L transitions were, therefore, roughly 39 keV and 101 keV, respectively, (the L binding energies are about 14 keV). The time resolution taken from their figure appears to be close to one nanosecond. The

best time resolution determined in the measurements described in this work at lower electron energies (31 versus 68 keV) was about 1.3 nsec. In subsequent work where the time resolution was more critical further adjustment of the low-energy-channel thresholds reduced prepulsing and tailing effects somewhat and gave a  $2\tau_0$  of 1.2 nsec for 28-keV electrons versus 113-keV electrons.

The back-to-back magnetic spectrometer system comprises the best combination of energy and time resolution capability for work with highly converted, low-energy transitions and lifetimes  $\geq 1$  nsec. When combined with electrostatic preacceleration such a system can be used with electron energies down to at least a few keV (see Section III.D.2).

### C. Apparatus

The system used in the delayed-coincidence measurements presented in this work utilized back-to-back intermediate-image beta-ray spectrometers to provide excellent energy resolution for selection of appropriate internal conversion electron lines associated with the feeding and depopulation of the level of interest. The advantages of this form of energy discrimination have been presented in Sec. III.B. Fig. 1 presents a schematic cross section of one of these spectrometers. The construction, modifications and operational characteristics of the spectrometers are given elsewhere (53, 54, 55).

Fig. 2 presents a schematic representation of the entire delayed-coincidence system. The radioactive source is placed on the axis of the two spectrometers. A specially designed source holder (see Section III.D.2) permitted application of electrostatic voltages to the source. A solid-

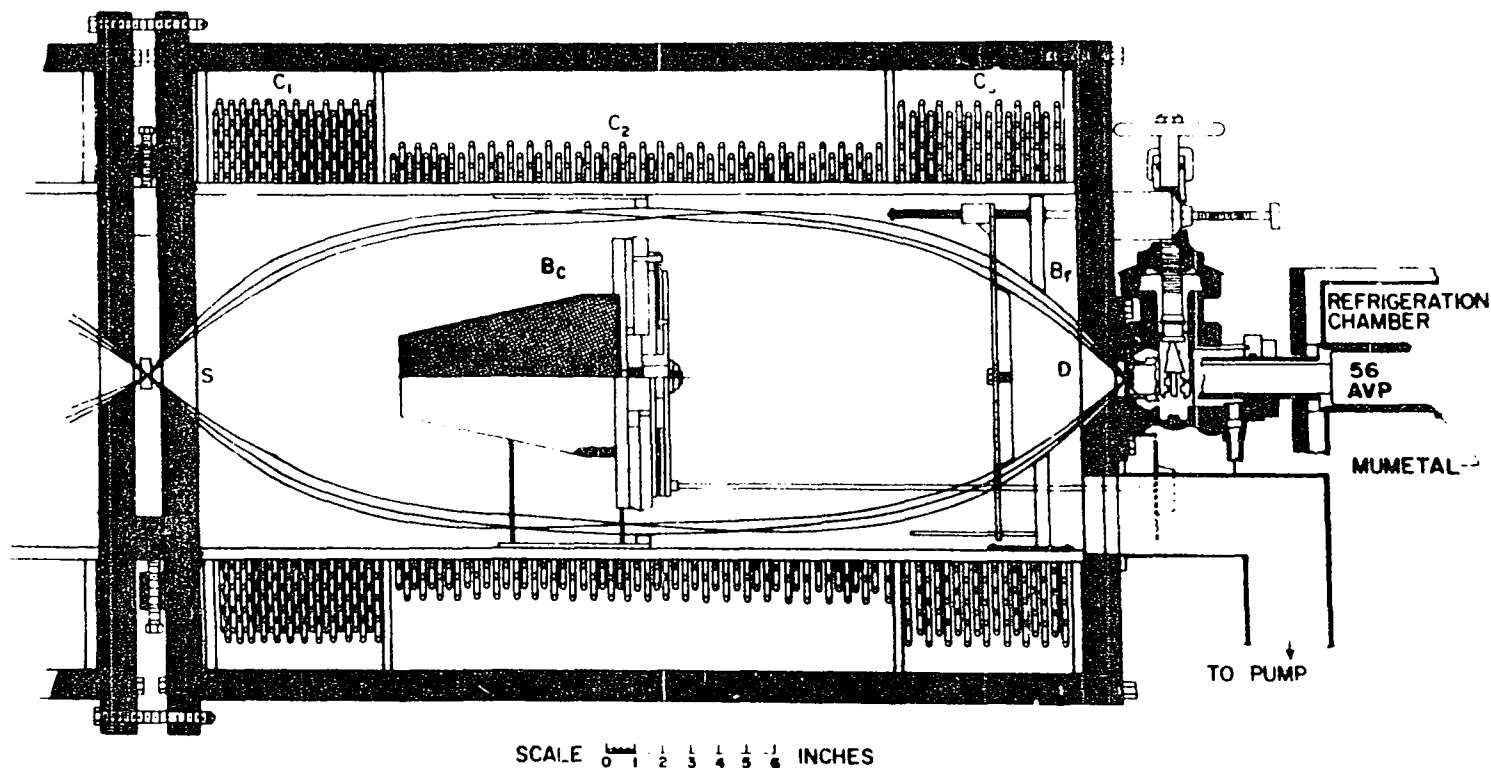


Fig. 1. Schematic cross section of the intermediate-image beta-ray spectrometers. (The electrons travel helical trajectories the distance of which from the axis is approximately indicated by the lines connecting S and D, the source and detector, respectively. The center and resolving baffles are  $B_c$  and  $B_r$ , respectively. The water cooled current coils are labeled  $C_1$ ,  $C_2$ , and  $C_3$ .)



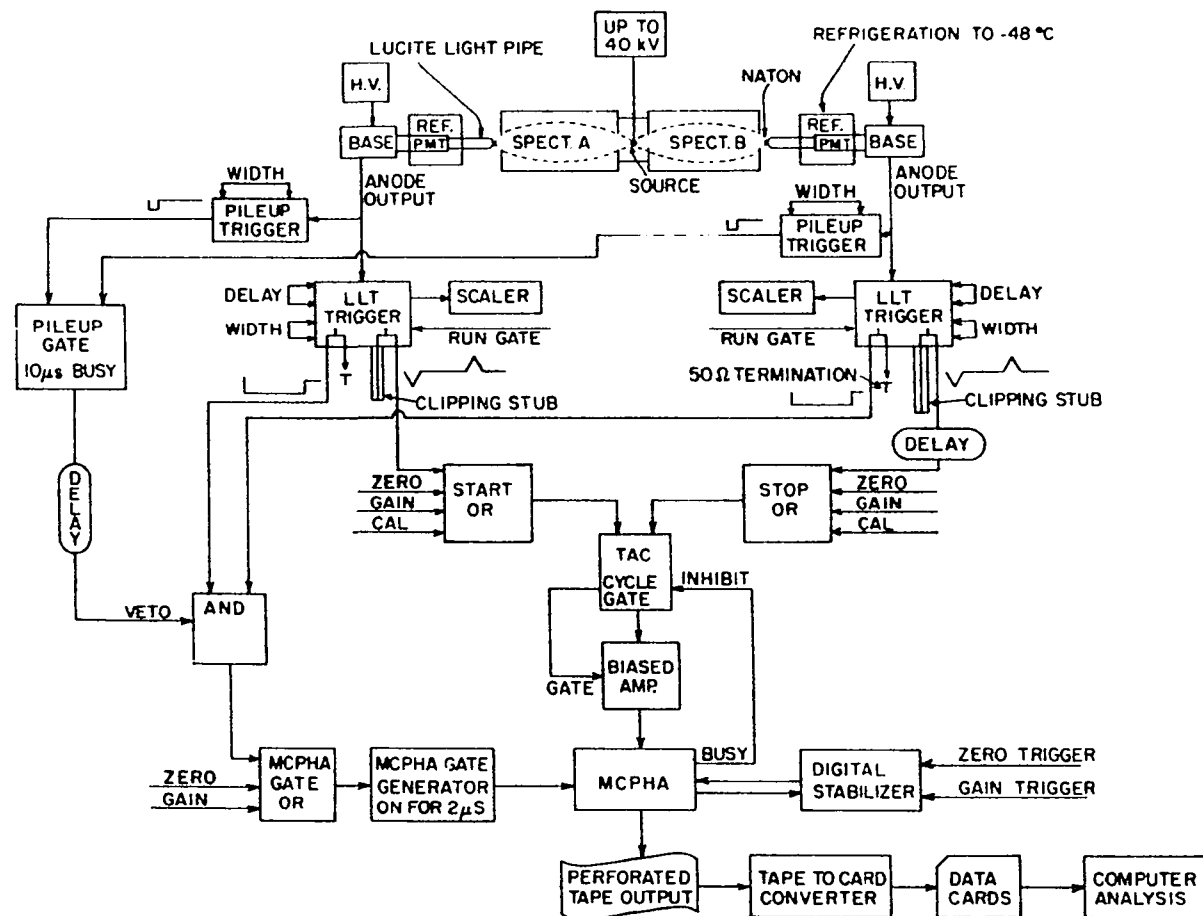


Fig. 2a. Delayed-coincidence system. (In (a) is represented schematically the source-detector configuration, energy discrimination method, and pileup-rejection, time-pickoff, and time-interval-measurement electronics. The interconnections with the stabilization electronics (b) and calibration electronics (c) are indicated. The data processing steps are also noted.)

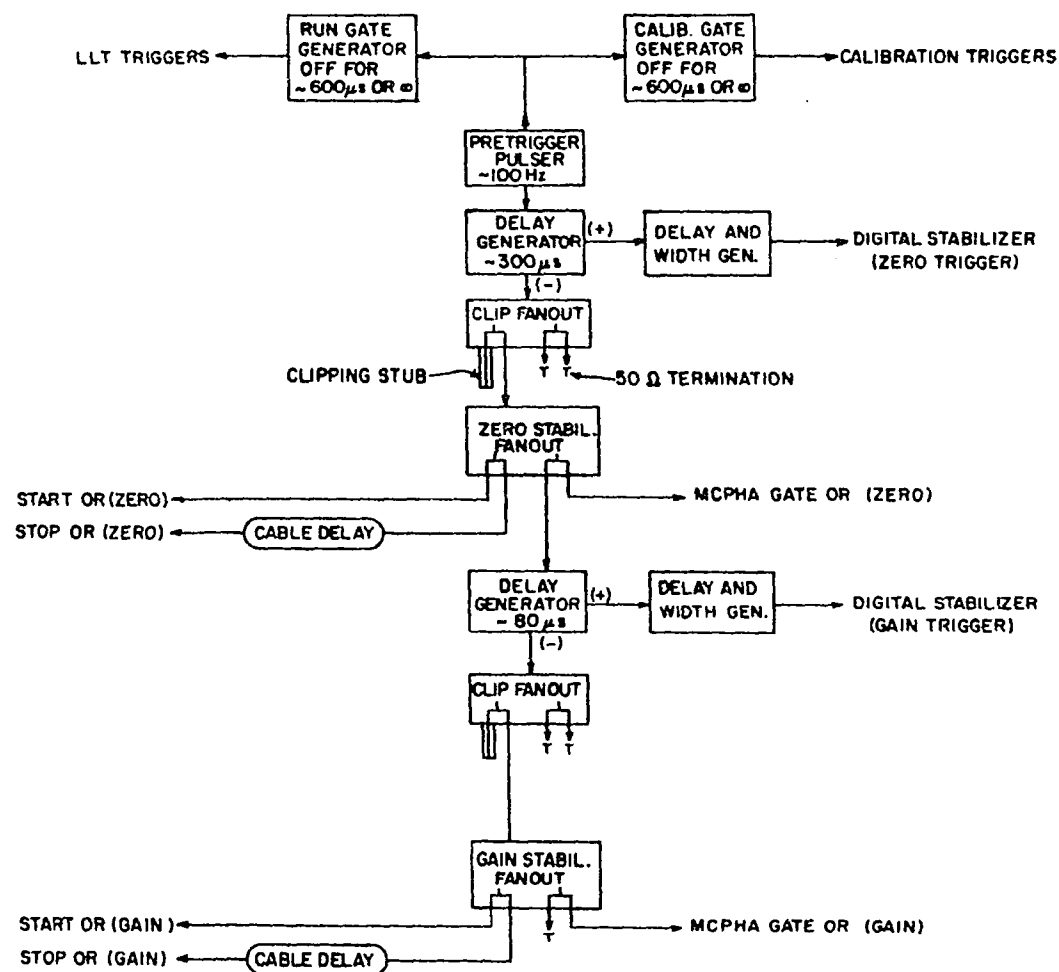


Fig. 2b. Delayed-coincidence system (continued). (In (b) is presented a block diagram of the stabilization electronics.)

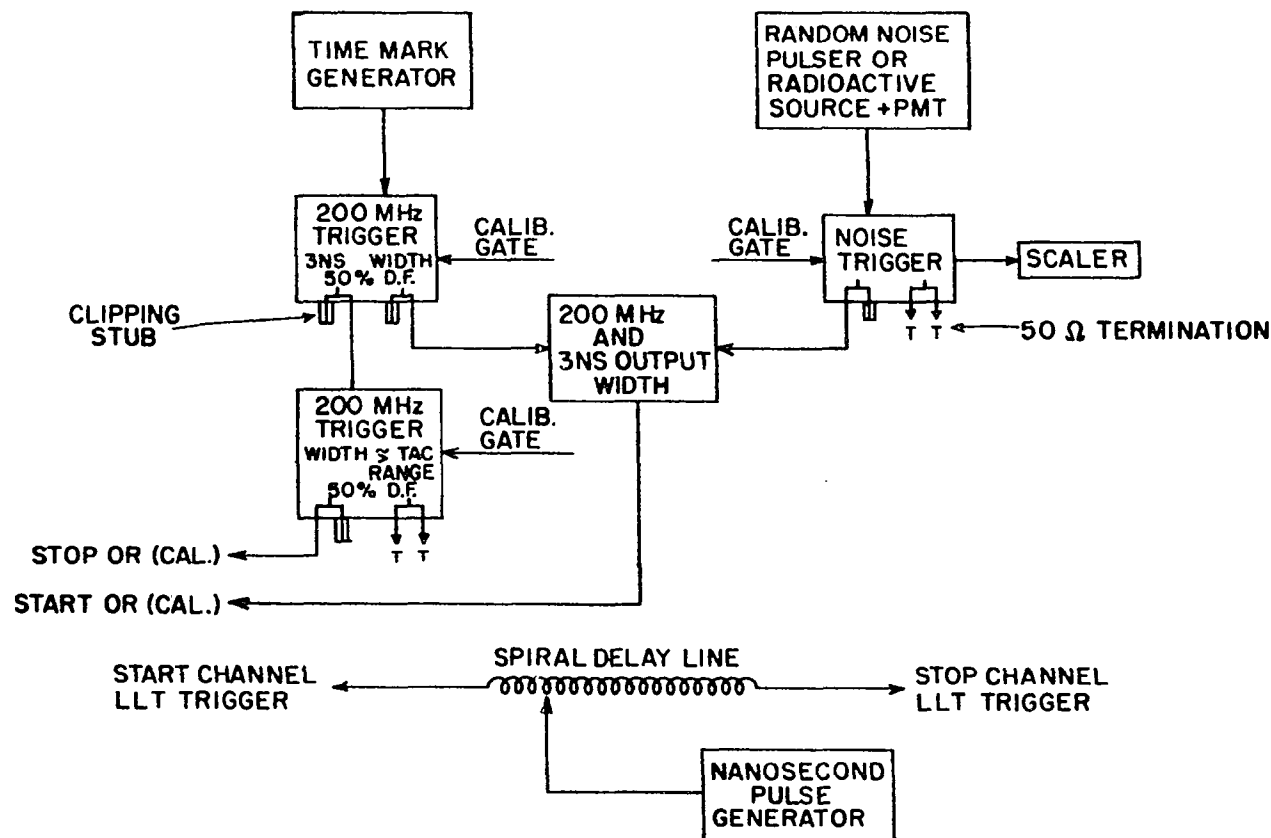


Fig. 2c. Delayed-coincidence system (continued). (In (c) two methods of time calibration are represented schematically. The electronic method (upper portion) was normally used but was compared with the spiral delay line method (lower portion).)

state 40-keV high-voltage supply<sup>1</sup> was used which had 0.01% line- and load-regulation specification and 0.1 % ripple specification, reversible polarity, rapid stabilization (< 10 min) and long term drift measured to be much less than 1 % in a day.

The focused electrons were detected in Naton 136 disks 0.025-in. thick by 0.5-in. diameter optically coupled to lucite light pipes which transmitted the light outside the spectrometer field to refrigerated phototubes surrounded by  $\mu$ -metal. The light pipes in spectrometer A (lower energy) and spectrometer B (higher energy) were, respectively, 12-in. long by 1.25-in. diameter and 8.5-in. long by 1.44-in. diameter. The lengths given include the approximate critical angle coupler sections used to improve light collection (56, 57 ). The effectiveness of the refrigeration in reducing phototube noise was discussed by McAdams and Hatch (34 ).

The phototube in the low-energy channel (spectrometer A) was a 56AVP which was used, in spite of known prepulsing problems ( 58 ), because of its high photocathode sensitivity ( $89 \mu\text{A}/\text{lm}$  at  $2854^\circ\text{K}$ ) and monochromatic sensitivity ( $56 \text{ mA}/\text{W}$  at  $4400 \pm 300 \text{ \AA}$ ) with  $10^8$  gain and  $0.5\text{-}\mu\text{A}$  dark current at 2480 V . A standard base assembly<sup>2</sup> was used and adjusted to give maximum pulse amplitude. The tube was able to be operated at 2750 V without bursting or excessive noise to provide maximum feasible amplification (see Section III.D.4).

The phototube in the higher energy channel (spectrometer B) was an

---

<sup>1</sup> Spellman High Voltage Electronics Corp., Model RHR-40-PN60.

<sup>2</sup> E G & G , Inc.

XP1021 with a photocathode sensitivity of  $82 \mu\text{A}/\text{lm}$  at  $2854^\circ\text{K}$  and monochromatic sensitivity of  $71 \text{ mA}/\text{W}$  at  $4370 \pm 50 \text{ \AA}$  with  $10^8$  gain and  $0.5\text{-}\mu\text{A}$  dark current at  $2700 \text{ V}$ . This tube and also another were both found to exhibit significant afterpulsing (59, 60) at about  $280 \text{ nsec}$  after the primary pulse; this property of the XP1021 has not been reported in the literature to the author's knowledge. A standard base assembly<sup>1</sup> was used and adjusted to give maximum pulse amplitude. The tube was operated at  $2680 \text{ V}$ . Separate power supplies<sup>2</sup> were used for the two photomultipliers.

In principle, the focusing potentiometers in a photomultiplier base assembly can be adjusted to optimize time resolution (61), however, such adjustments were expected to give negligible improvement since the major sources of time dispersion were probably the low electron energies and the light pipes.

The photomultiplier anode pulses were fed to the time measurement electronics. The principal features of the logic circuitry presented in Fig. 2 are the low-level-timing triggering, pileup rejection, time stabilization of the combined TAC, biased amplifier, and MCPHA, and electronic calibration capability with semiautomatic switching between the run and calibration modes of operation. Further discussion is confined to the case of a  $100\text{-nsec}$  TAC range as used in the measurements in  $T_m^{169}$  and  $T_m^{171}$ . Appropriate changes are necessary for other TAC ranges. For example, in the  $\text{Cs}^{134}$  measurement with the  $1.0\text{-}\mu\text{sec}$  range pileup rejection was not used due to the long ( $\approx 1 \mu\text{sec}$ ) LLT WIDTHs and veto-channel DELAY that would have been necessary. Changes in the sta-

---

<sup>1</sup>Amperex Electronic Corp.

<sup>2</sup>NJE Corp., Model HSV-5-20.

bilization delays and calibration adjustments are also necessary for different TAC ranges.

Neglecting temporarily the stabilization and calibration features, attention is confined to Fig. 2a. The anode pulses were split by passive 50 ohm impedance-matched signal splitters<sup>1</sup> to the pileup<sup>2</sup> and LLT<sup>3</sup> triggers. The LLT trigger acts as a modern high-efficiency counterpart to the old fast-slow coincidence apparatus ( 8 ). It provides two adjustable thresholds. The lower threshold establishes the timing of the output signal which is generated only if the upper threshold is exceeded. This feature reduces the time jitter associated with leading-edge timing with pulses of varying amplitude. The LLT DELAY used was 5 nsec which is appropriate for the Naton 136 rise time. The LLT WIDTHs used were 150 nsec. Short ( $\approx 3$  nsec) clipped pulses from the LLT triggers were fed to the START- and STOP-OR circuits<sup>4</sup> associated with the TAC<sup>5</sup> START and STOP channels.

The pileup triggers were operated with low threshold settings and provided 10-nsec width pulses to the pileup gate<sup>6</sup>. The pileup gate provided "updated", 10- $\mu$ sec signals delayed by 100 nsec to veto the overlap AND<sup>7</sup> which was fed by unclipped LLT signals. This setup has the effect of insuring that each channel is clear for at least 10  $\mu$ sec before a TAC output pulse is accepted for analysis since a TAC output must be

---

<sup>1</sup> Bishop Instrument, Inc.

<sup>2</sup> E G & G, Inc., Model TR104, modified for continuously variable threshold.

<sup>3</sup> E G & G, Inc., Model TD101, LLT (low-level timing) mode.

<sup>4</sup> E G & G, Inc., Model OR102.

<sup>5</sup> E G & G, Inc., Model TH200A.

<sup>6</sup> E G & G, Inc., Model GP100/N.

<sup>7</sup> E G & G, Inc., Model C104.

accompanied by an output from the overlap AND before the MCPHA is gated on. The rather slow conversion rate of the MCPHA<sup>1</sup> (2 MHz) made it desirable to inhibit the TAC while the MCPHA was busy and the gating of the biased amplifier<sup>2</sup> by the TAC "cycle-gate" signal was an added, but probably unnecessary, precaution. In addition the singles counting rates from the LLT triggers were also monitored by scalers.

The stabilization logic circuitry is given primarily in Fig. 2 b. The purpose of this circuitry is to generate for TAC analysis at regular intervals ( $\approx 100$  Hz) two pairs of stabilization pulses labeled ZERO and GAIN. The cable delay inserted in the channel feeding the STOP OR from the "zero-stabilization fanout" was selected to give a narrow peak at the low channel end of the time spectrum whereas a longer cable delay in the GAIN section provided a similar peak at the high channel end of the time spectrum. The digital stabilizer<sup>3</sup> associated with the MCPHA locked these peaks into specified channels. The creation of the stabilization pulse pairs from a single current source and use of fixed cable delays provided time-difference references having negligible time jitter. The system was capable of compensating for baseline or gain shifts in the TAC, biased amplifier, or MCPHA.

Appropriate gating and timing was provided by the various gate and delay generators<sup>4</sup> to insure that stabilization pulse-pairs did not interfere with run or calibration pulses. This was accomplished by gating off the LLT or calibration triggers during the stabilization cycle

<sup>1</sup>Radiation Instrument Development Laboratory, Inc., Model 34-12B.

<sup>2</sup>E G & G, Inc., Model AN109/N.

<sup>3</sup>Radiation Instrument Development Laboratory, Inc., Model 39-6.

<sup>4</sup>E G & G, Inc., Model GG200 or GP200/N.

( $\approx 600 \mu\text{sec}$ ) and waiting  $\approx 300 \mu\text{sec}$  for the analysis of possible previous coincidences to be completed before generation of the ZERO pulse-pair. A delay of  $\approx 80 \mu\text{sec}$  between the formation of the ZERO pair and the GAIN pair was needed to allow time for analysis of the ZERO pair. The stabilizer was provided with ZERO- and GAIN- trigger pulses from the delay and width generators<sup>1</sup> to indicate arrival of the respective ZERO- or GAIN- stabilization pulses. Pulses were also provided to the MCPHA GATE OR<sup>2</sup> to gate the MCPHA on for analysis of the TAC output pulses associated with ZERO or GAIN stabilization.

At least one possible improvement to the stabilization system should be indicated. It would be highly desirable, especially for measuring lifetimes  $\lesssim 2\tau_0$ , to include the photomultipliers and LLT Triggers in the stabilization loop. Such a system using a light pulser was developed by Griffin and Souder (62) for use with a  $\gamma$ - $\gamma$  coincidence apparatus. Technical difficulties arise in trying to apply this method to a back-to-back spectrometer system due to the wide separation of the detectors. However, for short lifetimes where counting-rate changes are likely to produce noticeable photomultiplier shifts (63,64) the effort might be worth while. A special technique has been described recently by Lindskog et al. (65) for maintaining constant singles rates by use of an auxiliary source and baffle system. However, this method does not protect against other causes of photomultiplier shift.

Fig. 2c presents schematic diagrams of two methods of TAC calibration used in this work. The upper part of the figure shows the

---

<sup>1</sup> Design by C. H. Weber, Ames Laboratory, Model ALRR 1013A-

<sup>2</sup> E G & G, Inc., Model OR102/N.



logic diagram of an electronic calibration scheme used throughout the present measurements. This configuration permitted semi automatic and simultaneous calibration of the entire TAC range with approximately 20,000 counts per peak in less than 15 minutes. This method was compared (see Section III.D.7) with the spiral delay method (66,34) shown in the lower portion of the figure.

In the electronic scheme a time-mark generator<sup>1</sup> with an accuracy of better than a few parts per million provides time markers or a sine wave to one section of a 200 MHz dual discriminator<sup>2</sup> set for minimum output width ( $\approx 3$  nsec). This trigger then produces synchronous pulse trains, having the preset frequency and clipped to minimum width, to a 200 MHz overlap type coincidence circuit<sup>3</sup> and also to the second section of the 200 MHz dual discriminator where the frequency of the pulses feeding the TAC STOP input is synchronously reduced by use of a width setting (continuously variable) somewhat larger than the TAC range being used. Coincidences between the pulse train and random pulses (average rate  $\approx 10$  kHz) provide TAC START pulses such that the START-STOP time interval is an integral multiple of the preset frequency. Starting the TAC with the AND output instead of the pulse train reduces the TAC deadtime. For general applicability to any TAC range it is important that the 200 MHz triggers fire only once per input above threshold regardless of input width and that neither 200 MHz trigger is operating in the "updating" mode. The continuously variable width is quite

---

<sup>1</sup> Tektronix, Inc., Model 184.

<sup>2</sup> Chronetics, Inc., Model 151.

<sup>3</sup> Chronetics, Inc., Model 157.

convenient and the capability to operate continuously at 200 MHz (after special factory "tuning") made it unnecessary to pulse the calibration gates.

The calibration was semiautomatic in the sense that the change from the run mode of operation to the calibration mode was easily accomplished in a few seconds by appropriate changes in the width setting of the run, calibration and MCPHA gate generators. During calibration the MCPHA was gated on continuously.

Several electronic TAC calibration schemes have been published (67, 68, 69, 70, 71, 72, 73, 74, 75, 76, 77). The present scheme is an extension of the method of Hatcher (75) to a minimum peak separation of 5 nsec. (200 MHz). The other schemes have minimum separations of  $\geq 10$  nsec except for de Waard's (76) where a 2-nsec separation was achieved. The 5 nsec separation obtainable with the present system was quite adequate for accurate calibration of the 100-nsec TAC range used in the two  $T_m$  measurements. It gave a factor of two improvement in the statistical accuracy of the calibration as compared to a 10 nsec separation. The minimum separation is limited to 5 nsec by the maximum operation frequency of the triggers, the minimum output widths obtainable ( $\approx 3$  nsec) and the minimum overlap requirements of the AND circuit ( $\approx 1.5$  nsec).

#### D. Experimental Procedure

Although the delayed-coincidence method is conceptually just a series of simple electronic "stopwatch" measurements, the region of the time and energy scales in which one must work when dealing with nuclear systems and the typical complexity of radiations emitted from a radio-

active isotope require the use of highly sophisticated techniques. Extreme care must be exercised to avoid the numerous possible sources of significant systematic error. A major part of the effort involved in the completion of this project involved the isolation and elimination of systematic errors which can adversely affect attempts to extend the delayed-coincidence method to accurate measurement of lifetimes of the order of a few nanoseconds with internal conversion electrons having only a few keV of energy indicating one of the transitions of interest. Internal conversion electrons or beta particles with energies of 50-100 keV were associated with the other time-defining transition. In view of the discrepancies found with other experimenters in all of the measurements it is fitting to analyze several aspects of the measurement process and indicate the care taken to avoid systematic errors. These aspects include source preparation, preacceleration technique, energy resolution, electron detection, time pickoff method, time resolution, time calibration, nonlinearity measurement and correction, and data analysis.

#### 1. Source preparation

The measurements described in this work utilized radioactive sources of  $\text{Yb}^{169}$ ,  $\text{Er}^{169}$ ,  $\text{Er}^{171}$ , and  $\text{Cs}^{134m}$  obtained by thermal neutron irradiation in the Ames Laboratory Research Reactor of enriched stable isotopes obtained from Oak Ridge (except for  $\text{Cs}^{133}$  which occurs with a 100% natural abundance). The use of enriched isotopes greatly reduces the chance of unwanted contaminating radiations. In all cases, no noticeable contaminating activities could be found in the electron spectra.

The sources were deposited either by vacuum evaporation or molecular plating (39) on 1/4-mil, aluminized-mylar film ( $0.8 \text{ mg/cm}^2$ ). The source

diameter used was 1/8 in. which permitted operation at 2% momentum resolution with the thin sources used. The longer-lived parent radioisotopes,  $\text{Yb}^{169}$  and  $\text{Er}^{169}$ , were deposited after irradiation. In this case aluminum support rings (5/8-in. o.d., 1/2-in. i.d., 1/16-in. thick) were used. For the shorter-lived activities,  $\text{Er}^{171}$  and  $\text{Cs}^{134\text{m}}$ , stable  $\text{Er}^{170}$  and  $\text{Cs}^{133}$  were deposited before irradiation in which case mylar support rings (5/8-in. o.d., 3/8-in. i.d., 0.01-in. thick) were used. A clear acrylic spray<sup>1</sup> was used to secure the film to the ring.

The mylar film became brittle after irradiation, especially for the 8 hour irradiations of  $\text{Er}^{170}$ , and had to be handled carefully. The mylar rings caused no special problem but tended to warp slightly. The short irradiations were carried out in machined polyethelene "pillboxes" designed to protect the source film from physical damage and contamination and allow quick, safe decapsulation.

Special test irradiations of a lone ring and blank mylar film mounted on mylar rings were made to check for contaminants which could lead to erroneous delay curves. The electron spectrum of the ring alone indicated only a slight increase of the count rate above background below 300 keV because the ring was outside the focal region of the spectrometer source position for the baffle settings used. The electron spectrum of the mylar film and ring together showed only a high-energy beta activity which was negligibly weak compared to the source strengths produced.

Delayed-coincidence runs with blank film under conditions identical to those used with the  $\text{Er}^{171}$  activity gave only a few prompt coincidences

---

<sup>1</sup> Bordon Chemical Co., No. 1301 (Krylon).

(less than 100 in 8 hours for an 8 hour irradiation). Such prompt coincidences have been observed for other beta sources, e.g.  $\text{Ag}^{110\text{m}}$ , when no true coincidences were expected. They probably arise from some sort of inelastic scattering involving radiation emitted during the decay process. In addition a six-hour delayed-coincidence run using an irradiated blank film, where the zero-energy peak<sup>1</sup> was selected in coincidence with betas located at the position of the 112K conversion line of the  $\text{Er}^{171}$  decay, gave only a negligible indication of tailing which might have been due to delayed events. Such a run should have detected any significant lifetime present in the film associated with the betas as was established by similar runs with  $\text{Yb}^{169}$  and also  $\text{Er}^{171}$ . It was concluded that only a negligible contribution could be expected from the irradiated film to delay curves obtained with the  $\text{Er}^{171}$  and  $\text{Cs}^{134\text{m}}$  sources.

Generally source activities of about 0.1 mCi are considered desirable for coincidence measurements with the intermediate-image spectrometers. However, when working with very-low-energy electrons attenuation in the source might limit the effective useful activity. Therefore, for  $\text{Er}^{170}$  and  $\text{Cs}^{133}$  a series of irradiations of sources of different thickness was made in order to determine a rough optimum thickness by comparison of the intensity of the low energy line to that of a higher energy line.

Information concerning the specific isotopes is given below.

---

<sup>1</sup>This peak, which appears to consist of field-emission electrons as well as very-low-energy Auger electrons and Koster-Kronig electrons, is located at the energy corresponding to the preacceleration voltage used.

a. The Yb<sup>169</sup> source ( $T_{1/2} = 32$  day ) Ytterbium material enriched to 19.5% in Yb<sup>168</sup>, which has a thermal neutron cross section,  $\sigma$ , of 11000 barns, was irradiated for 30 days in a flux of  $3 \times 10^{13}$  neutrons/cm<sup>2</sup> sec. After irradiation the Yb<sub>2</sub>O<sub>3</sub> was converted to YbCl<sub>3</sub> for vacuum deposition. The large cross section of Yb<sup>168</sup> results in a very high specific activity which allows preparation of very thin sources. The Yb<sup>169</sup> source was estimated to have an activity of the order of 0.1 mCi. The visual appearance of the source material was that of a slight haze on the aluminized mylar and the thickness was at least few orders of magnitude less than the other sources.

b. The Er<sup>169</sup> source ( $T_{1/2} = 9.4$  day ) Erbium material enriched to 95.2% in Er<sup>168</sup> ( $\sigma = 2b$ ) was irradiated for 9 days in a flux of  $3 \times 10^{13}$  neutrons/cm<sup>2</sup> sec. After irradiation the Er<sub>2</sub>O<sub>3</sub> was converted to ErCl<sub>3</sub> for electrodeposition by molecular plating. The probable form of the deposit was ErCl<sub>3</sub> · 6H<sub>2</sub>O. The source thickness was visually about the same as the Er<sup>171</sup> sources used. The activity was somewhat less than that of the Yb<sup>169</sup> source but probably of the same order of magnitude, namely, 0.1 mCi.

c. The Er<sup>171</sup> sources ( $T_{1/2} = 7.5h$ ) Erbium material enriched to 96.1% in Er<sup>170</sup> ( $\sigma = 9b$ ) in the form Er<sub>2</sub>O<sub>3</sub> was converted to ErCl<sub>3</sub> for electrodeposition prior to irradiation. With this method of source preparation nearly 100% efficiency can be achieved and source thickness can be quantitatively controlled. The probable form of the deposit was ErCl<sub>3</sub> · 6H<sub>2</sub>O. With this assumption, the thickness of the Er<sup>171</sup> sources used for the final measurements was less than 0.16 mg/cm<sup>2</sup>. Irradiations

of 8 hours duration were carried out in a flux of  $4.2 \times 10^{13}$  neutrons/cm<sup>2</sup> sec. The initial activities were again estimated to be of the order of 0.1 mCi.

d. The Cs<sup>134m</sup> sources ( $T_{1/2} = 2.9\text{h}$ ) Chemically pure Cs<sup>133</sup> (100% natural abundance) in the form CsF was deposited on the backing film by vacuum sublimation prior to irradiation. The poor efficiency of this method of deposition made quantitative thickness determination impossible. Two sources were used, one for runs 700A and 700B, the other for runs 701 and 702. The first source visually appeared to have about the same thickness as the Er<sup>171</sup> sources. Its initial activity was probably of the order of 0.1 mCi. The second source appeared to be several times thicker with a corresponding increase in activity. The thicker source was used intentionally to check for possible systematic errors originating from source thickness or high count rates. The irradiations, each of three hours duration, were carried out in a flux of  $4.2 \times 10^{13}$  neutrons/cm<sup>2</sup> sec.

## 2. Preacceleration technique

The use of a preacceleration voltage to increase the energy of the electrons striking the scintillation detector has several advantages. First, it permits more efficient electron detection (see Section III.D.4) which permits faster data accumulation. Second, it improves the signal-to-noise ratio of the detection assembly and allows a reduction in the noise-associated accidental coincidences. Third, it improves the time resolution of the apparatus (see Section III.D.6.) thereby reducing the chance of systematic error in data analysis (see Section III.D.9). And fourth, it makes it easier to obtain a prompt curve without changing the energies

of the electrons incident on the detectors which can be important for data analysis (see Section III.D.9).

Earlier work in this laboratory (34) with the 8-keV transition in  $\text{Tm}^{169}$  employed preacceleration by simple application of a negative electrostatic voltage to the source backing which was mounted in an insulated source holder. A problem arose in the attempt to extend this method to the lower energy 5-keV transition in  $\text{Tm}^{171}$ . With a preacceleration voltage of 25 keV it was found that the spectrometer transmission went essentially to zero for the 5M electrons and was very slight for the 5N electrons. This conclusion was reached after careful calibration of the spectrometer (see Section VIII.) and preacceleration voltage supply (see Section IX.) showed that with a 25-kV preacceleration all of the conversion lines in the  $\text{Yb}^{169}$  decay, down to and including the 8M line, fell precisely where they should if one assumes a 25-keV energy gain and the validity of the zero-preacceleration spectrometer calibration. However, the  $\text{Er}^{171}$  electron spectrum at 25 kV preacceleration gave no indication of the 5M- or 5N- conversion lines (see Fig. 4B, without source shield) at their expected locations.

The precise cause of this loss in transmission was not known. Previous work (78, 79) had indicated the importance of performing the preacceleration radially by use of concentric acceleration surfaces or grids with hemispherical symmetry. From a consideration of the geometrical configuration of the source environment (see Fig.1) it was apparent that the electric field between the source at a potential of -25 kV, say, and spectrometer at ground would not provide ideal radial



preacceleration. Most likely the trajectories of the electrons were drawn away from the spectrometer axis and toward the surface of the truncated-cone entrance opening in the iron end-plate of the spectrometer.

Experimental and numerical investigations ( 50,51 ) concerning preacceleration in a Gerholm type spectrometer had indicated that transmission was decreased because the electron trajectories were being drawn toward the spectrometer axis due of the presence of the lead direct beam interceptor which was only about 1.8 in. from the source. A "field corrector" was found to increase the transmission considerably. It consisted of a cone-shaped piece of metal supported on three wire legs about 0.5 cm above the source with the apex toward the source and at the same potential as the source. It seems that the most important feature of this corrector is that it reduces the influence of the direct beam interceptor on the field shape and electron trajectories near the source although it is claimed to have definite focusing properties as well.

In the case of the longer intermediate-image spectrometer the direct beam interceptor is about nine inches from the source and it was felt that the type of "corrector" described above would not be helpful. Intuitively it was felt that it would be beneficial to shield the source entirely from the preacceleration field so that the electrons could proceed along normal radial paths at least until they were beyond the dielectric region of the source holder. Furthermore, the use of a shield grid having an approximately hemispherical shape ought to change the field shape in such a way that the preacceleration would be more radial. An

additional advantage of shielding the source is the elimination of possible external electric field gradients at the vacuum-source-film interfaces; this removes a source of concern with regard to possible perturbed angular correlation effects.

With these considerations in mind a new source rod was built which would allow use of an approximately hemispherical source shield screen or other possible correctors if necessary. The source end of the rod is shown schematically in Fig. 3. The radius of the screen varies from 0.25 in. in the plane of the support ring to 0.19 in. directly above the source. This variation, which was necessary to accommodate the geometrical requirements of the source positioning slit, is probably not significant. The screen was 16 wire/in. mesh.

A comparison of the low energy portions of the electron spectra at a preacceleration voltage of -25 kV from the  $\text{Yb}^{169}$  and  $\text{Er}^{171}$  decays with and without the shield screen is shown in Fig. 4 a & b. The spectra in Fig. 4 b were taken with the same source and corrected for source decay. The low energy region of the electron spectrum from the  $\text{Cs}^{134m}$  decay is shown for comparison in Fig. 4 c (with shield screen only). All of the lines lie at their predicted positions. Obviously the lifetime measurements of the 5-keV level in  $\text{Tm}^{171}$  and the 11-keV level in  $\text{Cs}^{134}$  would have been only marginal without the shield screen.

Figure 5 compares the effect of the screen on higher energy conversion lines with the performance at the low energy region. The spectrum scans shown are the same as used in Fig. 4 b. The same source was used for both scans and the data was corrected for source decay.

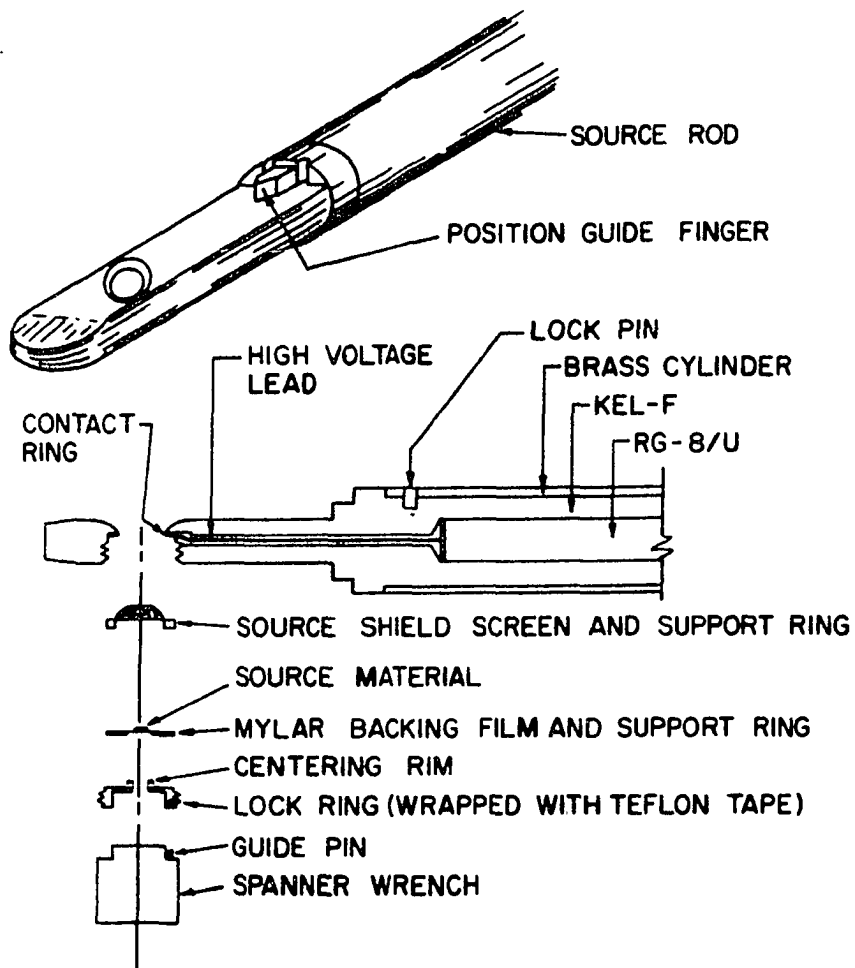


Fig. 3. Schematic diagram of the source end of the insulated source holder rod.

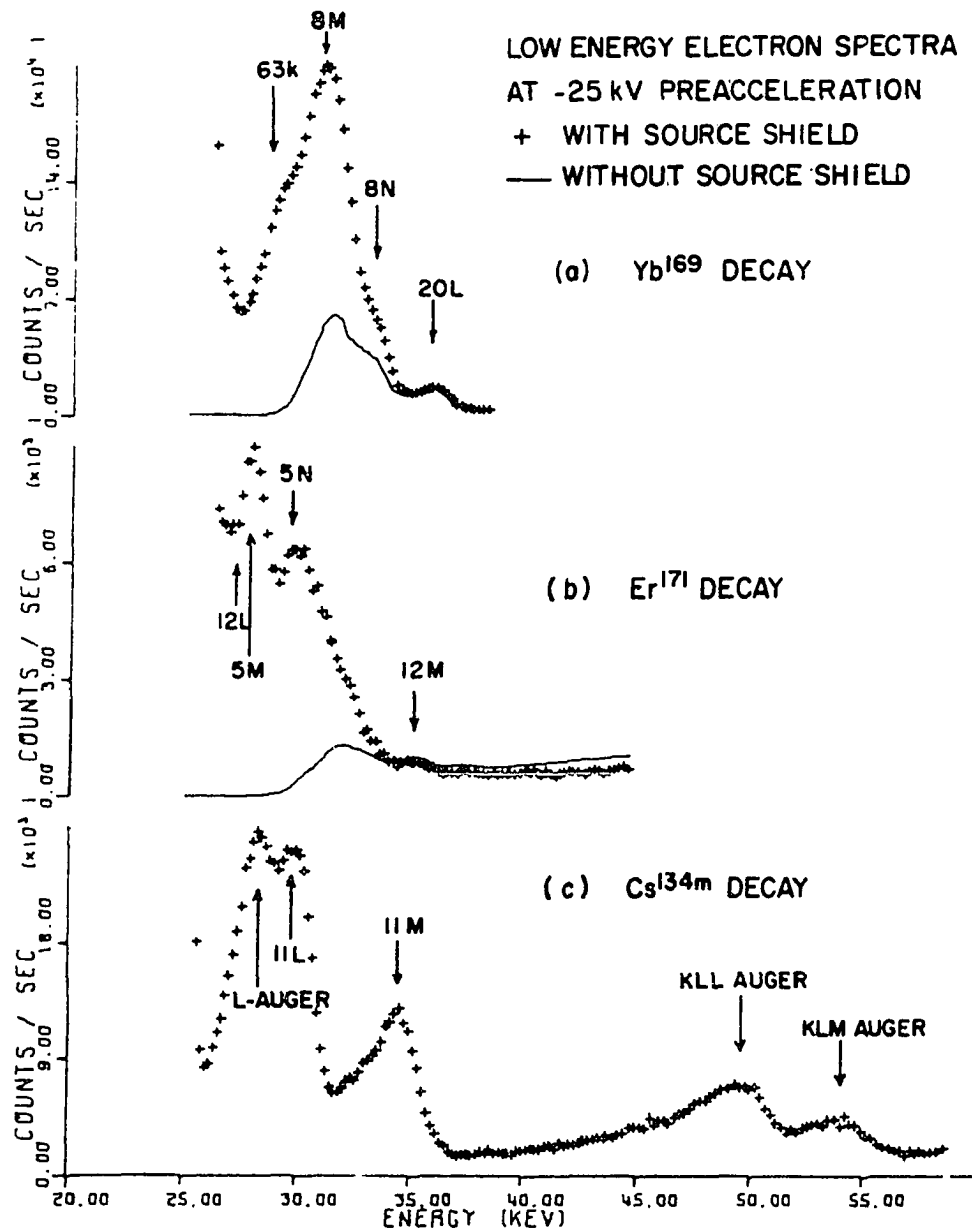


Fig. 4. Low energy portions of the electron spectra obtained from the  $\text{Yb}^{169}$  (a),  $\text{Er}^{171}$  (b), and  $\text{Cs}^{134m}$  (c) decays. (The source was at a potential of -25 kV in all cases. The plus signs indicate data taken while using the source shield screen whereas the solid lines represent data obtained without the screen. The data in (b) were corrected for source decay.)

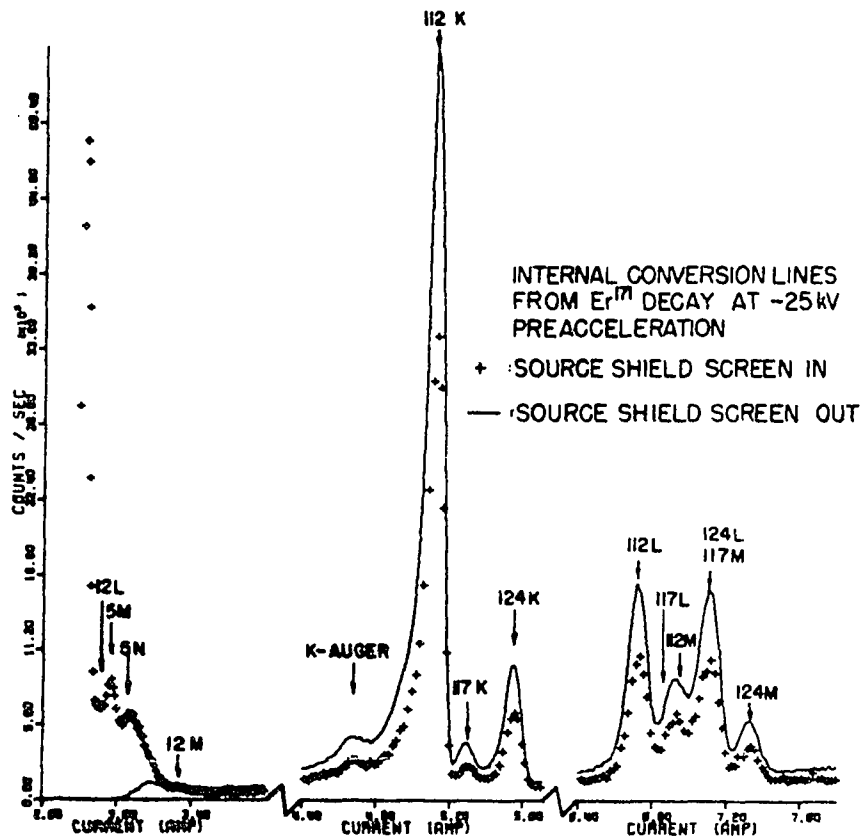


Fig. 5. Comparison of the influence of the source shield screen on spectrometer transmission at different energies. (The  $\text{Er}^{171}$  source was at a potential of -25 kV. The plus signs indicate data taken while using the source shield screen whereas the solid line represents data obtained without the screen. The data were corrected for source decay. The current-to-energy relationship is shown in Section VIII.)

Note that the line positions are unaffected. The reduction in transmission at higher energies is probably due to the interception of some electrons by the shield screen. At lower energies this effect is more than offset by improved field shape. In the coincidence measurements the higher energy transition is viewed through the backing and is not affected by the screen.

Different shield screens were used for different source isotopes to prevent accidental cross contamination of the data.

Other improvements in the preacceleration technique were also implemented. The final source rod design permitted indefinitely long operation at 25 kV (higher voltages were not required and, therefore, not tested). However, the use of Teflon tape (three wraps) around the lock ring was necessary to prevent corona or leakage currents. A safety circuit was installed to turn off the power to the high voltage supply in case of vacuum failure, excessive leakage current, or a discharge in the spectrometer. Use of a new solid-state high-voltage supply eliminated a three hour warmup period during which the output voltage of old supply drifted about 6%. The performance specifications of the new supply were given in Section III.C.

### 3. Energy resolution

The advantages of good energy resolution for delayed-coincidence measurements have been mentioned earlier in Section II.B. It was also indicated that the best energy resolution for electron-electron coincidence measurements is obtained by use of back-to-back magnetic spectrometers. Some disadvantages of such a configuration were also

indicated as being insignificant when dealing with lifetimes  $\gtrsim 1$  nsec and sufficiently strong sources as was the case for the present measurements.

For a magnetic spectrometer the momentum resolution,  $\frac{\Delta\eta}{\eta}$ , is independent of  $\eta$  where  $\eta$  is the relativistic momentum in units of  $m_0 c$  ( $m_0$  = electron rest mass,  $c$  = velocity of light) and is related linearly to the current,  $I$ , in the spectrometer coils (see Section VII). Therefore,

$$\eta = a I + b \quad (31)$$

and

$$\frac{\Delta\eta}{\eta} = \frac{\Delta I}{I} \quad (32)$$

The total relativistic energy  $\epsilon$  in units of  $m_0 c^2$  is related to  $\eta$  by the formula,

$$\epsilon^2 = \eta^2 + 1 \quad (33)$$

The kinetic energy,  $T$ , is given by

$$T = (\epsilon - 1) m_0 c^2 \quad (34)$$

From these equations one can show that the kinetic energy resolution is related to the momentum resolution by the formula,

$$\frac{\Delta T}{T} = \frac{\epsilon + 1}{\epsilon} \cdot \frac{\Delta\eta}{\eta} \quad (35)$$

The factor  $(\epsilon + 1)/\epsilon$  ranges from 1.95 to 1.80 for electron (kinetic) energies from 25 to 125 keV, respectively, which is the range of

---

<sup>1</sup>  $\Delta\eta$  is defined to be the FWHM of a well resolved spectral line resulting from monoenergetic electrons.

interest for the present measurements. A comparison of the shape of the electron spectrum obtained from the  $\text{Yb}^{169}$  decay plotted versus momentum with that plotted versus kinetic energy is given in Fig. 30 of Section VIII. The momentum resolution was 2%. This corresponds to a kinetic energy resolution of 3.9% to 3.6%, respectively, over the 25- to 125- keV range.

When preacceleration is used the effective resolution for a given internal conversion line is determined by the total momentum (or energy) including that gained because of the preacceleration. For this reason lines which are easily resolved without preacceleration can be unresolved with 25 kV applied to the source. This is seen to be true for the 8M- and 8N-conversion lines in the  $\text{Yb}^{169}$  decay by comparison of Fig. 30 of Section VIII. with Fig. 10 of Section IV.A.

In this work the baffles of the ~~low-energy-channel~~ spectrometer were set for an intrinsic momentum resolution of 2% which corresponds to roughly 2% transmission at zero preacceleration. This resolution in combination with a 25 kV preacceleration, which was sufficient for good electron detection (see Section III.D.4), gave adequate resolution of the 21L from the 8M, 8N, and Auger peak in the  $\text{Yb}^{169}$  decay (see Fig. 10 ) so that prompt curves could be obtained using the 21L line. In order to get a 2% resolution it was necessary to use a source diameter no larger than 1/8 in. and sufficiently thin sources as well as carefully center the source positioner. The source material was always on the side of the backing film facing the low energy channel.

The baffles of the higher energy channel spectrometer were set



for a momentum resolution of about 5%. Better resolution was not possible here due to the broadening of the lines which results from energy loss during penetration of the mylar backing film. The 5% resolution was, however, adequate to resolve the 110L and 177K lines in the  $\text{Yb}^{169}$  decay. From a study of the electron spectra and partial decay schemes given in Figs. 10, 18 and 26 one can see that only the 177K line could possibly introduce anything besides a prompt component into the delay curves obtained in this work.

#### 4. Electron detection

The physical makeup of the electron detection system has been given already in Sec. III.C. A discussion of the detailed mechanisms which occur during the detection and amplification process with the scintillator, light pipe, and photomultiplier is beyond the scope of this work. Such information can be found in references (21, 25, 80) . Here will be presented only a description of the measures taken to optimize and monitor detector performance over the data accumulation period ( $\approx 45$  days).

Due to the low light output from plastic scintillators, which are nevertheless quite desirable detectors for time measurements because of their fast decay times, considerable care must be exercised to achieve good light collection and amplification when working with low energy electrons. For this reason the phototube used in the low energy channel was specially selected for high photocathode sensitivity and low dark current and operated at a voltage somewhat higher than that specified for a gain of  $10^8$  (see Section III.C).

Special care was taken to achieve good optical coupling<sup>1</sup> of the scintillator, light pipe, and PMT and to keep the scintillator surface and light pipe walls free of light seal grease and vacuum grease. No reflective coating was used on the scintillator because of the low electron energies. Also no aluminum reflector was used on the light pipe walls since the slight improvement in pulse amplitude (25%) would be associated mostly with light which is reflected many times and, therefore, has a longer transit time. The increase in light transit-time-jitter could conceivably offset the benefits of greater pulse height.

The position of the scintillator along the spectrometer axis was adjusted to give the maximum counting rate.

In order to guard against deterioration of the detector performance due PMT or light seal degradation, pulse height distributions (PHD) at various electron energies, obtained with a long lived source ( $\text{Ba}^{133}$ ,  $T_{1/2} = 7.2\text{y}$ ), were monitored periodically during the delayed-coincidence measurements. (An LG102/N<sup>2</sup> was used to provide suitable stretching and amplification of the nanosecond PMT pulses before pulse height analysis.) These PHDs were compared to "standard" sets of PHDs taken at the same operating voltage (after a suitable noise stabilization period) before the lifetime measurements were begun. After the accumulation of the "standard" PHDs the light seals were checked for damage which can occur during placement of the detection assembly into its operating configuration. No damage was found. The monitored PHDs maintained the

---

<sup>1</sup>Dow Corning Optical Coupling Compound, Type 20-057.

<sup>2</sup>E G & G, Inc.

same shape and intensity as the "standard" PHDs throughout the measurements indicating no deterioration of detection performance. After the measurements were completed the light seals were again checked and found to be in perfect condition.

Fig. 6 shows a set of PHDs for the low energy channel which indicate the performance of the detection assembly. These PHDs have a better separation of the photopeak from the low amplitude rise than obtained with specially shaped Naton scintillators in a Gerholm spectrometer (49). The ability to separate the photopeak from the low amplitude rise is important for achieving optimum time resolution (see Section XI.) since the low amplitude rise is primarily associated with longer-lived excited states in the scintillator (21). The noise (dark-current) distribution gave only negligible contribution to the low amplitude rise.

The PHDs in Fig. 6 also compare favorably with those shown in (21) which were obtained without a light pipe using Pilot B.

##### 5. Time pickoff method

One of the most important elements of the electronics, especially for achieving the narrowest possible time resolution required in subnanosecond lifetime measurements, is the method of deriving the timing information from the detector pulses. The fundamental problem is how to get a time pickoff method which is independent of the detector pulse amplitude and rise time. Only approximate solutions have been found. The principal time pickoff methods used have been leading-edge timing, zero-crossing timing, and, more recently, constant fraction of pulse height

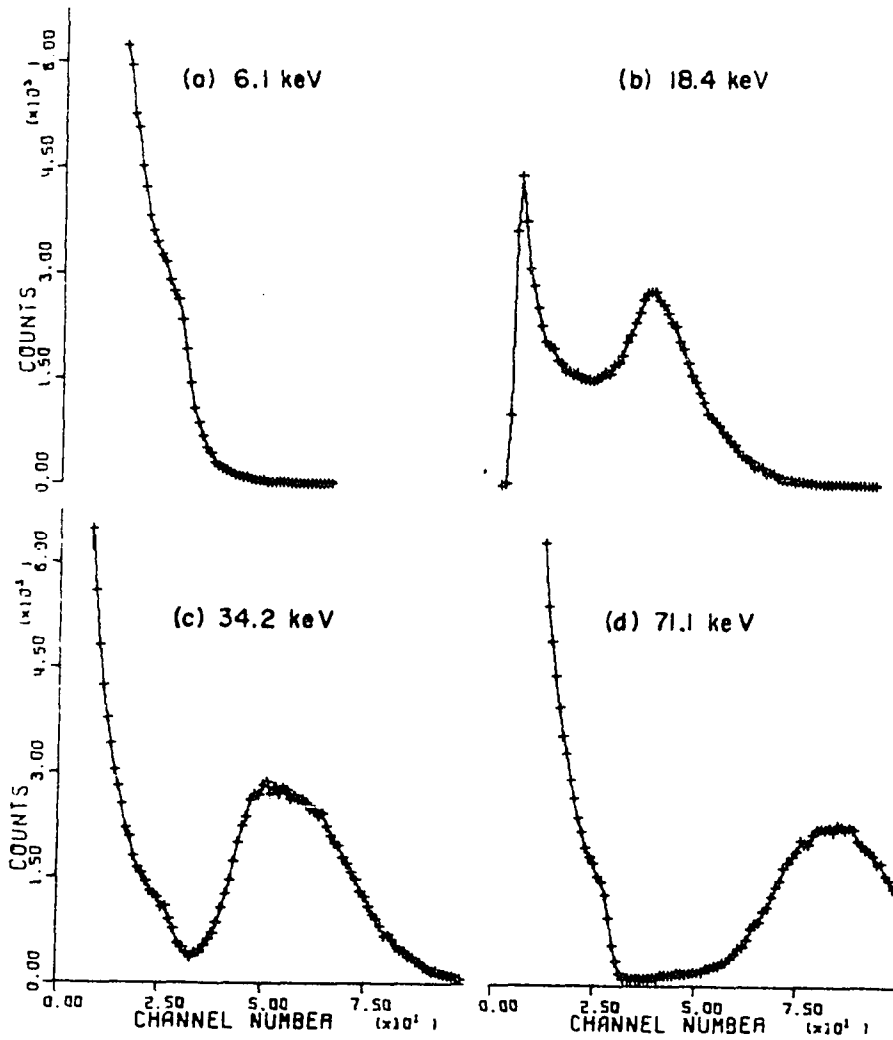


Fig. 6. Pulse height distributions obtained with electrons of different energy. (The detection system consisted of Naton 136 plastic scintillator, a lucite light pipe, and a 56AVP photomultiplier cooled to  $-48^{\circ}\text{C}$ . The incident energies were 6.1 keV (a), 18.4 keV (b), 34.2 keV (c), and 71.1 keV (d).)

timing. Some experimental aspects of the stalemate in the leading-edge timing versus zero-crossing timing controversy have been reviewed by Ogata et al. (40) whereas Bell (81) has given theoretical estimates which indicate that leading edge timing is always statistically superior to crossover timing. Schwarzschild and Warburton (7) have indicated that constant fraction of pulse height timing is comparable to leading-edge timing for plastic scintillators on fast PMTs where the pulse rise times are constant. However, constant fraction of pulse height timing gives better performance (82) with solid-state detectors where both rise times and amplitudes vary.

a. Low-level timing      The time pickoff method used in this work is a form of leading edge timing in which the timing is referenced to the crossing of a threshold, the E level, set as low as practicable on the leading edge of the detector pulses. However, an output pulse is not produced unless a second higher threshold, the  $E + \Delta E$  level, is crossed. This low-level timing reduces the time jitter associated with the varying amplitudes of the detector pulses.

Figs. 7 and 8 show pulse height distributions from the low- and high-energy channels, respectively, with different gating modes. The curves in Fig. 7 are for 27.5-keV electrons. Those in Fig. 8 are for 58.1 keV electrons. The figures display the relative positions of the various trigger threshold settings used in the delayed-coincidence measurements.

b. Systematic timing errors      A few systematic effects that can

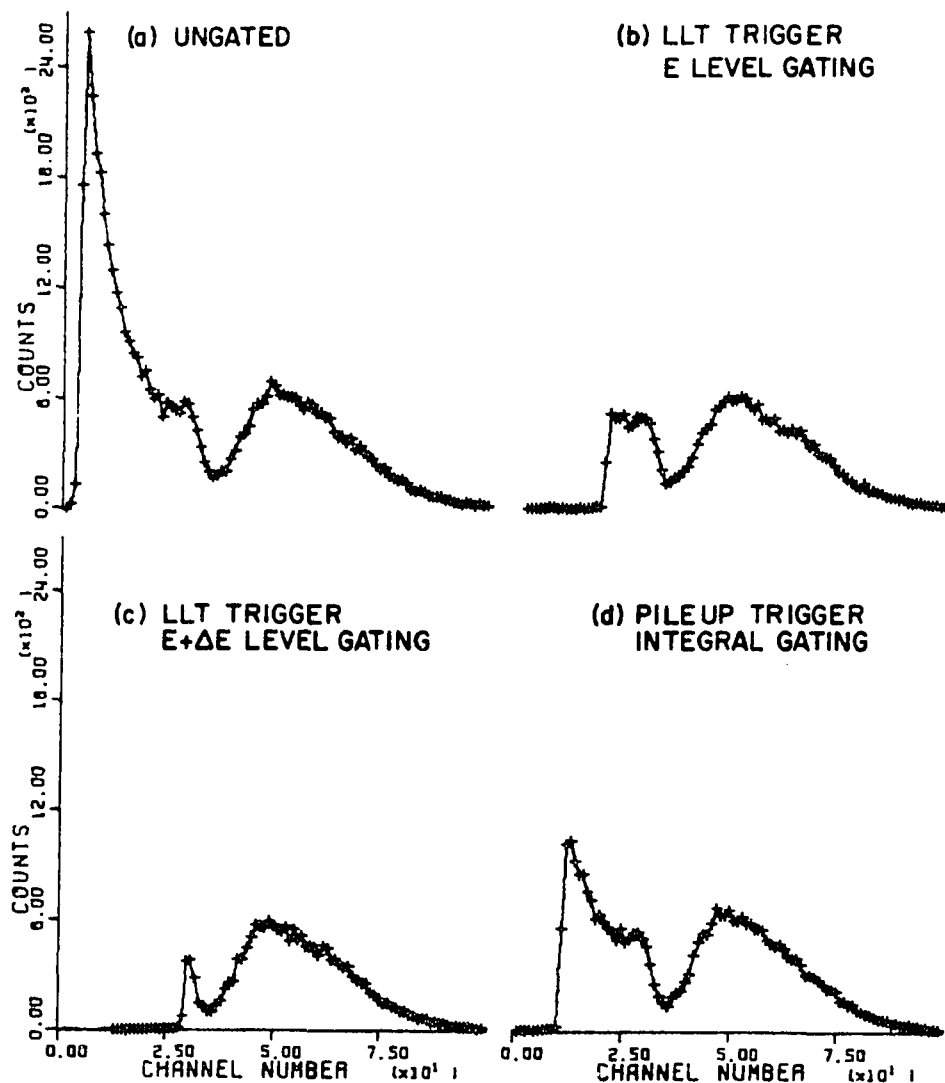


Fig. 7. Pulse height distributions in the low energy channel with different gating modes. (The incident electron energy was 27.5 keV. The ungated distribution is shown in (a). Distributions are also shown for gating from the lower threshold of the LLT trigger (b), the upper threshold of the LLT trigger (c), and the pileup trigger threshold (d).)

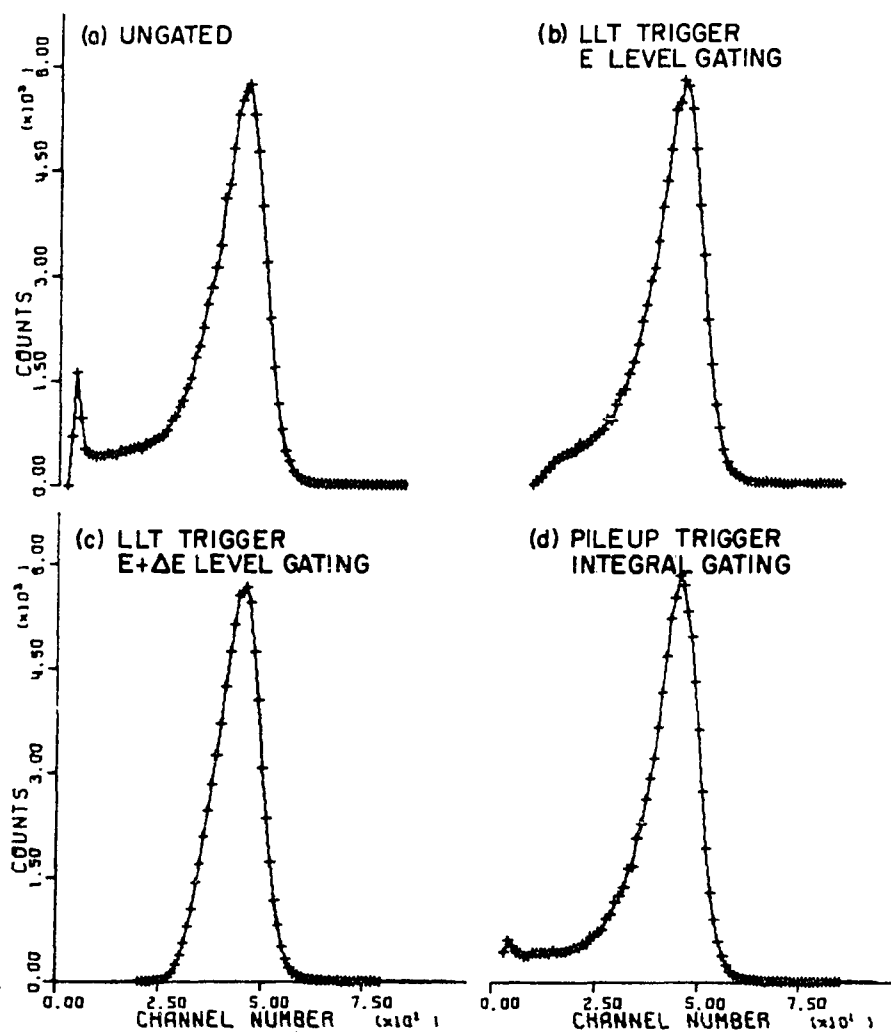


Fig. 8. Pulse height distributions in the high energy channel with different gating modes. (The incident electron energy was 58.1 keV. The ungated distribution is shown in (a). Distributions are also shown for gating from the lower threshold of the LLT trigger (b), the upper threshold of the LLT trigger (c), and the pileup trigger threshold (d).)

result in erroneous timing pulses are photomultiplier prepulsing and afterpulsing (see Section III.C), pulse reflections, and switch feed-through on commercial nanosecond cable-delay boxes.

The effects of prepulsing in the 56 AVP can be minimized by care in selection of the timing-level threshold. This is the reason for the relatively high E level in Fig. 7.

The pileup rejection circuitry (Fig. 2a) described in Section III.C. will eliminate all events where the timing pulse could be associated with an afterpulse for primary-to-afterpulse separations greater than the veto-channel DELAY (100 nsec) and less than  $10\mu\text{sec}$ . The deadtime of the LLT trigger ( $\geq 150$  nsec) ordinarily eliminates the possibility of generating erroneous timing pulses for primary-to-afterpulse separations less than the veto-channel DELAY. Two cases where this would not be true are

1. The primary pulse amplitude is below the timing threshold (E level) but the afterpulse amplitude is above the  $E + \Delta E$  level;
2. The LLT trigger undergoes a transition from the gated off mode to the gated on mode between the primary pulse and afterpulse. Both of these situations are very unlikely.

Most 50 ohm input impedances on nanologic circuits give rise to reflections of the order of 10%. Ordinarily this is not a problem except when pulses of wide dynamic range ( $> 10:1$ ) are fed to a trigger. In such a case multiple output pulses can be created if the trigger deadtime is less than twice the transit time of the cable from the detector to the trigger. If the trigger deadtime is greater than twice the transit time, erroneous timing pulses can still be generated if the trigger is gated



off for the primary pulse but on for the reflected pulse. To minimize such effects the LLT and pileup triggers were mounted on stands (forced air circulation provided) at the PMT bases and cables of the shortest possible length ( $\leq 4$  in.) were used to connect the PMT, splitter, and triggers (see Fig. 2a). Extender cables ( $\approx 10$ -ft. long) were used to power the triggers from the power manifolds. RG-174/U cable was used for the gate lines and additional filtering was added to the DC voltage levels in the triggers as a precaution.

Commercial delay boxes<sup>1,2</sup> have been found to exhibit switch feedthrough which produces attenuated pulses ahead of the delayed pulse. For logic signals this is no problem. However, such delay boxes should not ordinarily be used with detector pulses having a wide dynamic range.

## 6. Time resolution

An analysis of the various factors affecting the time resolution of the system is given here in order to be able to compare the observed resolution with theoretical predictions and examine possible improvements.

The width of the prompt curves observed in the present coincidence measurements is a result of electron transit-time dispersion in the spectrometers, the statistical properties of the scintillators and PMTs, and photon transit-time dispersion in the light pipes. From a statistical point of view one can associate mean values and standard deviations with the spectrometer transit time, the light-pipe transit time, and the scintillator PMT processes. It is convenient to isolate the light pipe

---

<sup>1</sup> E G & G, Inc.

<sup>2</sup> Science Accessories Corp.

conceptually from the scintillator and PMT, in spite of the fact that it joins them physically, since the theoretical calculations of detector statistics have not included light pipe effects.

The variance in the output timing of the pulses in a given channel will be the sum of the variances and covariances associated with the spectrometer transit time, light-pipe transit time, and scintillator-PMT processes. The spectrometer transit times can for practical purposes be considered independent of the other effects. There may be some correlation between the light-pipe transit time and PMT transit time since the latter depends on the point of origin of the photoelectron ( $\approx 0.2$  nsec maximum difference for an XP1020). No attempt has been made to evaluate this correlation, however, since its neglect probably affects the variance less than other approximations and uncertainties in the theory of scintillation detectors. In any case it is highly unlikely that the covariance of the light-pipe and PMT transit times is negative and decreases the net variance. Thus the sum of the individual variances should at least be a lower limit for the channel variance and an adequate estimate for the purposes of the present analysis.

The two coincidence channels are independent so the total variance will be the sum of the channel variances. If all the distributions associated with the processes introducing time dispersion were Gaussian then the time resolution function or prompt curve would have a Gaussian shape with a FWHM equal to 2.345 times its standard deviation which is just the square root of the total variance. The experimental prompt

curve shown in Fig. 9<sup>1</sup>, which was obtained with electron energies of 28 keV versus 113 keV, is somewhat asymmetric and not truly Gaussian. This is reflected in the fact that the standard deviation in the data is 0.59 nsec which would correspond to a Gaussian having  $2\tau_0 = 1.4$  nsec whereas the experimental  $2\tau_0$  is 1.2 nsec. It is not unusual for prompt curves obtained with radiations of significantly different energies to show asymmetry. Furthermore, experimental prompt curves generally have steeper slopes than a Gaussian. In the present situation there are also light pipe effects which are definitely not Gaussian in nature (see Section X. ). For these reasons the experimental factor,  $1.2/0.59 = 2.0$ , will be used to convert an estimated standard deviation to an expected  $2\tau_0$ .

In Sec. III B.4 it was noted that the maximum transit time dispersion in the spectrometers is probably less than a few hundred picoseconds. The standard deviation in the spectrometer transit time would be expected to be less by a factor of two to four, roughly, and might be expected to be associated with an approximately Gaussian distribution. (For estimation purposes a value of 0.1 nsec will be used.)

The early theories (80, 83) of the statistical properties of scintillator-photomultiplier detection assemblies assumed that a rather large number (at least 50) of primary photoelectrons,  $R$ , were produced at the

---

<sup>1</sup>This prompt curve was obtained with more careful threshold adjustments in work subsequent to the lifetime measurements treated here as was noted in Sec. III B.4. Its reduced prepulsing and tailing effects make it more appropriate for comparison with theoretical calculations. The best  $2\tau_0$  obtained in the present work was 1.3 nsec for 31-versus 68-keV electrons. Such prompts curves are shown in Section IV.

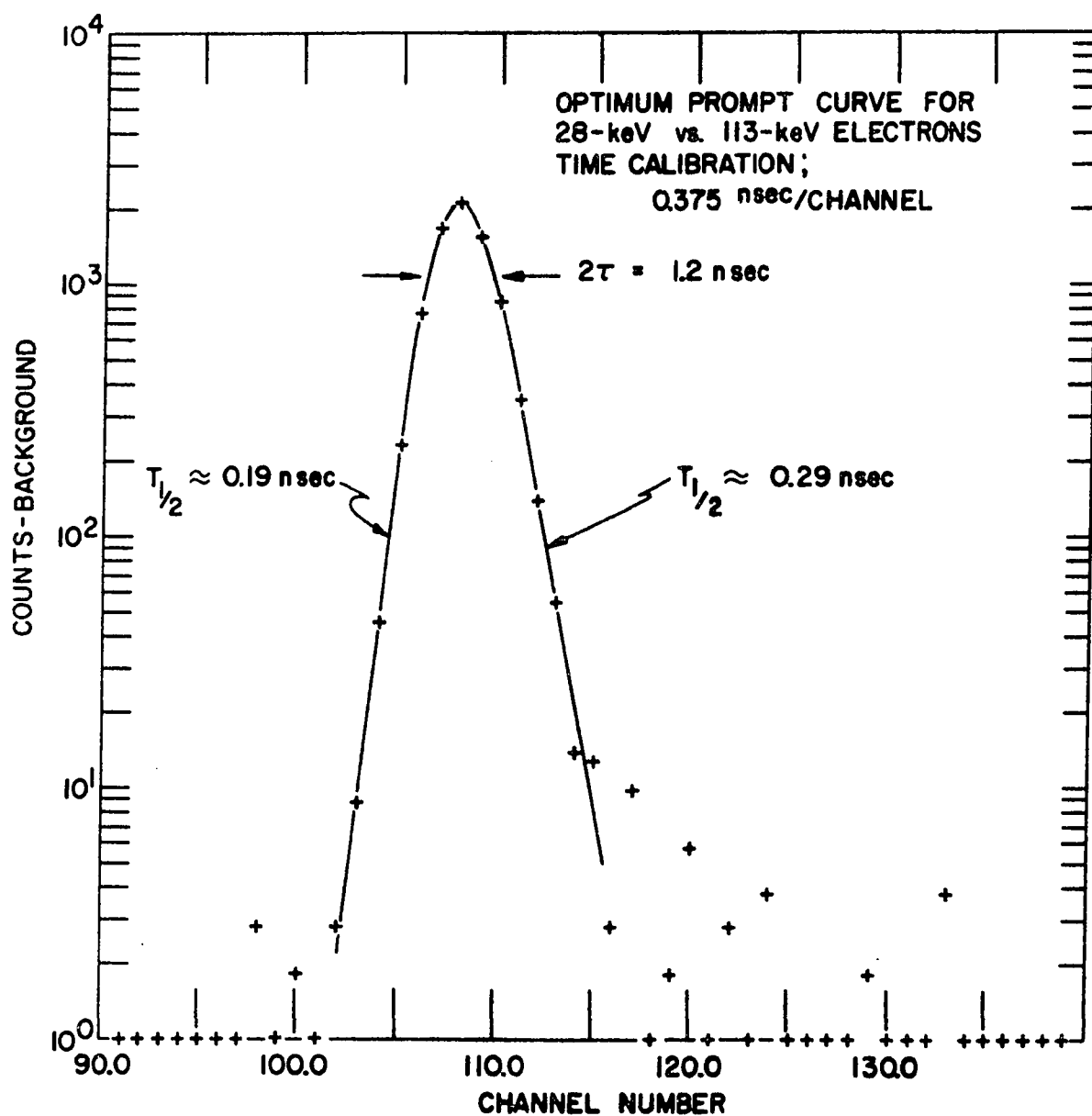


Fig. 9. Optimum low energy  $e^- - e^-$  prompt coincidence distribution.  
(The electron energies incident on the detectors were 28 keV and 113 keV.)

PMT photocathode. Since the data of Bertolini et al. (18) indicate that roughly one photoelectron is produced per 2.5-keV energy loss in Naton 136 on an XP1020 PMT, these early theories are applicable only for energies above 75 keV. Very recent calculations, however, have treated as few as five or ten photoelectrons so time resolution estimates for energies as low as 12 keV are now possible (84, 85).

With a photoelectron yield of one per 2.5 keV the electron energies associated with the prompt curve in Fig. 9 correspond to  $R \approx 11$  and  $R \approx 45$ . From the graph in the paper by Donati et al. (84) one can determine rough estimates of the optimum standard deviation in timing of a single Naton 136- XP1020 assembly for  $R = 5, 10, 20$ , and 50 to be 1.0-, 0.66-, 0.45, and 0.28- nsec, respectively.

In Section X. a simple but reasonable model is used to estimate the mean transit time and standard deviation for a light pipe. From the lengths given in Sec.III.C. and an assumed index of refraction of 1.5 for lucite one obtains standard deviations of 0.22- and 0.15-nsec, respectively, for the low- and high- energy channels. As was mentioned earlier these standard deviations do not correspond to Gaussian distributions.

Combining quadratically the standard deviations for the spectrometers, light pipes, and PMTs ( $R = 10$  and  $R = 50$ ) results in a predicted  $2\tau_0$  of 1.6 nsec. The fact that this value is larger than that observed may be due to the higher photoelectron yields which would be expected with the specially selected phototubes used (see Sec.III.C.). The monochromatic sensitivities of the photocathodes in the low- and high-energy channels, respectively, were 50% and 30% greater than the specified average value,

55 mA/w. (Light pipe losses would tend to reduce somewhat the effect of greater sensitivity on the photoelectron yield in comparison with the value of Bertolini et al.) Due to the fact that significantly higher photoelectron yields were probable in this work it seems reasonable to use the values  $R = 20$  and  $R = 50$  to calculate the estimated  $2\tau_0$ . The result then becomes  $2\tau_0 = 1.2$  nsec. The exact agreement with experiment is no doubt fortuitous. In any case the experimental apparatus performed as well as or better than reasonable estimates predict.

It is worth noting that elimination of the light pipes, if it could be done without introduction of adverse magnetic interference, would only reduce the estimated  $2\tau_0$  by about 0.1 nsec for the  $R$ -values used above. The light pipe contribution to the  $2\tau_0$  does not become an appreciable fraction of the total broadening until considerably larger  $R =$  values, i.e., higher energy radiations, better scintillator light output, or greater photocathode sensitivity, are obtained. Even with  $R = 50$  for both PMTs the estimated  $2\tau_0$  only drops from 1.0 nsec to 0.84 nsec.

The estimated contribution of the spectrometer transit-time dispersion to the time resolution broadening is negligible.

The excellent time resolution obtained in these measurements (considering the electron energies involved) is a result of careful attention paid to optimizing the many relevant factors discussed in previous subsections. Before this optimization program was undertaken the  $2\tau_0$  was about 3 nsec. The improvements effected made data analysis by the slope method (see Section III.D.9) easier and more reliable.

## 7. Time calibration

The time calibration of the delayed-coincidence apparatus is very crucial for the measurement of lifetimes with high accuracy. Several methods of time calibration have been treated briefly in references ( 8, 68 ). More recently there has been considerable emphasis on the development of electronic methods of calibration (67, 68, 69, 70, 71, 72, 73, 74, 75, 76, 77 ). The motivation for this effort is three-fold: accuracy, versatility and convenience. .

The time base oscillator used in an electronic calibration scheme is capable of calibration to an accuracy of a few parts per million (ppm) with drifts specified to be less than 3 ppm in 24h<sup>1</sup>. In addition the use of an electronic method rather than the commonly used calibrated delay cable technique eliminates possible systematic errors associated with the effects of dispersion and attenuation in the cables. Such deviations from the ideal transmission line can affect the rise time and amplitude of the calibration pulses and thereby introduce nonlinearity into the calibration ( 68, 71).

The use of an air-cored spiral delay line ( 66 ) can essentially eliminate the effects of dispersion and attenuation; however, it is feasible only over a range of about 100 nsec. The electronic method is extremely versatile and one setup can be used to obtain calibration peaks spaced from 5 nsec up to the long-time limit of applicability of the delayed-coincidence method ( $10^{-5}$  sec).

The electronic approach is also quite convenient in that all calibra-

---

<sup>1</sup> For example, Tektronix, Inc., Model 184, Time-Mark Generator.

tion peaks accumulate simultaneously and rapidly. In the version used in this work, which is described in Sec.III.C., it is also semiautomatic.

The time-mark-generator calibration was checked by the Ames Laboratory Instrumentation Group before and after the final series of measurements and found to be accurate to better than 5 parts per million.

a.  $T_m^{169}$  and  $T_m^{171}$  measurements For the 100-nsec TAC range used with the two  $T_m$  measurements the electronic calibration consisted of 18 peaks containing roughly 30,000 counts each and separated by 5 nsec. The calibration data was corrected for the nonlinearity of the combined TAC, biased amplifier, and MCPHA as described in Sec.III.D.8.) and (86,87) before analysis. A computer program was used to locate the peaks, compute their centroids, and fit a straight line to the centroid-versus-delay curve by an unweighted linear least-squares calculation. The calibration constant was determined from the slope of this line. The calculated statistical error was typically about 0.006%. An example of such a calibration is contained in ( 86 ). The only significant difference between this example and the calibrations used for the  $T_m$  measurements was a slight change in amplifier gain which gave a somewhat different calibration constant and linearity correction.

The  $T_m$  measurements were carried out over a period of 45 days. Calibrations were performed at least every other day. Over this period the calibration was constant within 0.25%. The weighted mean calibration constant from 52 calibrations was 0.38121 nsec/channel. The weights used were the inverse squares of the computed statistical errors in the individual calibrations. The weighted standard deviation of the values



from the weighted mean was 0.00011 nsec/channel. The calibration constant for the Tm measurements with conservative absolute 0.25% error limits was adopted to be  $(0.38121 \pm 0.00095)$  nsec/channel.

b. Cs<sup>134</sup> measurements For the 1.0  $\mu$ sec TAC range used with the Cs<sup>134</sup> measurements 16 peaks separated by 50 nsec and containing roughly 15,000 counts each provided the calibration constant after linearity correction and linear least-squares analysis similar to that described above. The measurements were carried out over a period of nine days. Over this period the calibration was constant to 0.1%. The weighted mean calibration constant from 5 calibrations was 3.6561 nsec/channel. The weighted standard deviation was 0.0013 nsec/channel. The calibration constant adopted for the Cs<sup>134</sup> measurements with absolute 0.1% error limits was  $(3.6561 \pm 0.0037)$  nsec/channel.

c. Comparison of electronic and spiral delay line methods In previous work in this laboratory (34, 35), which included a measurement of the lifetime of the 8-keV level in Tm<sup>169</sup>, a spiral-delay-line calibration method was used and compared to calibrated-delay-cable calibrations using either prompt radiations or a fast rise-time pulser. The various methods agreed within 1% error. However, the spiral delay line was not truly air-cored since the conductor wire was supported by a continuous layer of plexiglass and, therefore, could be expected to exhibit some dispersion and attenuation.

In the course of the present work a comparison of the electronic and spiral-delay-line calibration methods was made. The electronic method gave a calibration constant which was 1% lower than the spiral-

delay-line method. The error assignment for the calibration of the spiral delay line was 1% so the methods agreed within error. The electronic calibration is considered to be more accurate, however.

The fact that the electronic calibration was lower than the spiral delay calibration partially explains the 2% lower value obtained in the present work for the lifetime of the 8-keV level in  $\text{Tm}^{169}$  compared to the earlier measurement (see Sec. IV.A).

#### 8. Nonlinearity measurement and correction

It is well known that electronic instruments such as the TAC, biased amplifier, and MCPHA, which are essential elements in the time measurement process, depart somewhat from an ideal linear response. In the setup used in this work (see Fig. 2) this means that the time difference between two pulses fed to the TAC is not related to the channel number in the MCPHA in a perfectly linear manner. The integral nonlinearity of the present apparatus was found to be about 5% over 90% of the 100-nsec TAC range. If uncorrected, such nonlinearity can affect the final lifetime result in a complex manner because the non-constant channel width of the histogram data will lead to error in the calibration constant, inaccurate estimation of accidental coincidence background and inaccurate fits of the parameterized theoretical distribution to the data (see Sec. III.D.2). It was felt that such effects could possibly lead to a systematic error of a couple percent, especially for data such as shown in Sec. IV. where observation of the decay over many half-lives (obviously desirable for statistical accuracy) with a suitable background estimation region requires the use of a large fraction of the available delay range.

In order to avoid systematic error associated with instrumental nonlinearity a method was developed in the course of this work to eliminate MCPHA system nonlinearity by a correction technique using a computer. The method is based upon the rearrangement of the MCPHA histogram channel boundaries through the use of an accurate differential nonlinearity measurement, which gives the relative channel widths, in order to get channels of constant width. The linearity correction is applied to the time calibration data, the prompt curves, and delay curves in order to have all data correspond to the same channel width. A more detailed description of the numerical correction technique, experimental considerations of importance for obtaining a rapid, accurate differential nonlinearity measurement via the accidental coincidence distribution, and tests of the performance of the method are given in ( 86 ). The FORTRAN computer programs for correction and testing are presented in ( 87 ).

The accuracies of the differential nonlinearity data used in this work for correction of data taken on the 100-nsec and 1- $\mu$ sec TAC ranges were 0.3- and 0.2-%, respectively. Because of the inherent statistical accuracy of this data and the care taken to avoid possible systematic errors in the correction procedure (see reference ( 86 )) the error associated with system nonlinearity is believed to be negligibly small compared to the error assigned to the time calibration in the previous section.

The omission of linearity correction for typical sets of data resulted in half-life values  $\approx$  1% longer for the experimental conditions

used in this work. The linearity correction and more accurate time calibration are able account for the  $\approx 2\%$  lower half-life value obtained in this work for the 8-keV level in  $\text{Tm}^{169}$  compared to the earlier measurement (35).

## 9. Data analysis

The fundamental equation governing delayed-coincidence experiments expresses the fact that the time distribution of delayed coincidences  $D(t)$  is the convolution of the physical time-difference distribution  $f(t)$  with the time resolution function of the apparatus  $P(t)$ , i.e.,

$$D(t) = \int_{-\infty}^{\infty} f(t') P(t-t') dt' \quad (36)$$

where  $D(t)$ ,  $P(t)$ , and  $f(t)$  are all normalized to unit area and considered as probability densities. Depending on the experimental circumstances  $f(t)$  may correspond to a simple single-component exponential decay or a complex multi-component decay. All of the data encountered in this work can be represented by the simplest complex decay situation, namely, a single delayed component with a prompt admixture. This admixture is due to unresolved Auger electrons. In this case

$$f(t) = \begin{cases} 0 & \text{for } t < 0 \\ A \delta(t-0) + (1-A)\lambda e^{-\lambda t} & \text{for } t \geq 0. \end{cases} \quad (37)$$

In the analysis of experimental data it is necessary to take into account properly the histogram nature of the data, the influence of the accidental coincidence distribution, and systematic nonlinearity. The implications of these effects are treated in other work of the writer (86, 88 ).

The general problem of analysis of complex decay distributions has

been considered by the writer in some detail in other work (88 ). Different possible methods were discussed and compared. It was concluded that the unfolding of the delayed-coincidence distribution should provide the best statistical accuracy and least chance of systematic error. Accurate numerical methods were developed which are generally applicable to maximum-likelihood unfolding of complex delay curves using an experimentally determined prompt curve. A computer program was written which applies these methods to the case where  $f(t)$  is given by Equation 37 and the accidental coincidence distribution amounts to a superimposed constant background. The general features of the program are described in ( 88); the testing of the program with manufactured data is discussed in (89 ); and the program listing and usage are given in ( 90).

The fundamental assumption of the unfolding procedure developed is that the correct histogram time resolution function is known for the experimental conditions in effect during the delay curve measurement. Hence an auxiliary measurement of a prompt curve is required under conditions as closely reproducing the delay curve measurement as possible. In practice it is rather difficult to obtain an "exact" prompt source which has transitions of the same energy and counting rate as selected in the delay curve measurement associated with a mean life much less than  $2\tau_0$ . The ability to shift the electron energies by application of an electrostatic voltage to the source simplifies the problem somewhat and usually allows one to maintain constant energy conditions in at least the lower energy channel. One then relies on the fact that a small percentage change in the energies in higher energy channel

and different counting rates should not appreciably affect the prompt shape but only introduce time-zero shifts which can be treated as a determinable parameter in the analysis procedure. Deviations from this assumption will be reflected in the chi square of the fit.

From Equations 36 and 37 it is easily shown that

$$\frac{d}{dt} \ln D(t) = -\lambda \left(1 - \frac{P(t)}{D(t)}\right) + \frac{A}{D(t)} \cdot \frac{dP(t)}{dt} . \quad (38)$$

In the region of the delay curve where

$$\frac{P(t)}{D(t)} \ll 1 \quad (39)$$

$$\text{and } \left| \frac{A}{D(t)} \frac{dP(t)}{dt} \right| \ll \lambda \quad (40)$$

the half-life can be determined from the slope of a semilogarithmic plot of  $D(t)$ . The above conditions are true only when  $\tau \gtrsim 2\tau_0$  and when the prompt curve does not exhibit significant tailing or serious asymmetry.

For the final data obtained in this investigation Conditions 39 and 40 were fulfilled in all cases. Two forms of analysis based on Equation 38 were used and have been described in (88). One method consists of performing a linear least-squares fit to the logarithms of the delay data minus background in the tail region of the delay curve. The other method consists of a maximum likelihood fit of an exponential plus a constant background to the tail region of the delay data. The latter method allows the use of fit quantities which take into account more accurately the fundamental histogram nature of the delay data.

a.  $T_m^{169}$  and  $T_m^{171}$  data For this data all three of the above mentioned analysis methods were used. Since the half-lives were only a few times the  $2\tau_0$  of the system and since there was usually a significant prompt component in the data, care had to be used to pick analysis limits consistent with Conditions 39 and 40. This was simplified by the availability of the results from the unfolding analysis.

The prompt curves required for the unfolding analysis of the  $T_m$  data were obtained from the  $Yb^{169}$  decay using the 21L- versus 110K- or 110L- conversion lines with preacceleration or the 110K- versus 198K- conversion electrons with deacceleration. The intermediate level is the same for both cases and has a half-life of about 63 psec which is much less than the 1.3-nsec  $2\tau_0$ . The electron energy focused in the lower energy channel was kept constant for the prompt and delay curve measurements. For the  $T_m^{169}$  measurements the energy in the higher energy channel was changed by at most 4.5% between the prompt and delay curve measurements. For the  $T_m^{171}$  measurements the energy change was less than 11% or 7% for delay runs using the 112K- or 112L- conversion line, respectively.

The fact that the chi square is generally lower for the  $T_m^{171}$  data (cf. Tables 2 and 8) which had larger energy changes seems to indicate that factors other than the energy change between the prompt and delay curve measurements were more critical in determining the goodness of the fit. It is possible that time-zero drifts during data accumulation were the primary cause of fit degradation. Such drifts originating in the photomultipliers or low-level-timing triggers would not have been corrected by the stabilization electronics.

b. Cs<sup>134</sup> data For the Cs<sup>134</sup> measurements the 46-nsec half-life was considerably larger than the 1.3-nsec  $2\tau_0$  of the system and the prompt admixture was rather small. Thus the conditions necessary for the validity of slope analysis were easily fulfilled. Since the  $2\tau_0$  of the system was less than the calibration constant ( $\approx 3.7$  nsec/channel) the prompt curve was nearly a  $\delta$ -function and unfolding analysis by the technique described above was not possible. Therefore, only the two tail fitting methods of analysis were used in the determination of the lifetime of the 11-keV level in Cs<sup>134</sup>.



#### IV. EXPERIMENTAL HALF-LIFE RESULTS

In this section the experimental results of the lifetime measurements of the very-low-energy first-excited states in  $\text{Tm}^{169}$ ,  $\text{Tm}^{171}$ , and  $\text{Cs}^{134}$  will be presented. The results obtained from the different data analysis methods will be compared. The assignment of error will be discussed. The final adopted values will be compared to the results reported by other experimenters and one indication of systematic discrepancy will be pointed out.

##### A. The 8.4-keV Level in $\text{Tm}^{169}$

The half-life of the 8.4-keV level in  $\text{Tm}^{169}$  was investigated by means of both the beta decay of  $\text{Er}^{169}$  and the electron capture decay of  $\text{Yb}^{169}$ . The decay scheme features (41) of importance to the present investigation are presented in Fig.10 along with an electron spectrum obtained with a  $\text{Yb}^{169}$  source at a preacceleration voltage of -25 kV. The labeled arrows in this figure as in all other electron spectra shown in this work indicate the expected location of the electron line. Another electron spectrum exhibiting the  $\text{Yb}^{169}$  decay with no preacceleration voltage is given in Fig.30 of Section VIII. Neither of these spectra was taken using the source shield screen. A scan of the low energy region at -25 kV with the shield screen is shown in Fig. 4. All three of these spectra were taken with the low-energy-channel spectrometer at the same baffle settings as used in all the lifetime measurements. The discriminator threshold settings and detector operation conditions were not the same so one should be careful to avoid drawing invalid conclusions concerning relative intensities and counting efficiencies.

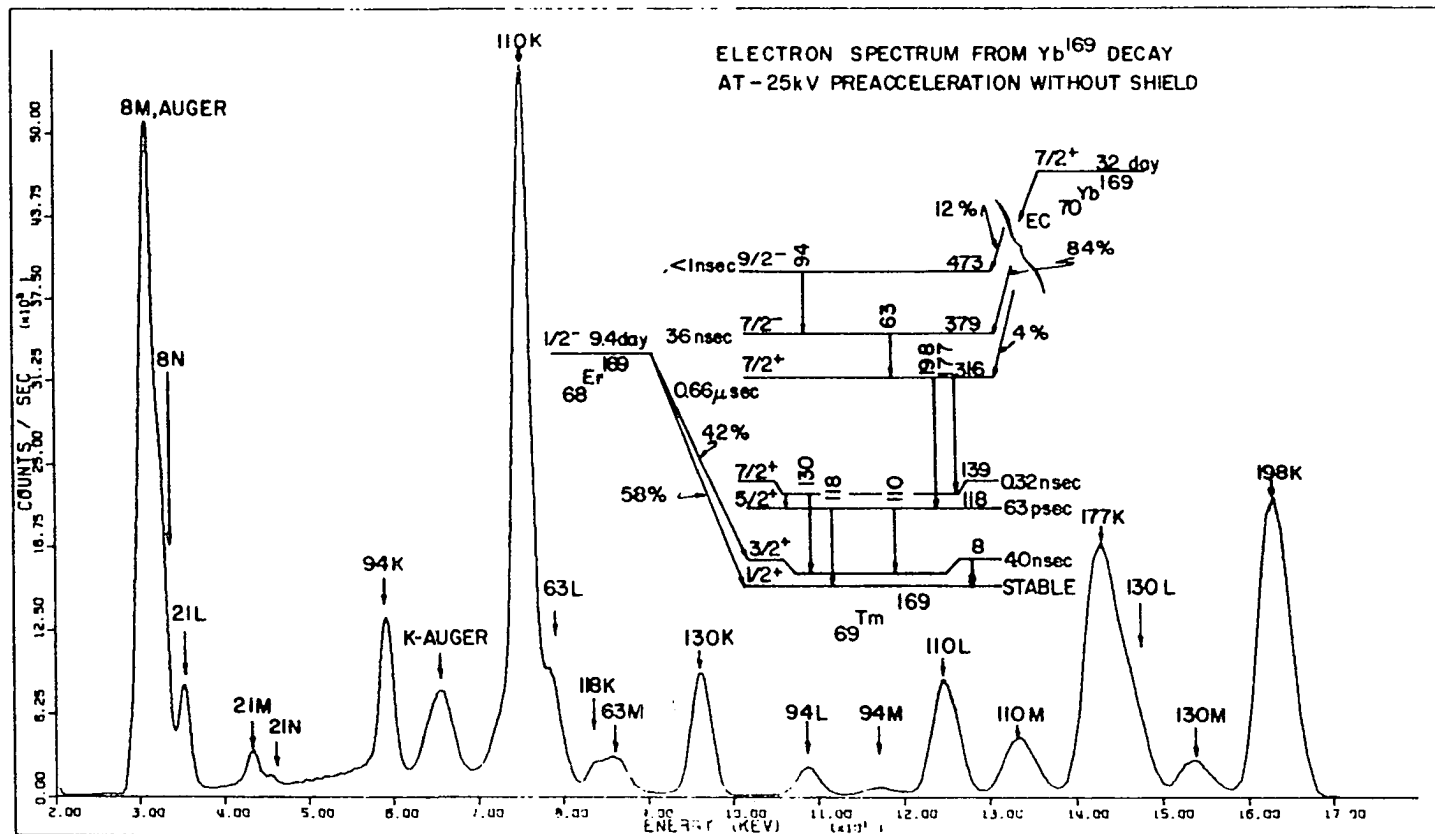


Fig. 10. A portion of the electron spectrum obtained from the  $\text{Yb}^{169}$  decay and a partial decay scheme of the  $\text{Yb}^{169}$  and  $\text{Er}^{169}$  decays. (The source was at a potential of -25 kV. No source shield screen was used.)

Ten delayed-coincidence distributions were used to determine the half-life of the 8.4-keV level in  $\text{Tm}^{169}$ . The source, conversion line, and preacceleration voltage information for these sets of data is given in Table 1 along with the corresponding prompt curve information. Various possible combinations of conversion lines were used to check for discrepancies that could indicate a contaminant activity. No indication of contaminating activity was found.

For D125-P126<sup>1</sup> the spectrometer windows were set on the sides of the appropriate conversion lines in such a fashion that the prompt curve could be obtained without changing the spectrometer currents. The spectrometer currents were also unchanged for D604-P158A. For the other data slightly different energies were focused in the higher energy channel for the prompt and delay curve runs. For D130 and D136 the low-energy-channel spectrometer window was set at different positions along the side of the unresolved peak composed of 8M, 8N, and Auger electrons.

Table 2 gives the results of the maximum-likelihood unfolding analysis of the  $\text{Tm}^{169}$  data. Note the lack of evidence of half-life dependence on the source voltage (see Section XI). The errors indicated in the table are the statistical standard deviations calculated from the individual data sets. The normalized weight is proportional to the inverse square of the calculated standard deviation of the half-life. Figures 11, 12, 13, and 14 give examples of the various types of  $\text{Tm}^{169}$  data obtained and indicate the accuracy of the unfolding procedure. Figures 15 and 16 provide examples of the complete fit including background and display the prompt curve normalized to the same area as the delayed component. The plot of the normalized

---

<sup>1</sup>The notation D125-P126 denotes the data consisting of delay run 125 and prompt run 126.

Table 1 . Source, conversion line, and preacceleration voltage information for the prompt- and delay-data tags associated with the 8-keV level in  $Tm^{169}$

| Delay Tag | Delay Source | Low Energy Line | High Energy Line | Delay Source Voltage (kV) | Prompt Tag | Prompt Source | Low Energy Line | High Energy Line | Prompt Source Voltage (kV) |
|-----------|--------------|-----------------|------------------|---------------------------|------------|---------------|-----------------|------------------|----------------------------|
| 125       | $Yb^{169}$   | 8N              | 110K             | -10.5                     | 126        | $Yb^{169}$    | 20L             | 110K             | -7.8                       |
| 130       | $Yb^{169}$   | 8M-8N           | 110K             | -23                       | 129        | $Yb^{169}$    | 20L             | 110K             | -20.5                      |
| 136       | $Yb^{169}$   | 8M-8N           | 110K             | -20                       | 135        | $Yb^{169}$    | 20L             | 110K             | -17                        |
| 141       | $Yb^{169}$   | 8M              | 110K             | -24                       | 140        | $Yb^{169}$    | 20L             | 110K             | -17                        |
| 143A      | $Yb^{169}$   | 8M              | 110K             | -24                       | 140        | $Yb^{169}$    | 20L             | 110K             | -17                        |
| 143B      | $Yb^{169}$   | 8M              | 110K             | -24                       | 140        | $Yb^{169}$    | 20L             | 110K             | -17                        |
| 146       | $Yb^{169}$   | 8M              | 110L             | -24                       | 145        | $Yb^{169}$    | 20L             | 110L             | -17                        |
| 148       | $Yb^{169}$   | 8M              | 110L             | -20                       | 158A       | $Yb^{169}$    | 110K            | 198K             | +22.7                      |
| 602       | $Er^{169}$   | 8M              | Betas            | -21                       | 152        | $Yb^{169}$    | 20L             | 110L             | -16                        |
| 604       | $Er^{169}$   | 8M              | Betas            | -21                       | 158A       | $Yb^{169}$    | 110K            | 198K             | +22.7                      |

Table 2. Summary of quantities calculated in the maximum-likelihood unfolding analysis of delayed-coincidence distributions involving the lifetime of the 8-keV level in  $\text{Tm}^{169}$  obtained from the  $\text{Yb}^{169}$  and  $\text{Er}^{169}$  decays

| Delay Tag | Prompt Tag | Delay Background | Prompt Admixture  | Half-life (nsec)  | Normalized Weight | Shift (channel)   |
|-----------|------------|------------------|-------------------|-------------------|-------------------|-------------------|
| 125       | 126        | 1985 $\pm$ 4     | 0.375 $\pm$ 0.002 | 4.034 $\pm$ 0.017 | 1.22              | 0.062 $\pm$ 0.010 |
| 130       | 129        | 2363 $\pm$ 5     | 0.420 $\pm$ 0.002 | 4.033 $\pm$ 0.014 | 1.76              | 0.004 $\pm$ 0.007 |
| 136       | 135        | 1207 $\pm$ 3     | 0.452 $\pm$ 0.002 | 4.091 $\pm$ 0.017 | 1.16              | 0.525 $\pm$ 0.006 |
| 141       | 140        | 2215 $\pm$ 5     | 0.498 $\pm$ 0.002 | 4.027 $\pm$ 0.014 | 1.73              | 0.914 $\pm$ 0.004 |
| 143A      | 140        | 1081 $\pm$ 3     | 0.483 $\pm$ 0.002 | 4.043 $\pm$ 0.018 | 1.04              | 0.818 $\pm$ 0.006 |
| 143B      | 140        | 1076 $\pm$ 3     | 0.493 $\pm$ 0.002 | 4.049 $\pm$ 0.019 | 1.00              | 0.789 $\pm$ 0.006 |
| 146       | 145        | 971 $\pm$ 3      | 0.481 $\pm$ 0.002 | 4.062 $\pm$ 0.017 | 1.19              | 0.029 $\pm$ 0.008 |
| 148       | 158A       | 756 $\pm$ 3      | 0.504 $\pm$ 0.002 | 4.004 $\pm$ 0.018 | 1.06              | 0.217 $\pm$ 0.007 |
| 602       | 152        | 177 $\pm$ 2      | 0.139 $\pm$ 0.003 | 4.039 $\pm$ 0.017 | 1.20              | 0.343 $\pm$ 0.024 |
| 604       | 158A       | 40 $\pm$ 1       | 0.081 $\pm$ 0.003 | 4.028 $\pm$ 0.013 | 2.13              | 0.257 $\pm$ 0.037 |

| Delay Tag | Prompt Tag | Delay Counts | Prompt Counts | Prompt Background | Normalized Chi Square | Degrees Freedom | Probability $\chi^2 > \chi^2_{\text{(OBS)}}$ | $\sqrt{\text{Variance of fit}}$ |
|-----------|------------|--------------|---------------|-------------------|-----------------------|-----------------|--|---------------------------------|
| 125       | 126        | 556324       | 157294        | 356               | 0.84                  | 192             | 0.94   | 53                              |
| 130       | 129        | 800947       | 263956        | 512               | 1.68                  | 186             | 0.00   | 84                              |
| 136       | 135        | 476498       | 272103        | 491               | 1.92                  | 187             | 0.00   | 59                              |
| 141       | 140        | 877787       | 364513        | 553               | 1.63                  | 186             | 0.00   | 79                              |
| 143A      | 140        | 440847       | 364513        | 553               | 1.49                  | 186             | 0.00   | 49                              |
| 143B      | 140        | 437587       | 364513        | 553               | 1.85                  | 186             | 0.00   | 55                              |
| 146       | 145        | 535399       | 157206        | 166               | 1.42                  | 192             | 0.00   | 52                              |
| 148       | 158A       | 421775       | 251502        | 159               | 1.18                  | 192             | 0.05   | 37                              |
| 602       | 152        | 171554       | 177599        | 146               | 0.79                  | 192             | 0.98   | 15                              |
| 604       | 158A       | 196113       | 251500        | 158               | 0.65                  | 192             | 0.99   | 7                               |

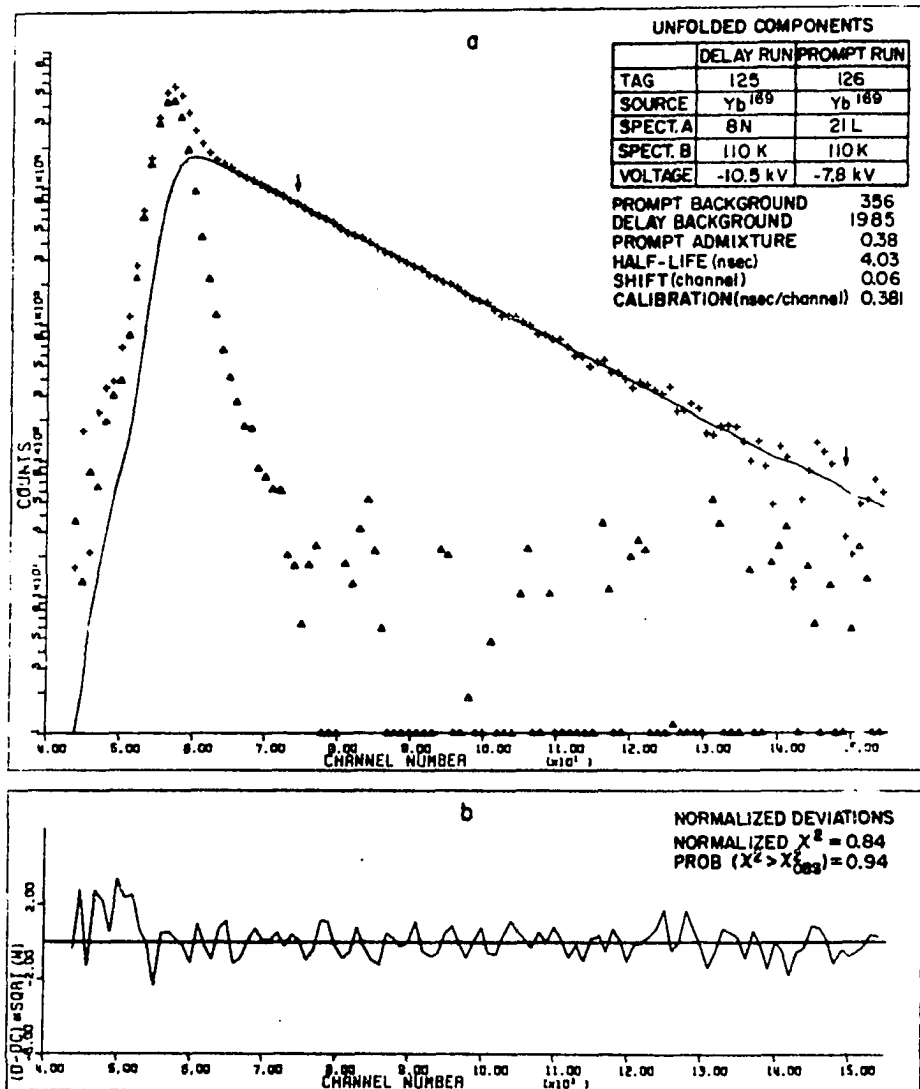


Fig. 11. Delay curve for the 8.4-keV level in  $Tm^{169}$  via the 8N and 110K transitions in the  $Yb^{169}$  decay. (a. Plus signs represent the delay data minus background. Triangles represent the shifted prompt normalized to the calculated prompt admixture. The solid line is the unfolded delayed component. The arrows indicate the region used for logarithmic slope analysis. The left arrow also locates the lower channel limit for the exponential tail fit; the other limit is off scale to the right. b. The normalized deviations from the data of the composite fit.)

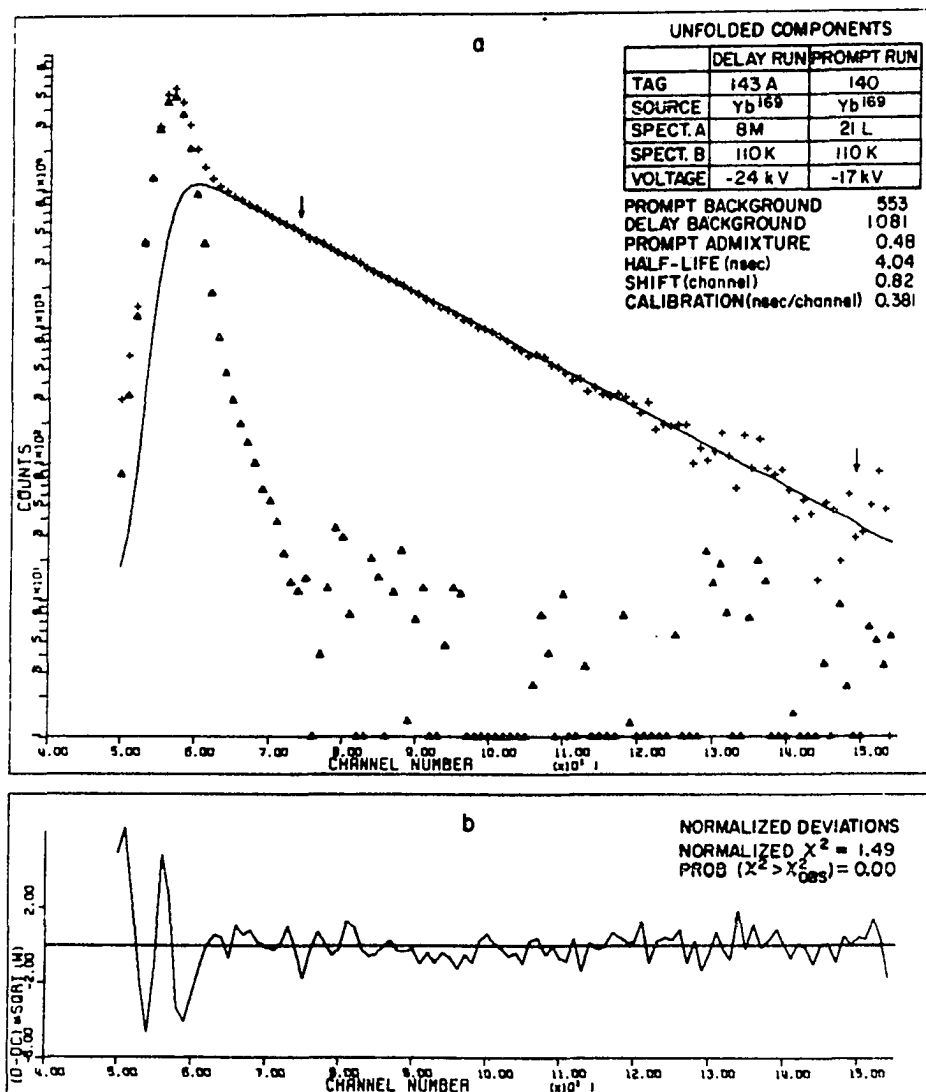


Fig. 12. Delay curve for the 8.4-keV level in  $Tm^{169}$  via the 8M and 110K transitions in the  $Yb^{169}$  decay. (a. Plus signs represent the delay data minus background. Triangles represent the shifted prompt normalized to the calculated prompt admixture. The solid line is the unfolded delayed component. The arrows indicate the region used for logarithmic slope analysis. The left arrow also locates the lower channel limit for the exponential tail fit; the other limit is off scale to the right. b. The normalized deviations from the data of the composite fit.)

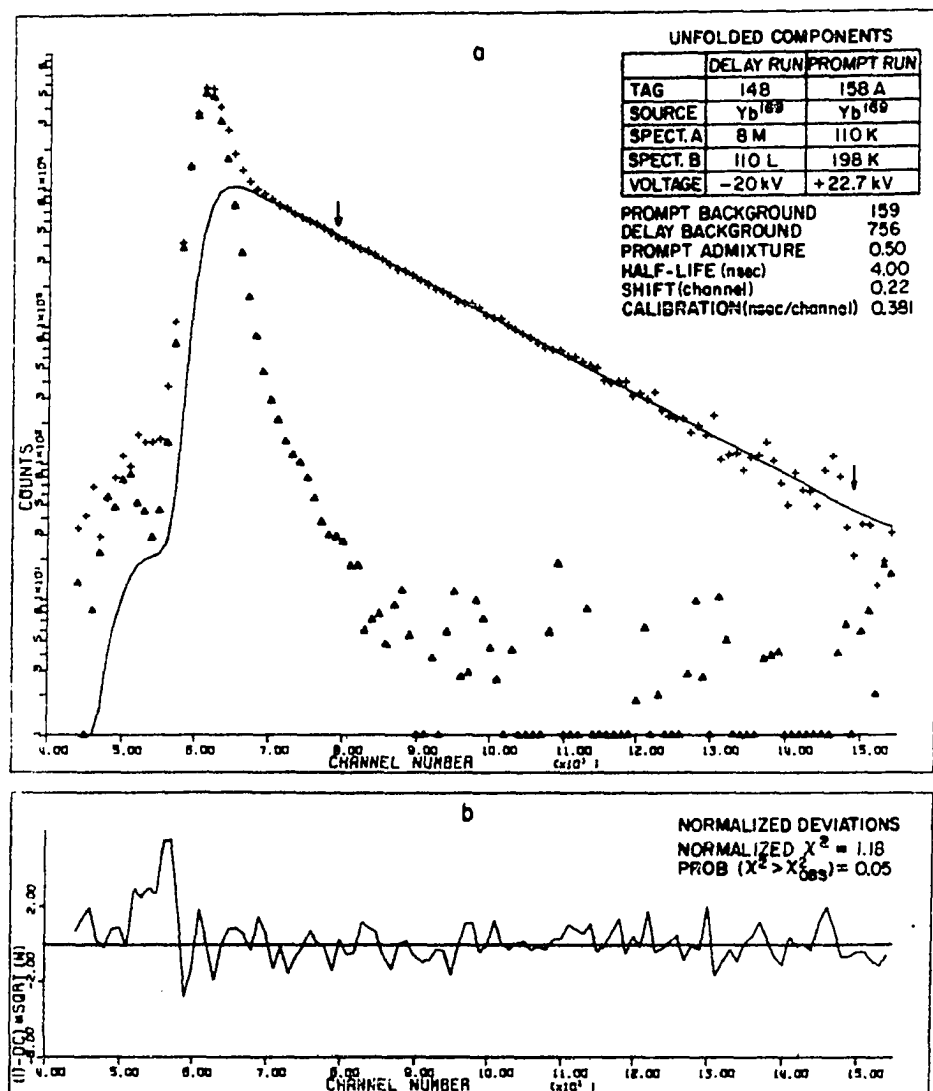


Fig. 13. Delay curve for the 8.4-keV level in  $Tm^{169}$  via the 8M and 110L transitions in the  $Yb^{169}$  decay. (a. Plus signs represent the delay data minus background. Triangles represent the shifted prompt normalized to the calculated prompt admixture. The solid line is the unfolded delayed component. The arrows indicate the region used for logarithmic slope analysis. The left arrow also locates the lower channel limit for the exponential tail fit; the other limit is off scale to the right. b. The normalized deviations from the data of the composite fit.)



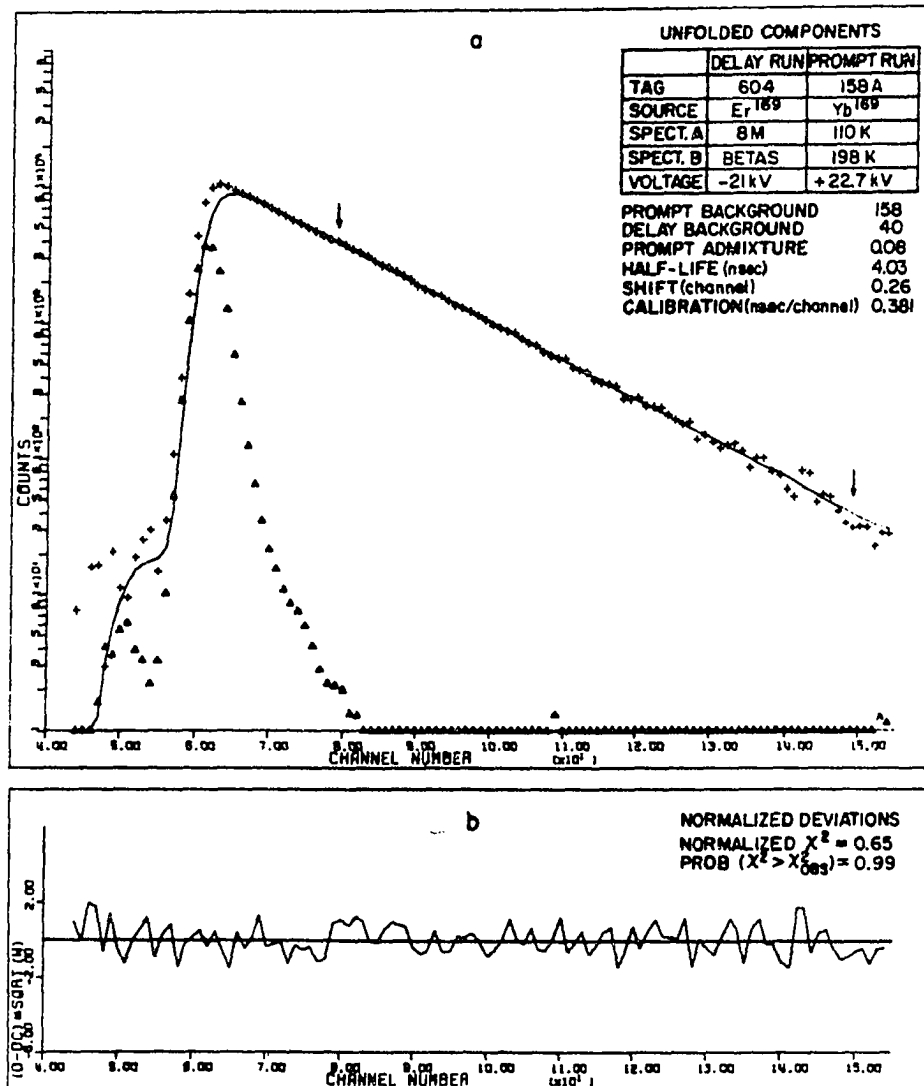


Fig. 14. Delay curve for the 8.4-keV level in  $\text{Tm}^{169}$  via the 8M transition and betas in the  $\text{Er}^{169}$  decay. (a. Plus signs represent the delay data minus background. Triangles represent the shifted prompt normalized to the calculated prompt admixture. The solid line is the unfolded delayed component. The arrows indicate the region used for logarithmic slope analysis. The left arrow also locates the lower channel limit for the exponential tail fit; the other limit is off scale to the right. b. The normalized deviations from the data of the composite fit.)

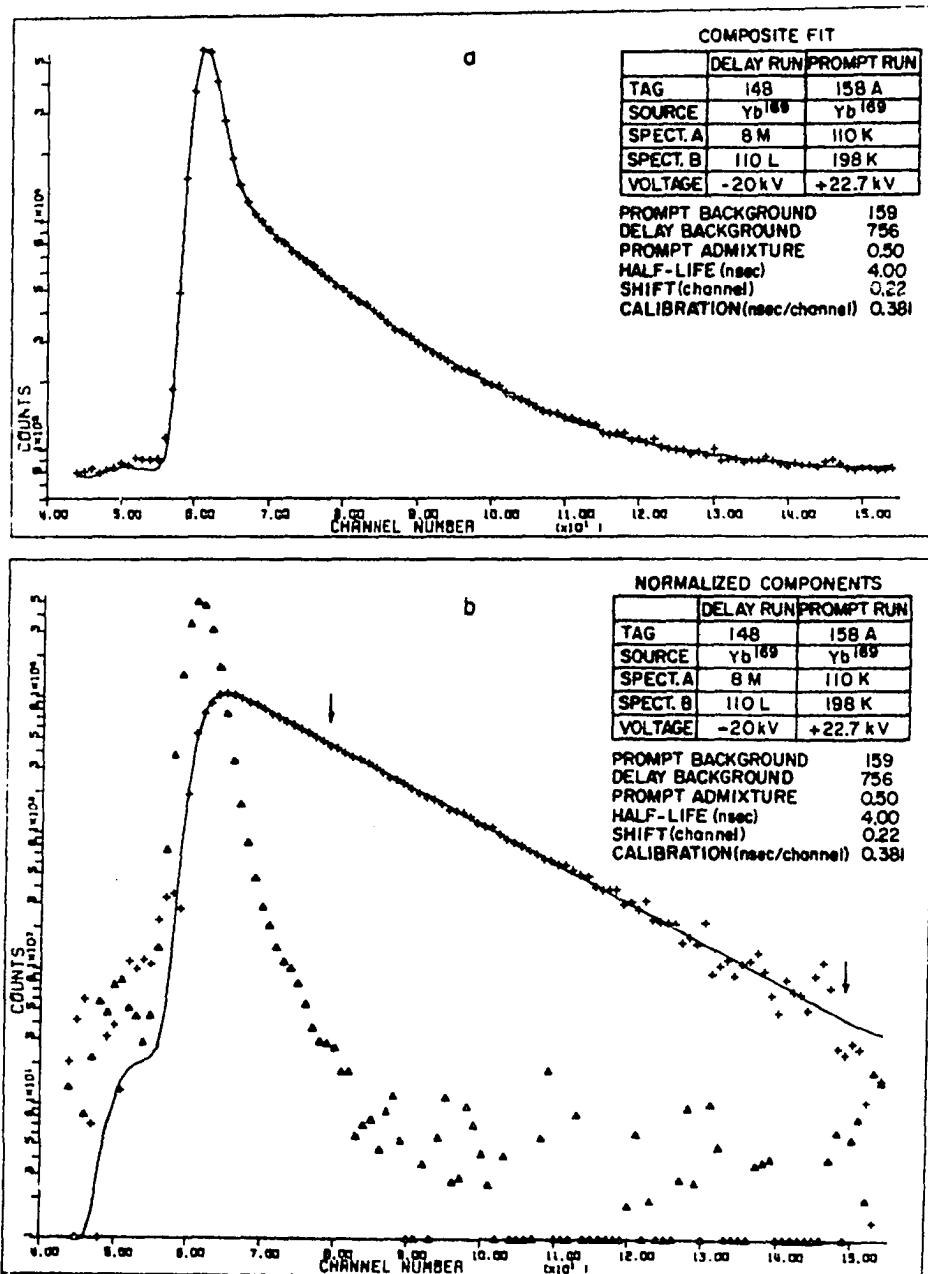


Fig. 15. Delay curve for the 8.4-keV level in  $Tm^{169}$  via the 8M and 110L transitions in the  $Yb^{169}$  decay and a corresponding prompt curve via the 110K and 198K transitions in the  $Yb^{169}$  decay. (a. Plus signs represent the delay data. The solid line is the calculated composite fit. b. Triangles represent the shifted prompt data normalized to the area of the calculated delayed component. Plus signs represent the delay data minus the calculated prompt component. The line is the calculated delayed component.)

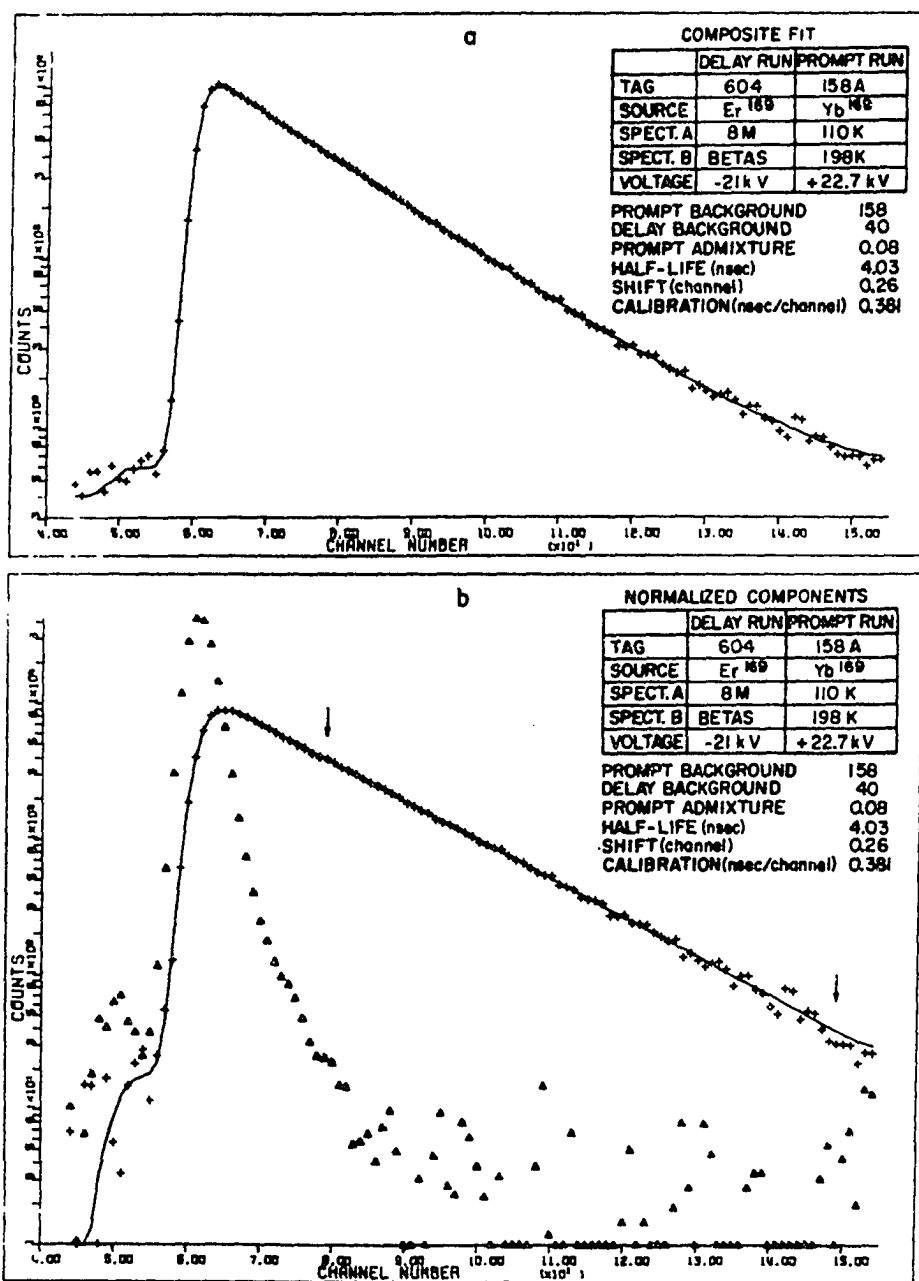


Fig. 16. Delay curve for the 8.4-keV level in  $\text{Tm}^{169}$  via the 8M transition and betas in the  $\text{Er}^{169}$  decay and a corresponding prompt curve via the 110K and 198K transitions in the  $\text{Yb}^{169}$  decay. (a. Plus signs represent the delay data. The solid line is the calculated composite fit. b. Triangles represent the shifted prompt data normalized to the area of the calculated delayed component. Plus signs represent the delay data minus the calculated prompt component. The line is the calculated delayed component.)

components makes it quite easy to assign or check slope analysis limits. The usable range of the MCPHA consisted of about 240 channels for the  $T_m^{169}$  (and  $T_m^{171}$ ) measurements and provided an ample background estimation region which does not appear in the figures. Also the  $T_m^{169}$  (and  $T_m^{171}$ ) data have been inverted to get time delay increasing with channel number for convenience in data analysis.

Table 3 presents the results of the maximum-likelihood fit of an exponential plus constant background to the tail portion of the  $T_m^{169}$  delayed-coincidence distributions.

Table 4 gives the results of the linear least-squares fit to the logarithms of the tail portion of the  $T_m^{169}$  delayed-coincidence distributions. The accidental-coincidence estimation region was always chosen sufficiently far out in the positive delay direction to avoid any detectable contribution from true delayed events (cf. Tables 2, 3, and 4).

The individual half-life results obtained by the different analysis procedures were averaged. These averages are given for comparison in Table 5 along with various statistical quantities. A comparison of the  $T_m^{169}$  results in Table 5 with the  $T_m^{171}$  and  $Cs^{134}$  results in Tables 11 and 15 gives no indication of a significant systematic high or low trend associated with any of the methods. The adopted value is, therefore, taken to be the weighted average of the results of the different analysis methods calculated as indicated in Table 5.

The final value adopted for the half-life of the 8.4-keV level in  $T_m^{169}$  is  $(4.04 \pm 0.06)$  nsec. The error assignment is the sum of the estimated limit of the systematic error, 0.02 nsec, and the computed standard error, 0.04 nsec. The systematic 0.43% error limit is the root-

Table 3. Summary of quantities calculated in the maximum-likelihood fit of an exponential plus constant background to the tail portion of delayed-coincidence distributions involving the lifetime of the 8-keV level in  $\text{Tm}^{169}$  obtained from the  $\text{Yb}^{169}$  and  $\text{Er}^{169}$  decays

| Delay Tag | Constant Background | Initial Height | Half-Life (nsec)  | Normalized Weight | Normalized Chi Square | Degrees Freedom | Probability $\chi^2 > \chi^2_{\text{(OBS)}}$ | $\sqrt{\text{Variance of fit}}$ |
|-----------|---------------------|----------------|-------------------|-------------------|-----------------------|-----------------|--|---------------------------------|
| 125       | 1978 $\pm$ 5        | 7478 $\pm$ 42  | 4.042 $\pm$ 0.028 | 1.40              | 0.65                  | 163             | 0.99   | 39                              |
| 130       | 2353 $\pm$ 5        | 7129 $\pm$ 42  | 4.095 $\pm$ 0.031 | 1.14              | 0.63                  | 163             | 0.99   | 42                              |
| 136       | 1206 $\pm$ 4        | 5052 $\pm$ 34  | 4.043 $\pm$ 0.033 | 1.02              | 0.68                  | 163             | 0.99   | 31                              |
| 141       | 2201 $\pm$ 5        | 9585 $\pm$ 47  | 4.041 $\pm$ 0.024 | 1.93              | 0.66                  | 163             | 0.99   | 42                              |
| 143A      | 1076 $\pm$ 3        | 4934 $\pm$ 33  | 4.029 $\pm$ 0.032 | 1.06              | 0.61                  | 163             | 1.00   | 28                              |
| 143B      | 1070 $\pm$ 3        | 4792 $\pm$ 32  | 4.043 $\pm$ 0.033 | 1.00              | 0.69                  | 163             | 0.99   | 30                              |
| 146       | 962 $\pm$ 3         | 5456 $\pm$ 34  | 4.016 $\pm$ 0.029 | 1.29              | 0.65                  | 158             | 0.99   | 28                              |
| 148       | 747 $\pm$ 3         | 4443 $\pm$ 30  | 4.069 $\pm$ 0.032 | 1.06              | 0.55                  | 158             | 1.00   | 23                              |
| 602       | 178 $\pm$ 2         | 3247 $\pm$ 23  | 4.044 $\pm$ 0.029 | 1.28              | 0.73                  | 158             | 0.99   | 13                              |
| 604       | 40 $\pm$ 1          | 3912 $\pm$ 24  | 3.991 $\pm$ 0.021 | 2.49              | 0.56                  | 158             | 1.00   | 6                               |

Table 4. Summary of quantities calculated in the linear least-squares fit to the logarithms of the tail portion, after subtraction of a constant background, of delayed-coincidence distributions involving the lifetime of the 8-keV level in  $\text{Tm}^{169}$  obtained from the  $\text{Yb}^{169}$  and  $\text{Er}^{169}$  decays

| Delay Tag | Constant Background | Half-Life (nsec)  | Normalized Weight | Normalized Chi Square | Degrees Freedom | Probability $\chi^2 > \chi^2_{\text{(OBS)}}$ | $\sqrt{\text{Variance of Fit}}$ | Delay Counts |
|-----------|---------------------|-------------------|-------------------|-----------------------|-----------------|--|---------------------------------|--------------|
| 125       | 1982                | $4.022 \pm 0.069$ | 1.40              | 0.65                  | 163             | 0.99   | 39                              | 556939       |
| 130       | 2342                | $4.108 \pm 0.077$ | 1.13              | 0.67                  | 163             | 0.99   | 43                              | 805154       |
| 136       | 1205                | $4.035 \pm 0.082$ | 1.00              | 0.68                  | 163             | 0.99   | 31                              | 476790       |
| 141       | 2198                | $4.040 \pm 0.058$ | 1.98              | 0.67                  | 163             | 0.99   | 42                              | 881310       |
| 143A      | 1081                | $4.007 \pm 0.080$ | 1.06              | 0.62                  | 163             | 1.00   | 28                              | 440867       |
| 143B      | 1071                | $4.021 \pm 0.082$ | 1.01              | 0.69                  | 163             | 0.99   | 30                              | 438674       |
| 146       | 962                 | $4.005 \pm 0.071$ | 1.33              | 0.65                  | 158             | 0.99   | 28                              | 537365       |
| 148       | 746                 | $4.065 \pm 0.078$ | 1.09              | 0.56                  | 158             | 1.00   | 23                              | 423945       |
| 602       | 176                 | $4.034 \pm 0.069$ | 1.42              | 0.74                  | 158             | 0.99   | 14                              | 171251       |
| 604       | 42                  | $3.982 \pm 0.049$ | 2.85              | 0.61                  | 158             | 1.00   | 7                               | 195654       |

Table 5. Comparison of the average half-life values and statistical quantities associated with the different analysis procedures for the ten delayed-coincidence distributions involving the lifetime of the 8-keV level in  $\text{Tm}^{169}$

| Analysis Procedure  | UNWTAV <sup>a</sup><br>(nsec) | WTAV <sup>b</sup><br>(nsec) | SIGUU <sup>c</sup> | SIGWW <sup>d</sup>              | SIGMUU <sup>e</sup> | SIGMWW <sup>f</sup> | SUMW <sup>g</sup><br>(10 <sup>5</sup> ) | SIGMSW <sup>h</sup> |
|---|-------------------------------|-----------------------------|--------------------|---------------------------------|---------------------|---------------------|---|---------------------|
| Maximum-Likelihood Unfolding                              | 4.041                         | 4.039                       | 0.0232             | 0.0219                          | 0.00734             | 0.00691             | 0.3903                                  | 0.00506             |
| Maximum-Likelihood Exponential-Plus-Constant Tail Fit     | 4.041                         | 4.036                       | 0.0280             | 0.0300                          | 0.00884             | 0.00950             | 0.1258                                  | 0.00892             |
| Linear Least-Squares Fit to the Logarithmic Slope of Tail | 4.032                         | 4.026                       | 0.0351             | 0.0358                          | 0.01108             | 0.01132             | 2.121                                   | 0.02171             |
| Weighted Average <sup>i</sup>                             |                               |                             | 4.036              | Standard Deviation <sup>j</sup> |                     |                     | 0.00924                                 |                     |

<sup>a</sup>Unweighted average of half-life values

<sup>b</sup>Weighted average of half-life values

<sup>c</sup>Unweighted standard deviation of values from the unweighted average

<sup>d</sup>Weighted standard deviation of values from the weighted average

<sup>e</sup>Standard deviation in the unweighted mean of ten values ( $\text{SIGUU}/\sqrt{10}$ )

<sup>f</sup>Standard deviation in the weighted mean of ten values ( $\text{SIGWW}/\sqrt{10}$ )

<sup>g</sup>Sum of the unnormalized weights used to determine the weighted average

<sup>h</sup>Standard deviation in the weighted average calculated from  $1/\sqrt{\text{SUMW}}$

<sup>i</sup>Weighted average of the WTAV values; weights used were based on the SIGMWW values

<sup>j</sup>Estimated standard deviation is unweighted average of the SIGMWW values

sum-square of the following:

1. a 0.25% error limit for the time calibration and linearity correction (see Sections III.D.7. and III.D.8),
2. a 0.15% error limit representing the maximum variation of the unfolded half-life result with different weighting formulas for a typical set of data (see reference (88)), and
3. a 0.32% error limit representing the maximum variation of the half-life result for different methods of analysis (see Table 5).

The computed standard error is the product  $4.3 \times 0.0092$  where 4.3 is Student's  $t$  for nine degrees of freedom and a 99.6% confidence interval, and where 0.0092 is the estimated standard deviation in the weighted average calculated as indicated in Table 5.

A comparison of the results of this investigation with the values obtained by other experimenters is shown in Fig. 17. The numerical values are also tabulated in Table 6. Reported values which were apparently preliminary in nature have not been included in either Fig. 17 or Table 6. The order of presentation in both cases is reverse chronological. Measurements 1, 3 and 5 were made with magnetic energy discrimination and preacceleration; measurements 2, 6 and 8 utilized back-to-back scintillation counters; and measurements 4 and 7 were performed with a parallel-plate avalanche counter opposite a scintillation counter. The present work agrees within error only with measurements 3 and 8.

For most of the reported values there is not enough information available about the experimental work to allow full explanation of the individual discrepancies. However, the existence of the discrepancies



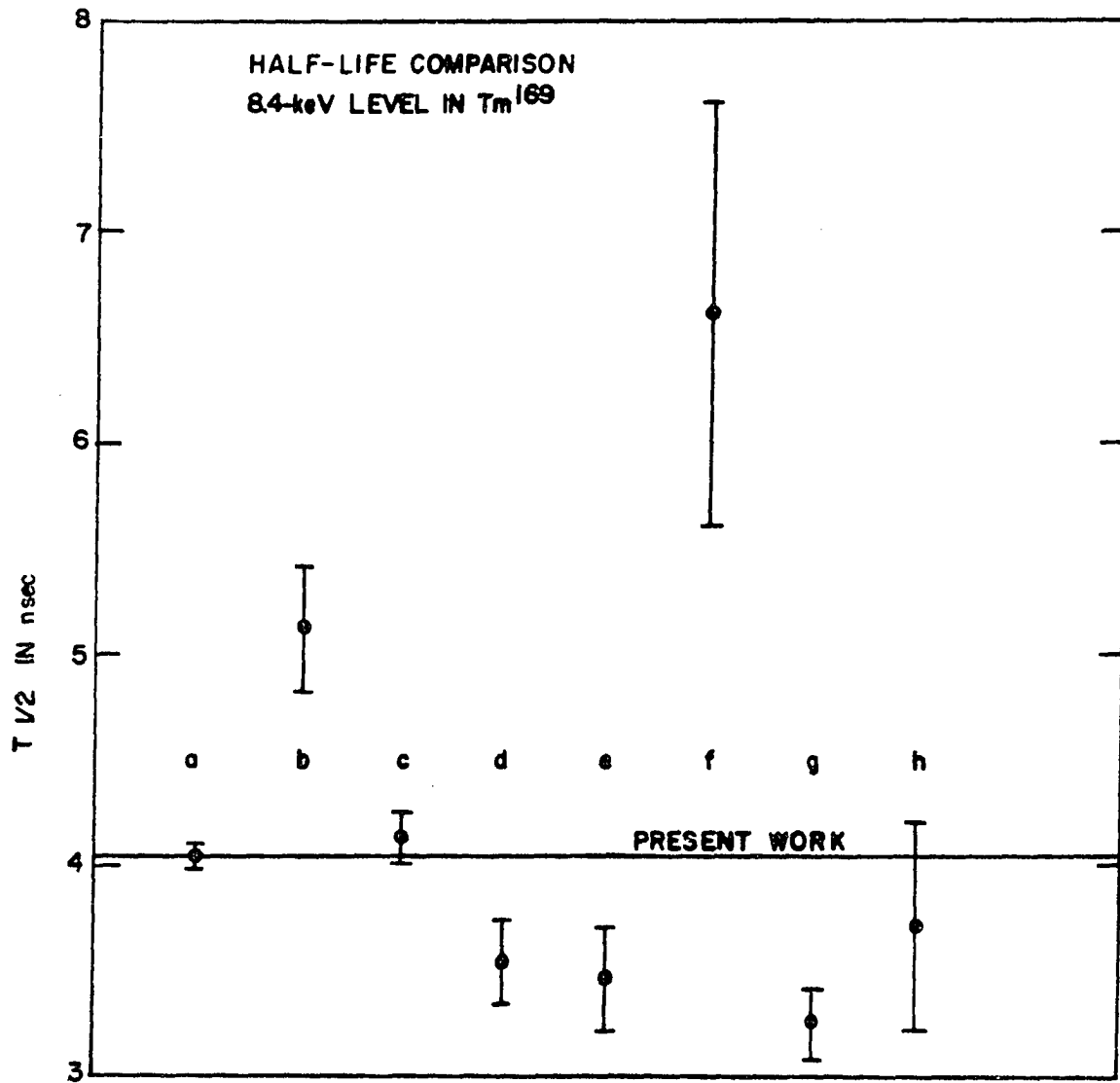


Fig. 17. Comparison of the half-life values of the 8.4-keV level in  $Tm^{169}$  reported by different experimenters. (a. Present work, b. Begzhanov *et al.* (91), c. McAdams *et al.* (35), d. Bloess and Münnich (47), e. Sundstrom *et al.* (92), f. Hauser *et al.* (93), g. Blechschmidt *et al.* (94), and h. Beekhuis and de Waard (95). The horizontal line indicates the value obtained in the present work.)

Table 6. Half-life values of the 8.4-keV level in  $\text{Tm}^{169}$  reported by different experimenters

| Measurement | Half-life<br>(nsec) | Experimenter                    |
|-------------|---------------------|---------------------------------|
| 1           | $4.04 \pm 0.06$     | Present work                    |
| 2           | $5.12 \pm 0.30$     | Begzhanov <u>et al.</u> (91)    |
| 3           | $4.13 \pm 0.12$     | McAdams <u>et al.</u> (35)      |
| 4           | $3.53 \pm 0.20$     | Bloess and Münnich (47)         |
| 5           | $3.45 \pm 0.25$     | Sundström <u>et al.</u> (92)    |
| 6           | $6.6 \pm 1.0$       | Hauser <u>et al.</u> (93)       |
| 7           | $3.24 \pm 0.17$     | Blechschiidt <u>et al.</u> (94) |
| 8           | $3.7 \pm 0.5$       | Beekhuis and de Waard (95)      |

is not surprising for numerous reasons. The poor energy resolution of scintillation counters and total lack of energy resolution in the parallel-plate avalanche counter has been discussed in Section III.B.. All of the measurements prior to the present work had significantly poorer time resolution and in some cases non-negligible asymmetry and tailing in the prompt curve. The time calibrations in the older measurement were generally obtained with calibrated delay cables and are somewhat subject to suspicion depending on the method and care employed in their calibration. The older measurements were performed with equipment which was probably unstable and which had a much narrower "linear" range. These properties required shorter runs with poorer statistics, allowed observation of the decay over far fewer half-lives, and made background determination by a separate run necessary. Also no nonlinearity correction was used. In addition the effects of prompt curve broadness, asymmetry, and tailing were ignored with naive application of the slope method of analysis. Another possible source of error would be the use of the negative time delay region for accidental-coincidence background estimation. This region is expected to contain true delayed coincidences due to Auger electrons which are associated with transitions above the 316 keV level ( $T_{1/2} = 0.66 \mu\text{sec}$ ) and which, therefore, precede the 110 keV transition. Also, centroid-shift analysis of data such as shown in Fig. 14 would result in too low a value due to the hidden prompt admixture. This prompt admixture is attributed to L-Auger electrons associated with internal ionization during  $\beta$  decay (96). Some speculations regarding specific measurements have been given by McAdams and Hatch (34) and need not be repeated.

Previously the most disturbing discrepancy was that between measurements 2 and 5 which were both obtained with magnetic energy discrimination and preacceleration. It lead McAdams and Hatch (34) to conclude that "measurements by other investigators using the general methods used in this investigation and used by Sundström et al. would be especially desirable." The only parts of the experimental apparatus common to the present investigation and that of McAdams et al. were the magnetic spectrometers. In spite of the almost completely different instrumentation and experimental procedures these independent investigations agree within error and the change in value can be explained by improvements in calibration and by nonlinearity correction (see Sections III. D.8. and III.D.9). In view of the precision of the present measurements and the considerable care taken to optimize system performance and to eliminate possible sources of systematic error it is believed that the value reported here is correct.

#### B. The 5.0-keV Level in $\text{Tm}^{171}$

The half-life of the 5.0-keV level in  $\text{Tm}^{171}$  was investigated through the beta decay of  $\text{Er}^{171}$ . The decay scheme features (41,97) of importance to the present investigation are presented in Fig.18 along with an electron spectrum of the  $\text{Er}^{171}$  decay obtained at a preacceleration voltage of -25 kV without the source shield screen. Segmented scans of the  $\text{Er}^{171}$  spectrum at -25 kV preacceleration both with and without the shield screen are shown in Fig. 5. All of these scans were taken with the low-energy-channel spectrometer at the same baffle settings as used in all the lifetime measurements. The discriminator threshold settings and detector operation conditions were not the same so one

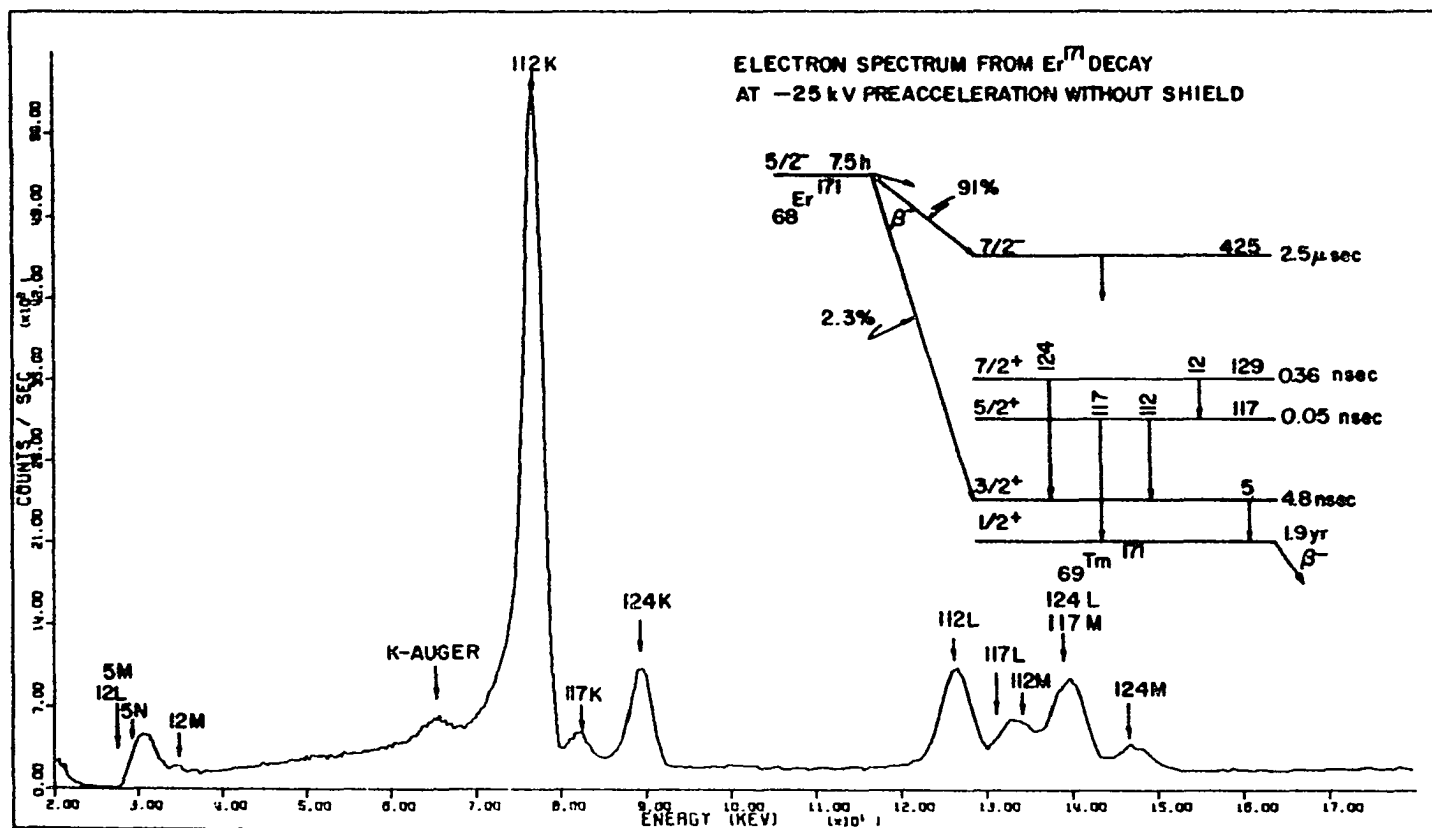


Fig. 18. A portion of the electron spectrum obtained from the  $\text{Er}^{171}$  decay and a partial decay scheme of the  $\text{Er}^{171}$  decay. (The source was at a potential of -25 kV. No source shield screen was used for this data.)

should be careful to avoid drawing invalid conclusions concerning relative intensities and counting efficiencies.

Eleven delayed-coincidence distributions were used to determine the half-life of the 5.0-keV level in  $\text{Tm}^{171}$ . The source, conversion line, and preacceleration voltage information for these sets of data is given in Table 7 along with the corresponding prompt curve information. Various possible combinations of conversion lines were used to check for discrepancies that could indicate a contaminant activity. No indication of contaminating activity was found.

For D411B-P154 the current in the high-energy-channel spectrometer was kept constant while the energy focused in the low-energy-channel spectrometer differed by 32% in the delay and prompt runs. The change was from 27.5- to 36.2-keV, respectively. In spite of this significant energy variation a good fit was obtained with the unfolding analysis (see Table 8). For all the other data sets the current in the low-energy-channel spectrometer was kept constant in the prompt and delay runs (see Section III.D.9).

Table 8 gives the results of the maximum-likelihood unfolding analysis of the  $\text{Tm}^{171}$  data. Figures 19, 20, 21, and 22 give examples of the various types of  $\text{Tm}^{171}$  data obtained and indicate the accuracy of the unfolding procedure. Figure 23 is included to indicate the nature of the data and fit obtained for the worst combination of poor statistics and high chi square. Figure 24 provides an example of the complete fit including background and displays the prompt curve normalized to the same area as the delayed component.

Tables 9 presents the results of the maximum-likelihood fits of an

Table 7 . Source, conversion line, and preacceleration voltage information for the prompt- and delay-data tags associated with the 5-keV level in  $Tm^{171}$

| Delay Tag | Delay Source      | Low Energy Line | High Energy Line | Delay Source Voltage (kV) | Prompt Tag | Prompt Source     | Low Energy Line | High Energy Line | Prompt Source Voltage (kV) |
|-----------|-------------------|-----------------|------------------|---------------------------|------------|-------------------|-----------------|------------------|----------------------------|
| 401       | Er <sup>171</sup> | 5N              | 112K             | -25                       | 135        | Yb <sup>169</sup> | 20L             | 110K             | -17                        |
| 405       | Er <sup>171</sup> | 5M              | 112K             | -25                       | 135        | Yb <sup>169</sup> | 20L             | 110K             | -17                        |
| 406       | Er <sup>171</sup> | 5N              | 112K             | -25                       | 135        | Yb <sup>169</sup> | 20L             | 110K             | -17                        |
| 408       | Er <sup>171</sup> | 5N              | 112K             | -25                       | 140        | Yb <sup>169</sup> | 20L             | 110K             | -17                        |
| 409       | Er <sup>171</sup> | 5M              | 112K             | -25                       | 140        | Yb <sup>169</sup> | 20L             | 110K             | -17                        |
| 410       | Er <sup>171</sup> | 5M              | 112L             | -25                       | 145        | Yb <sup>169</sup> | 20L             | 110L             | -17                        |
| 411B      | Er <sup>171</sup> | 5M              | 112L             | -25                       | 154        | Yb <sup>169</sup> | 20L             | 110L             | -26                        |
| 412       | Er <sup>171</sup> | 5M              | 112L             | -25                       | 158A       | Yb <sup>169</sup> | 110K            | 198K             | +22.7                      |
| 413A      | Er <sup>171</sup> | 5N              | 112L             | -23                       | 158B       | Yb <sup>169</sup> | 110K            | 198K             | +22.7                      |
| 413B      | Er <sup>171</sup> | 5N              | 112L             | -23                       | 158B       | Yb <sup>169</sup> | 110K            | 198K             | +22.7                      |
| 414       | Er <sup>171</sup> | 5N              | 112L             | -23                       | 158B       | Yb <sup>169</sup> | 110K            | 198K             | +22.7                      |

Table 8. Summary of quantities calculated in the maximum-likelihood unfolding analysis of delayed-coincidence distributions involving the lifetime of the 5-keV level in  $\text{Tm}^{171}$  obtained from the  $\text{Er}^{171}$  decay

| Delay Tag | Prompt Tag | Delay Background | Prompt Admixture  | Half-life (nsec)  | Normalized Weight | Shift (channel)   |
|-----------|------------|------------------|-------------------|-------------------|-------------------|-------------------|
| 401       | 135        | 30 $\pm$ 1       | 0.734 $\pm$ 0.002 | 4.927 $\pm$ 0.057 | 1.18              | 1.347 $\pm$ 0.008 |
| 405       | 135        | 288 $\pm$ 2      | 0.366 $\pm$ 0.002 | 4.776 $\pm$ 0.015 | 17.76             | 2.487 $\pm$ 0.006 |
| 406       | 135        | 14 $\pm$ 1       | 0.799 $\pm$ 0.002 | 4.858 $\pm$ 0.062 | 1.00              | 0.783 $\pm$ 0.006 |
| 408       | 140        | 121 $\pm$ 2      | 0.761 $\pm$ 0.002 | 4.792 $\pm$ 0.045 | 1.83              | 1.077 $\pm$ 0.006 |
| 409       | 140        | 86 $\pm$ 1       | 0.399 $\pm$ 0.002 | 4.753 $\pm$ 0.022 | 8.01              | 2.225 $\pm$ 0.010 |
| 410       | 145        | 63 $\pm$ 1       | 0.413 $\pm$ 0.003 | 4.869 $\pm$ 0.035 | 3.01              | 1.799 $\pm$ 0.010 |
| 411B      | 154        | 70 $\pm$ 1       | 0.402 $\pm$ 0.002 | 4.764 $\pm$ 0.022 | 7.68              | 4.132 $\pm$ 0.009 |
| 412       | 158A       | 634 $\pm$ 3      | 0.427 $\pm$ 0.002 | 4.793 $\pm$ 0.017 | 12.47             | 1.155 $\pm$ 0.007 |
| 413A      | 158B       | 181 $\pm$ 2      | 0.766 $\pm$ 0.002 | 4.726 $\pm$ 0.047 | 1.71              | 0.863 $\pm$ 0.005 |
| 413B      | 158B       | 132 $\pm$ 2      | 0.762 $\pm$ 0.002 | 4.834 $\pm$ 0.039 | 2.50              | 0.807 $\pm$ 0.005 |
| 414       | 158B       | 270 $\pm$ 2      | 0.757 $\pm$ 0.002 | 4.785 $\pm$ 0.036 | 2.98              | 0.862 $\pm$ 0.004 |

| Delay Tag | Prompt Tag | Delay Counts | Prompt Counts | Prompt Background | Normalized Chi Square | Degrees Freedom | Probability $\chi^2 > \chi^2_{\text{(OBS)}}$ | $\sqrt{\text{Variance of fit}}$ |
|-----------|------------|--------------|---------------|-------------------|-----------------------|-----------------|--|---------------------------------|
| 401       | 135        | 96624        | 272073        | 491               | 1.59                  | 192             | 0.00   | 11                              |
| 405       | 135        | 496444       | 272036        | 491               | 1.34                  | 192             | 0.00   | 31                              |
| 406       | 135        | 110992       | 272103        | 491               | 1.66                  | 192             | 0.00   | 11                              |
| 408       | 140        | 223183       | 364546        | 553               | 1.06                  | 192             | 0.27   | 18                              |
| 409       | 140        | 203903       | 364542        | 553               | 0.81                  | 192             | 0.97   | 12                              |
| 410       | 145        | 88088        | 157212        | 166               | 1.12                  | 187             | 0.13   | 11                              |
| 411B      | 154        | 196956       | 183299        | 156               | 1.11                  | 187             | 0.14   | 14                              |
| 412       | 158A       | 500818       | 251529        | 159               | 0.81                  | 187             | 0.97   | 30                              |
| 413A      | 158B       | 209585       | 268834        | 173               | 1.16                  | 187             | 0.06   | 19                              |
| 413B      | 158B       | 270125       | 268834        | 173               | 1.52                  | 187             | 0.00   | 21                              |
| 414       | 158B       | 374469       | 268834        | 173               | 1.31                  | 187             | 0.00   | 28                              |



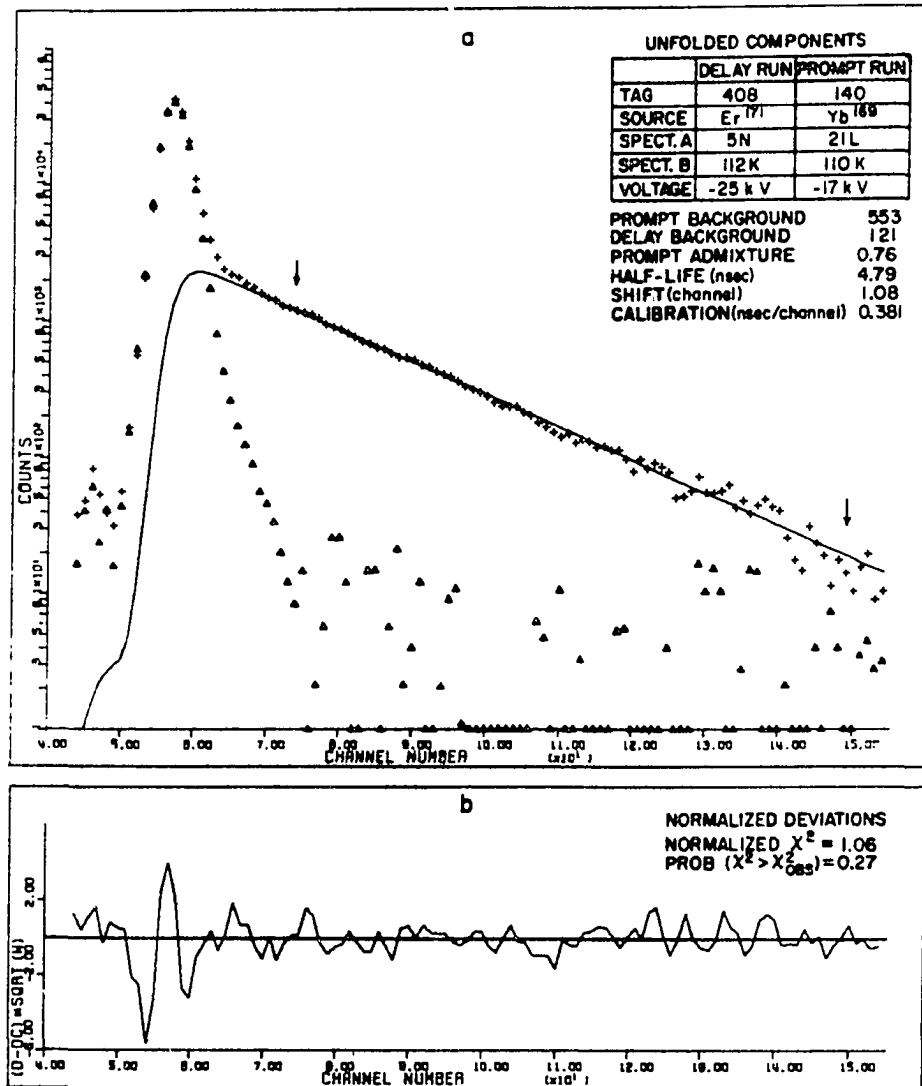


Fig. 19. Delay curve for the 5.0-keV level in  $\text{Tm}^{171}$  via the 5N and 112K transitions in the  $\text{Er}^{171}$  decay. (a. Plus signs represent the delay data minus background. Triangles represent the shifted prompt normalized to the calculated prompt admixture. The solid line is the unfolded delayed component. The arrows indicate the region used for logarithmic slope analysis. The left arrow also locates the lower channel limit for the exponential tail fit; the other limit is off scale to the right. b. The normalized deviations from the data of the composite fit.)

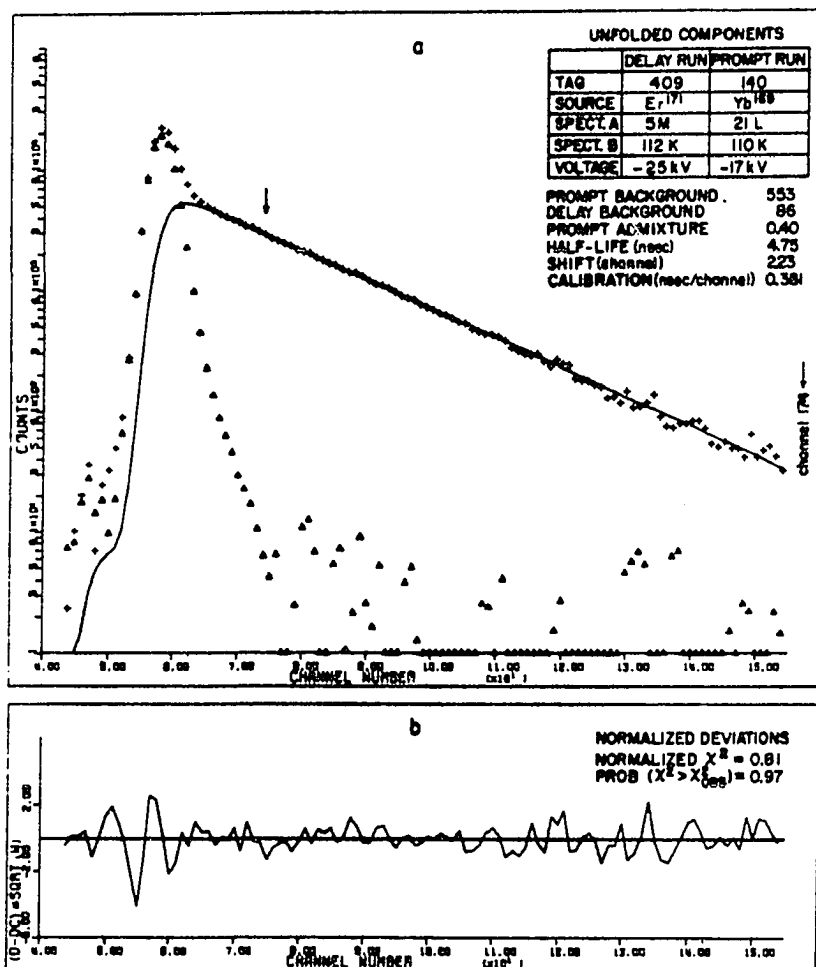


Fig. 20. Delay curve for the 5.0-keV level in  $Tm^{171}$  via the 5M and 112K transitions in the  $Er^{171}$  decay. (a. Plus signs represent the delay data minus background. Triangles represent the shifted prompt normalized to the calculated prompt admixture. The solid line is the unfolded delayed component. The arrows indicate the region used for logarithmic slope analysis. The left arrow also locates the lower channel limit for the exponential tail fit; the other limit is off scale to the right. b. The normalized deviations from the data of the composite fit.)

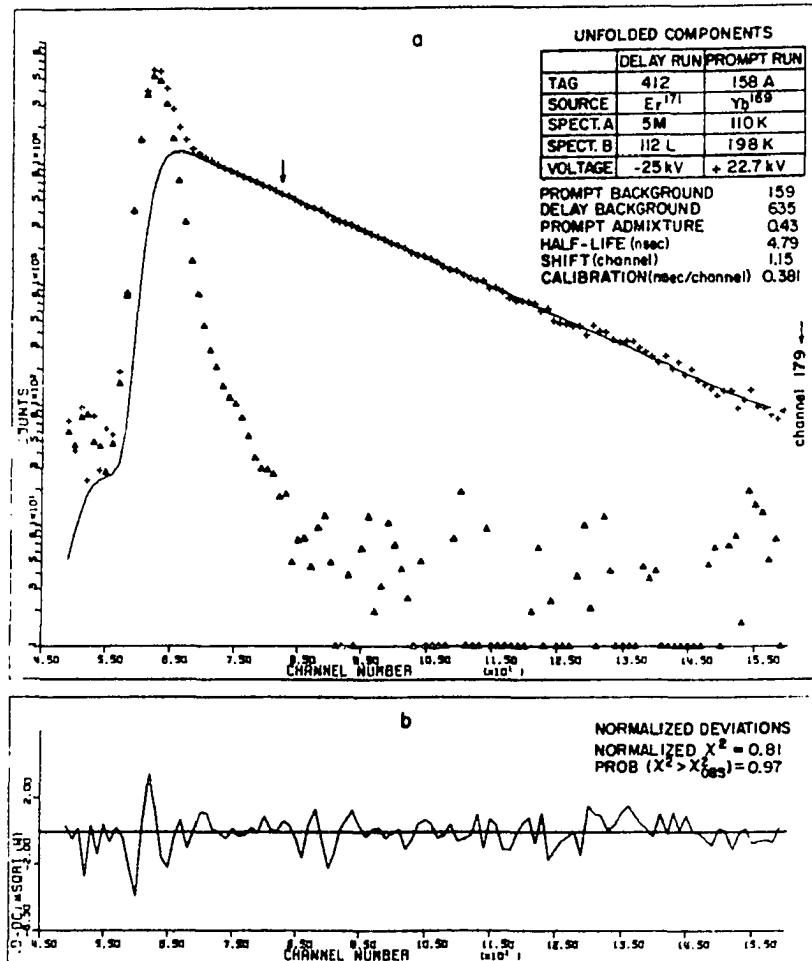


Fig. 21. Delay curve for the 5.0-keV level in  $Tm^{171}$  via the 5M and 112L transitions in the  $Er^{171}$  decay. (a. Plus signs represent the delay data minus background. Triangles represent the shifted prompt normalized to the calculated prompt admixture. The solid line is the unfolded delayed component. The arrows indicate the region used for logarithmic slope analysis. The left arrow also locates the lower channel limit for the exponential tail fit; the other limit is off scale to the right. b. The normalized deviations from the data of the composite fit.)

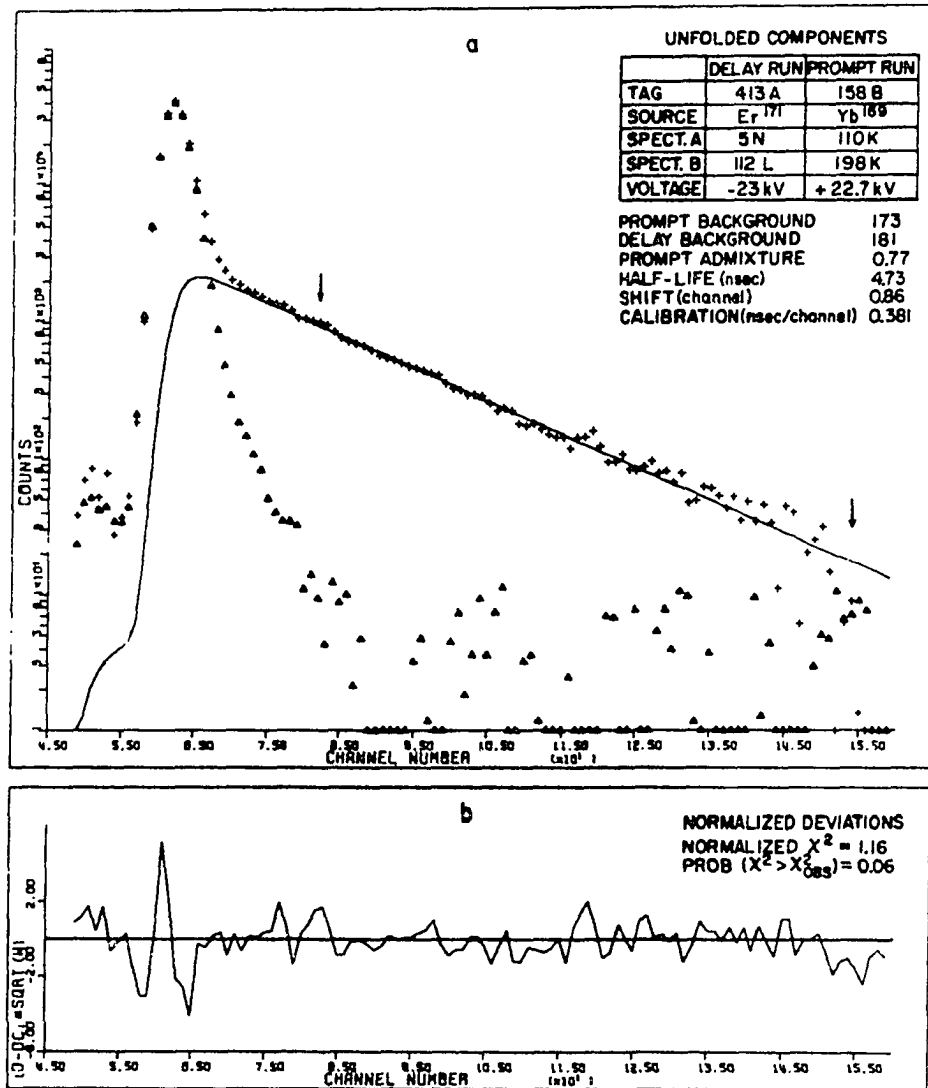


Fig. 22. Delay curve for the 5.0-keV level in  $Tm^{171}$  via the 5N and 112L transitions in the  $Er^{171}$  decay. (a. Plus signs represent the delay data minus background. Triangles represent the shifted prompt normalized to the calculated prompt admixture. The solid line is the unfolded delayed component. The arrows indicate the region used for logarithmic slope analysis. The left arrow also locates the lower channel limit for the exponential tail fit; the other limit is off-scale to the right. b. The normalized deviations from the data of the composite fit.)

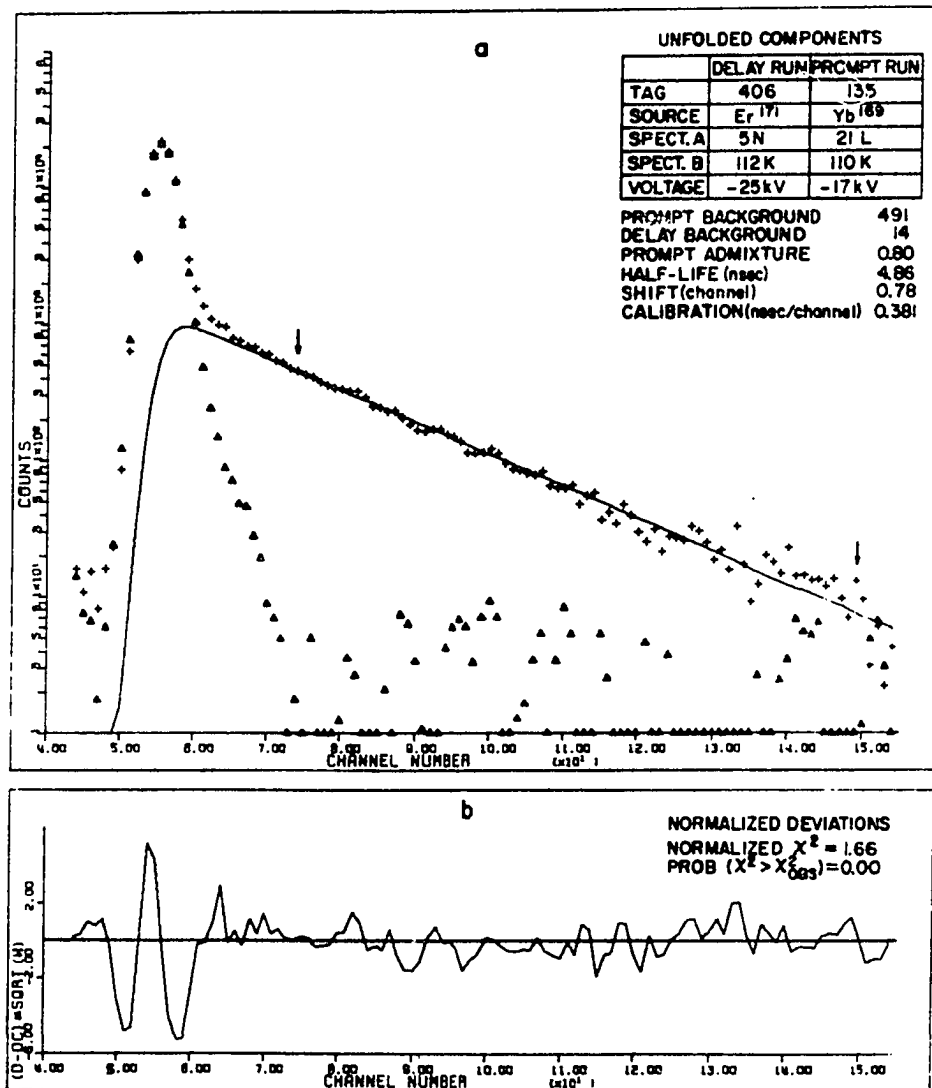


Fig. 23. A "worst case" delay curve for the 5.0-keV level in  $Tm^{171}$  via the 5N and 112K transitions in the  $Er^{171}$  decay. (a. Plus signs represent the delay data minus background. Triangles represent the shifted prompt normalized to the calculated prompt admixture. The solid line is the unfolded delayed component. The arrows indicate the region used for logarithmic slope analysis. The left arrow also locates the lower channel limit for the exponential tail fit; the other limit is off scale to the right. b. The normalized deviations from the data of the composite fit.)

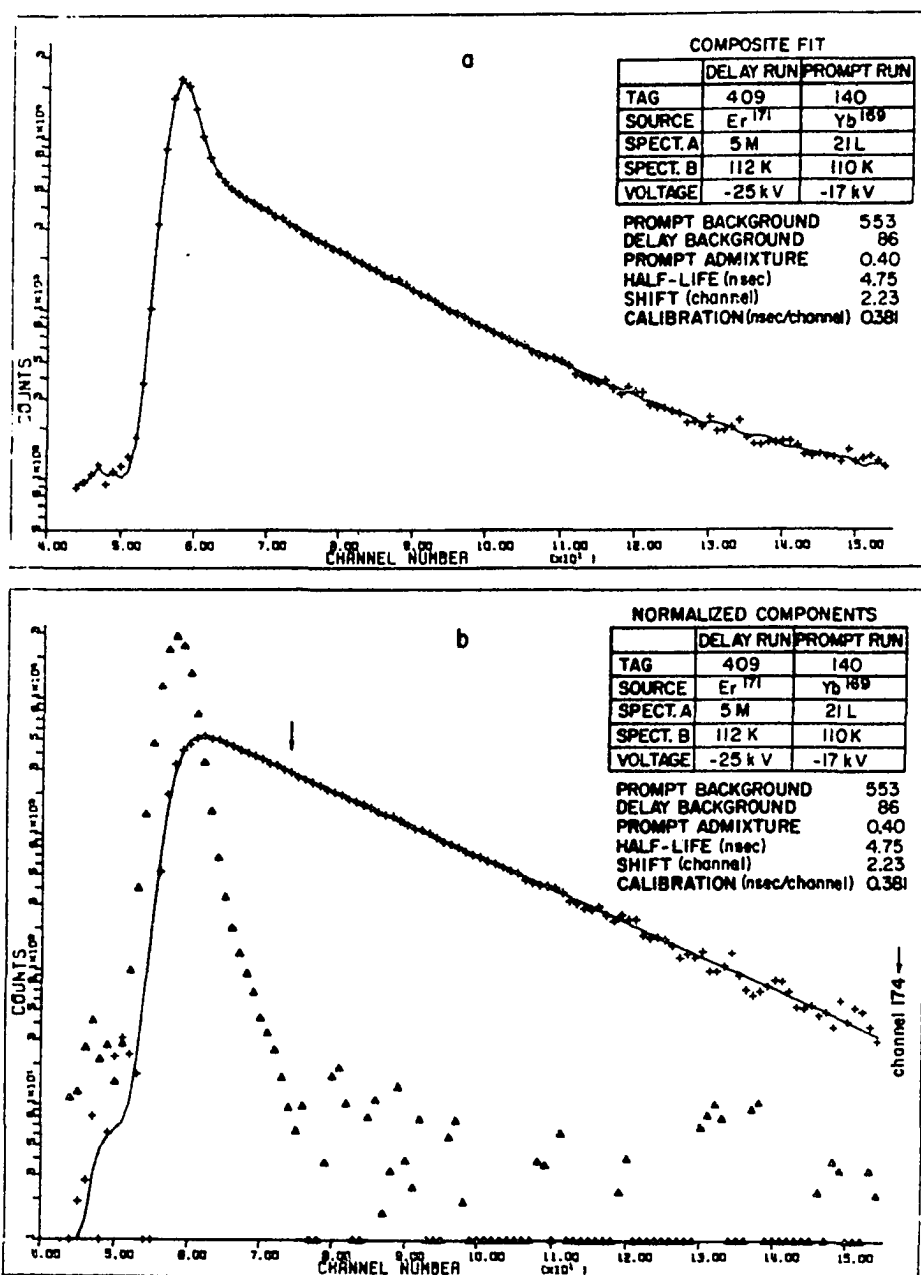


Fig. 24. Delay curve for the 5.0-keV level in  $Tm^{171}$  via the 5M and 112K transitions in the  $Er^{171}$  decay and a corresponding prompt curve via the 21L and 110K transitions in the  $Yb^{169}$  decay. (a. Plus signs represent the delay data. The solid line is the calculated composite fit. b. Triangles represent the shifted prompt data normalized to the area of the calculated delayed component. Plus signs represent the delay data minus the calculated prompt component. The line is the calculated delayed component.)

Table 9. Summary of quantities calculated in the maximum-likelihood fit of an exponential plus constant background to the tail portion of delayed-coincidence distributions involving the lifetime of the 5-keV level in  $\text{Tm}^{171}$  obtained from the  $\text{Er}^{171}$  decay

| Delay Tag | Constant Background | Initial Height | Half-Life (nsec)  | Normalized Weight | Normalized Chi Square | Degrees Freedom | Probability $\chi^2 > \chi^2_{\text{(OBS)}}$ | $\sqrt{\text{Variance of Fit}}$ |
|-----------|---------------------|----------------|-------------------|-------------------|-----------------------|-----------------|--|---------------------------------|
| 401       | $30 \pm 1$          | $525 \pm 8$    | $4.875 \pm 0.082$ | 1.00              | 0.58                  | 163             | 1.00   | 5                               |
| 405       | $287 \pm 2$         | $6856 \pm 31$  | $4.779 \pm 0.022$ | 14.65             | 0.61                  | 163             | 1.00   | 17                              |
| 406       | $14 \pm 1$          | $447 \pm 8$    | $4.759 \pm 0.079$ | 1.08              | 0.66                  | 163             | 0.99   | 4                               |
| 408       | $120 \pm 1$         | $1193 \pm 14$  | $4.720 \pm 0.060$ | 1.86              | 0.54                  | 163             | 1.00   | 9                               |
| 409       | $86 \pm 1$          | $2868 \pm 19$  | $4.750 \pm 0.031$ | 7.04              | 0.69                  | 163             | .99  | 10                              |
| 410       | $63 \pm 1$          | $974 \pm 12$   | $4.723 \pm 0.061$ | 1.80              | 0.61                  | 155             | 1.00   | 8                               |
| 411B      | $70 \pm 1$          | $2165 \pm 17$  | $4.785 \pm 0.037$ | 4.95              | 0.52                  | 155             | 1.00   | 8                               |
| 412       | $636 \pm 3$         | $5481 \pm 30$  | $4.792 \pm 0.030$ | 7.62              | 0.68                  | 155             | 0.99   | 24                              |
| 413A      | $180 \pm 2$         | $932 \pm 13$   | $4.687 \pm 0.081$ | 1.02              | 0.67                  | 155             | 0.99   | 12                              |
| 413B      | $132 \pm 1$         | $1240 \pm 14$  | $4.735 \pm 0.061$ | 1.83              | 0.65                  | 155             | 0.99   | 11                              |
| 414       | $268 \pm 2$         | $1706 \pm 17$  | $4.821 \pm 0.058$ | 2.04              | 0.69                  | 155             | 0.99   | 16                              |

exponential plus constant background to the tail portion of the  $T_m^{171}$  delayed-coincidence distributions.

Table 10 gives the results of the linear least-squares fit to the logarithms of the tail portion of the  $T_m^{171}$  delayed-coincidence distributions after subtraction of a constant background. The accidental-coincidence estimation region was always chosen sufficiently far out in the positive delay direction to avoid any detectable contribution from true delayed events (cf. Tables 8, 9, and 10).

The individual half-life results obtained by the different analysis procedures were averaged. These results are given for comparison in Table 11 along with various statistical quantities. A comparison of the  $T_m^{171}$  results in Table 11 with the  $T_m^{169}$  and  $Cs^{134}$  results in Tables 5 and 15 gives no indication of a significant systematic high or low trend associated with any of the methods. The adopted value is, therefore, taken to be the weighted average of the results of the different analysis methods calculated as indicated in Table 11.

The final value adopted for the half-life of the 5.0-keV level in  $T_m^{171}$  is  $(4.77 \pm 0.08)$  nsec. The error assignment is the sum of the estimated limit of systematic error, 0.03 nsec, and the computed standard error, 0.05 nsec. The systematic 0.61% error limit is the root-sum-square of the following:

- 1) a 0.25% error limit for the time calibration and linearity correction (see Sections III.D.7. and III.D.8),
- 2) a 0.15% error limit representing the maximum variation of the unfolded half-life result with different weighting formulas for a typical set of data (see reference (88)), and



Table 10. Summary of quantities calculated in the linear least-squares fit to the logarithms of the tail portion, after subtraction of a constant background, of delayed-coincidence distributions involving the lifetime of the 5-keV level in  $\text{Tm}^{171}$  obtained from the  $\text{Er}^{171}$  decay

| Delay Tag | Constant Background | Half-Life (nsec)  | Normalized Weight | Normalized Chi Square | Degrees Freedom | Probability $\chi^2 > \chi^2_{\text{(OBS)}}$ | $\sqrt{\text{Variance of Fit}}$ | Delay Counts |
|-----------|---------------------|-------------------|-------------------|-----------------------|-----------------|--|---------------------------------|--------------|
| 401       | 32                  | $4.819 \pm 0.199$ | 1.00              | 0.61                  | 163             | 1.00   | 5                               | 96277        |
| 405       | 292                 | $4.754 \pm 0.049$ | 16.80             | 0.65                  | 163             | 0.99   | 17                              | 495579       |
| 406       | 15                  | $4.685 \pm 0.185$ | 1.16              | 0.74                  | 163             | 0.99   | 4                               | 110702       |
| 408       | 120                 | $4.707 \pm 0.142$ | 1.95              | 0.54                  | 163             | 1.00   | 9                               | 223363       |
| 409       | 87                  | $4.740 \pm 0.070$ | 8.03              | 0.69                  | 163             | 0.99   | 10                              | 203770       |
| 410       | 64                  | $4.670 \pm 0.149$ | 1.77              | 0.61                  | 155             | 1.00   | 8                               | 87810        |
| 411B      | 70                  | $4.769 \pm 0.084$ | 5.61              | 0.52                  | 155             | 1.00   | 8                               | 196832       |
| 412       | 627                 | $4.819 \pm 0.069$ | 8.33              | 0.73                  | 155             | 0.99   | 25                              | 502300       |
| 413A      | 180                 | $4.668 \pm 0.195$ | 1.04              | 0.67                  | 155             | 0.99   | 12                              | 209818       |
| 413B      | 130                 | $4.727 \pm 0.143$ | 1.92              | 0.67                  | 155             | 0.99   | 11                              | 270655       |
| 414       | 265                 | $4.829 \pm 0.138$ | 2.07              | 0.70                  | 155             | 0.99   | 16                              | 375363       |

Table 11. Comparison of the average half-life values and statistical quantities associated with the different analysis procedures for the eleven delayed-coincidence distributions involving the lifetime of the 5-keV level in  $Tm^{171}$

| Analysis Procedure  | UNWTAV <sup>a</sup><br>(nsec) | WTAV <sup>b</sup><br>(nsec) | SIGUU <sup>c</sup>              | SIGWW <sup>d</sup> | SIGMUU <sup>e</sup> | SIGMWW <sup>f</sup> | SUMW <sup>g</sup><br>(10 <sup>4</sup> ) | SIGMSW <sup>h</sup> |
|---|-------------------------------|-----------------------------|---------------------------------|--------------------|---------------------|---------------------|---|---------------------|
| Maximum-Likelihood Unfolding                              | 4.807                         | 4.786                       | 0.0589                          | 0.0373             | 0.0178              | 0.0112              | 1.589                                   | 0.00793             |
| Maximum-Likelihood Exponential-Plus-Constant Tail Fit     | 4.766                         | 4.772                       | 0.0525                          | 0.0325             | 0.0158              | 0.0098              | 0.6619                                  | 0.0123              |
| Linear Least-Squares Fit to the Logarithmic Slope of Tail | 4.744                         | 4.760                       | 0.0596                          | 0.0431             | 0.0180              | 0.0130              | 0.1256                                  | 0.0282              |
| Weighted Average  |                               | 4.774 <sup>i</sup>          | Standard Deviation <sup>j</sup> |                    | 0.0113              |                     |   |                     |

<sup>a</sup> Unweighted average of half-life values.

<sup>b</sup> Weighted average of half-life values.

<sup>c</sup> Unweighted standard deviation of values from the unweighted average.

<sup>d</sup> Weighted standard deviation of values from the weighted average.

<sup>e</sup> Standard deviation in the unweighted mean of eleven values ( $SIGUU/\sqrt{11}$ ).

<sup>f</sup> Standard deviation in the weighted mean of eleven values ( $SIGWW/\sqrt{11}$ ).

<sup>g</sup> Sum of the unnormalized weights used to determine the weighted average.

<sup>h</sup> Standard deviation in the weighted average calculated from  $1/\sqrt{SUMW}$ .

<sup>i</sup> Weighted average of the WTAV values; weights used were based on the SIGMWW values.

<sup>j</sup> Estimated standard deviation is unweighted average of the SIGMWW values.

3) a 0.54% error limit representing the maximum variation of the half-life result for different methods of analysis (see Table 11). The computed standard error is the product  $4.2 \times 0.011$  where 4.2 is Student's  $t$  for 10 degrees of freedom and a 99.6% confidence interval, and where 0.011 is the estimated standard deviation in the weighted average calculated as indicated in Table 11.

A comparison of the result of this investigation with the values obtained by other experimenters is shown in Fig. 25. The numerical values are also tabulated in Table 12. Preliminary values have not been included. The order of presentation is reverse chronological in both cases. Measurement 2 was made with back-to-back scintillation counters; measurement 3 was performed with a parallel-plate avalanche counter opposite a scintillation counter. The present work agrees with neither of the other two measurements.

Table 12. Half-life values of the 5.0-keV level in  $Tm^{171}$  reported by different experimenters

| Measurement | Half-life<br>(nsec) | Experimenter                     |
|-------------|---------------------|----------------------------------|
| 1           | $4.77 \pm 0.08$     | Present work                     |
| 2           | $2.88 \pm 0.27$     | Begzhanov <u>et al.</u> (91)     |
| 3           | $3.76 \pm 0.14$     | Blechsmidt <u>et al.</u><br>(94) |

The general observations given in Section IV.A. regarding possible systematic effects, which could explain discrepancies in the  $Tm^{169}$  measurements, also apply to the previous  $Tm^{171}$  measurements. In

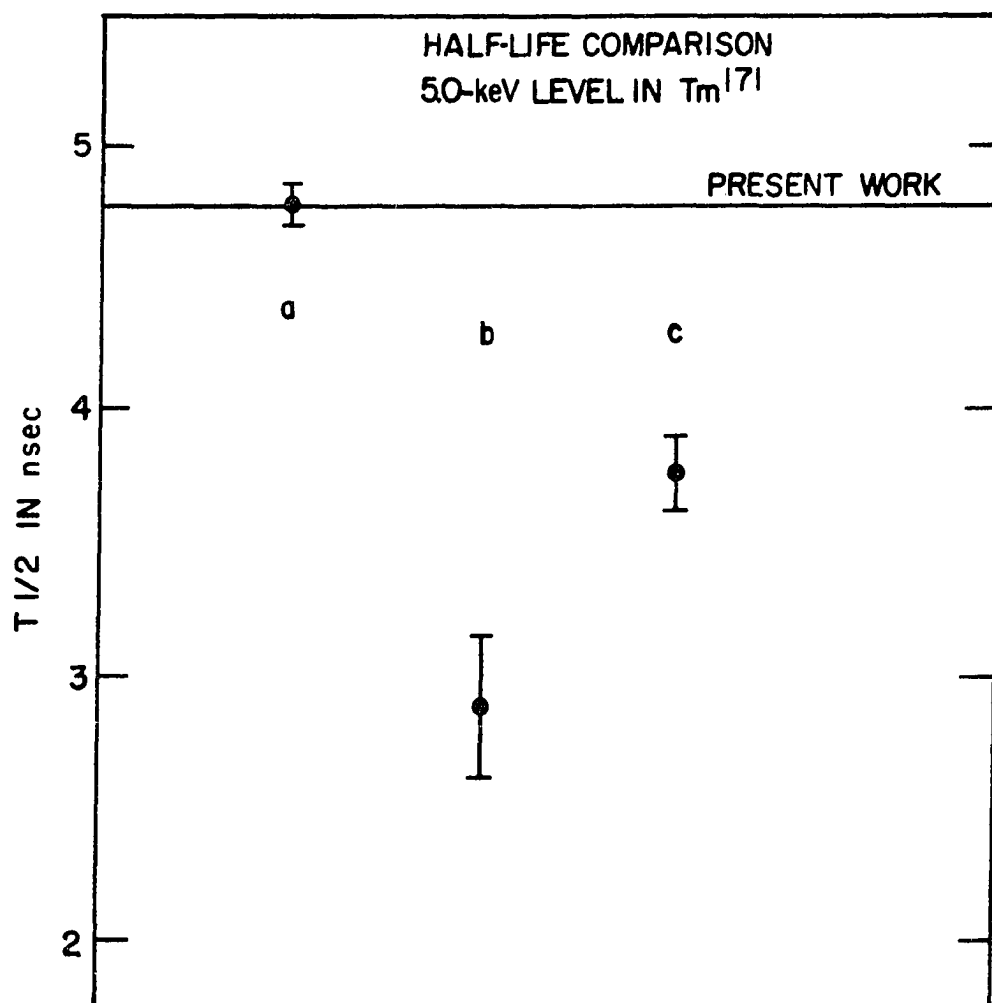


Fig. 25. Comparison of the half-life values of the 5.0-keV level in  $Tm^{171}$  reported by different experimenters. (a. Present work, b. Begzhanov *et al.* (91), and c. Blechsmidt *et al.* (94). The horizontal line indicates the value obtained in the present work.)

addition it may be noted that the asymmetry of the prompt curve associated with measurement 2 which is shown in (91) is certainly not suitable for slope analysis. However, it is hard to explain how such a prompt curve could lead to a low slope-analysis half-life. In view of the precision of the present measurements and the considerable care taken to optimize system performance and to eliminate possible sources of systematic error it is believed that the value reported here is correct.

### C. The 11-keV Level in $\text{Cs}^{134}$

The half-life of the 11-keV level in  $\text{Cs}^{134}$  was investigated via the decay of  $\text{Cs}^{134m}$ . The decay scheme features (41, 98) of importance to the present investigation are presented in Fig. 26 along with an electron spectrum obtained with a shielded  $\text{Cs}^{134m}$  source at a preacceleration voltage of -25 kV.

Four delayed-coincidence distributions were used to determine the lifetime of the 11-keV level in  $\text{Cs}^{134}$ . All the data was obtained by observing the 11L conversion electrons in coincidence with the 127L conversion electrons. A 25-kV preacceleration voltage was used in all cases. Due to the large calibration constant used to observe the long half-life over several lifetimes, the prompt curve fell mainly in two channels and unfolding analysis was neither possible nor necessary,

Table 13 presents the results of the maximum-likelihood fit of an exponential plus constant background to the tail portion of the  $\text{Cs}^{134}$  delayed-coincidence distributions. Figure 27 gives an example of the type of data obtained and indicates the accuracy of the maximum-likelihood exponential-plus-constant tail fit. The data extends to channel 240.

Table 14 presents the results of the linear least-squares fit to

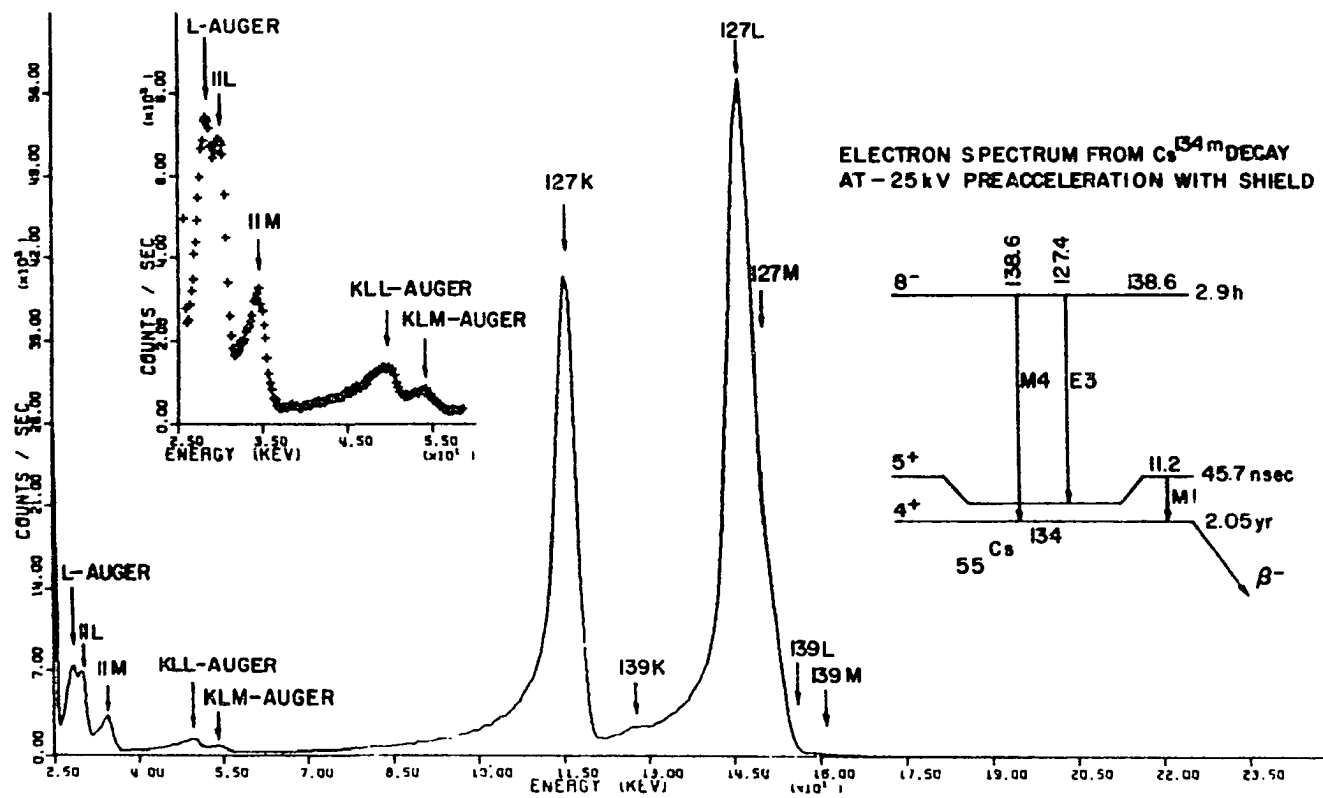


Fig. 26. An electron spectrum obtained from the  $\text{Cs}^{134\text{m}}$  decay. (The source was at a potential of -25 kV. A source shield screen was used for this data.)

Table 13. Summary of quantities calculated in the maximum-likelihood fit of an exponential plus constant background to the tail portion of delayed-coincidence distributions involving the lifetime of the 11-keV level in  $\text{Cs}^{134}$  obtained from the  $\text{Cs}^{134\text{m}}$  decay

| Delay Tag | Constant Background | Initial Height | Half-Life (nsec)  | Normalized Weight | Normalized Chi Square | Degrees Freedom | Probability $\chi^2 > \chi^2_{(\text{OBS})}$ | $\sqrt{\text{Variance of Fit}}$ |
|-----------|---------------------|----------------|-------------------|-------------------|-----------------------|-----------------|--|---------------------------------|
| 700A      | $1911 \pm 5$        | $8817 \pm 40$  | $45.92 \pm 0.260$ | 2.72              | 0.74                  | 164             | 0.99   | 42                              |
| 700B      | $396 \pm 2$         | $6273 \pm 30$  | $45.86 \pm 0.230$ | 3.45              | 0.78                  | 164             | 0.98   | 21                              |
| 701       | $23060 \pm 24$      | $17199 \pm 89$ | $47.14 \pm 0.428$ | 1.00              | 0.75                  | 113             | 0.98   | 145                             |
| 702       | $1678 \pm 7$        | $6853 \pm 36$  | $45.92 \pm 0.345$ | 1.53              | 0.63                  | 113             | 0.99   | 38                              |

Table 14. Summary of quantities calculated in the linear least-squares fit to the logarithms of the tail portion, after subtraction of a constant background, of delayed-coincidence distributions involving the lifetime of the 11-keV level in  $\text{Cs}^{134}$  obtained from the  $\text{Cs}^{134\text{m}}$  decay

| Delay Tag | Constant Background | Half-Life (nsec)  | Normalized Weight | Normalized Chi Square | Degrees Freedom | Probability $\chi^2 > \chi^2_{(\text{OBS})}$ | $\sqrt{\text{Variance of Fit}}$ | Delay Counts |
|-----------|---------------------|-------------------|-------------------|-----------------------|-----------------|--|---------------------------------|--------------|
| 700A      | 1939                | $45.24 \pm 0.626$ | 2.10              | 0.95                  | 164             | 0.65   | 48                              | 229282       |
| 700B      | 399                 | $45.76 \pm 0.536$ | 2.87              | 0.78                  | 164             | 0.98   | 21                              | 166673       |
| 701       | 23243               | $45.06 \pm 0.907$ | 1.00              | 1.25                  | 113             | 0.04   | 187                             | 499433       |
| 702       | 1680                | $45.77 \pm 0.742$ | 1.49              | 0.64                  | 113             | 0.99   | 38                              | 205616       |

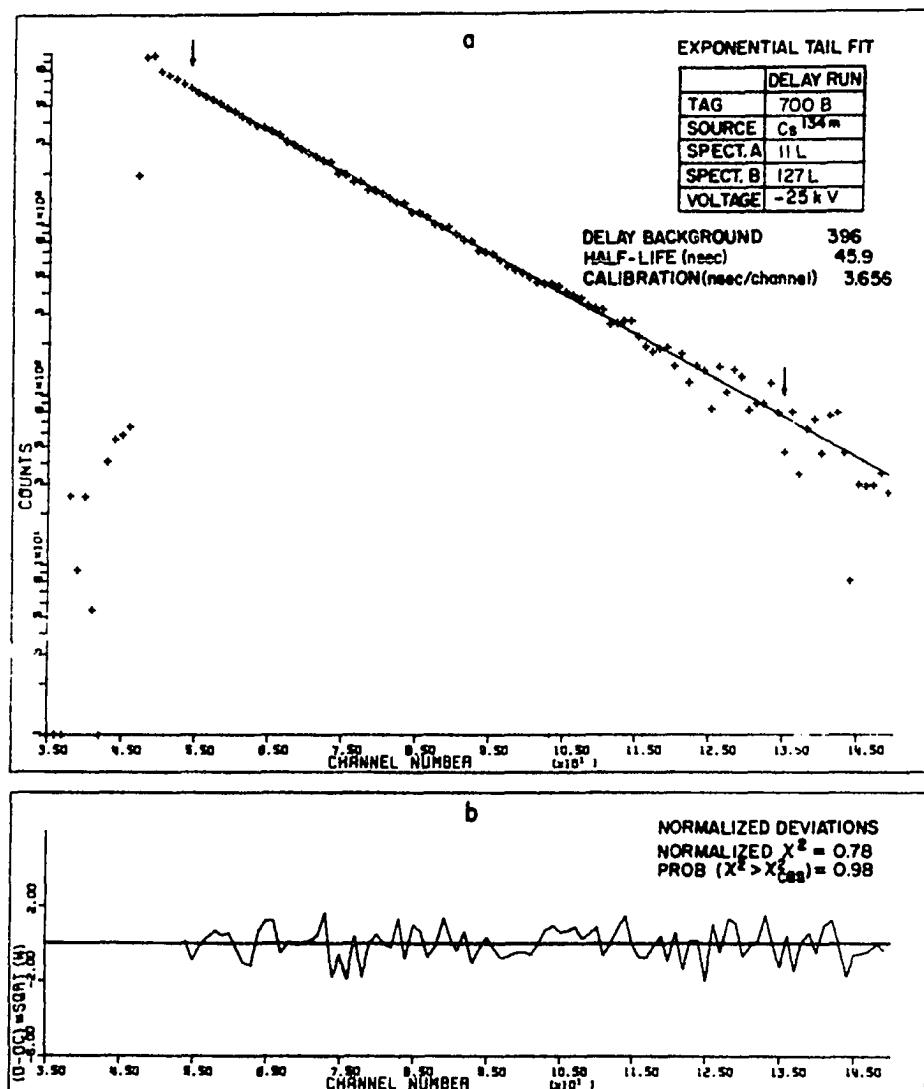


Fig. 27. Delay curve for the 11-keV level in  $\text{Cs}^{134}$  via the 11L and 127L transitions in the  $\text{Cs}^{134\text{m}}$  decay. (a. Plus signs represent the delay data minus background. The line is the calculated exponential component of the fit to the tail of the delay data. The arrows indicate the region used for logarithmic slope analysis. The left arrow also locates the lower channel limit for the exponential fit, the other limit is off scale to the right. b. The normalized deviations from the data of the composite fit.)



the logarithms of the tail portion of the  $\text{Cs}^{134}$  delayed-coincidence distributions after subtraction of a constant background.

The individual half-life results obtained by the different analysis procedures were averaged. These averages are given in Table 15 along with various statistical quantities. A comparison of the  $\text{Cs}^{134}$  results in Table 15 with the  $T_m^{169}$  and  $T_m^{171}$  results in Tables 5 and 11 gives no indication of a significant systematic high or low trend associated with any of the analysis methods. The adopted value is, therefore, taken to be the weighted average of the results of the different methods calculated as indicated in Table 15.

The final value adopted for the half-life of the 11-keV level in  $\text{Cs}^{134}$  is  $(45.7 \pm 1.2)$  nsec. The error assignment is the sum of the estimated limit of systematic error, 0.5 nsec, and the computed standard error, 0.7 nsec. The systematic 1.1% error limit is the root-sum-square of the following:

- 1) a 0.10% error limit for the time calibration and linearity correction (see Sections III.D.7. and III.D.8.),
  - 2) a 0.06% error limit representing the difference between the exponential fit results obtained with and without the use of a channel-width-error term in the weighting formula for a typical set of data, and
  - 3) a 1.13% error limit representing the difference between the half-life results obtained by the different analysis methods (see Table 15).
- The computed standard error is the product  $3.2 \times 0.20$  where 3.2 is Student's  $t$  for 3 degrees of freedom and a 95% confidence interval, and where 0.20 is the estimated standard deviation in the weighted average

Table 15. Comparison of the average half-life values and statistical quantities associated with the different analysis procedures for the four delayed-coincidence distributions involving the lifetime of the 11-keV level in Cs<sup>134</sup>

| Analysis Procedure  | UNWTAV <sup>a</sup><br>(nsec) | WTAV <sup>b</sup><br>(nsec) | SIGUU <sup>c</sup>              | SIGWW <sup>d</sup> | SIGMUU <sup>e</sup> | SIGMWW <sup>f</sup> | SUMW <sup>g</sup> | SIGMSW <sup>h</sup> |
|---|-------------------------------|-----------------------------|---------------------------------|--------------------|---------------------|---------------------|-------------------|---------------------|
| Maximum Likelihood Exponential Plus Constant Tail Fit     | 46.21                         | 46.04                       | 0.617                           | 0.458              | 0.309               | 0.229               | 47.49             | 0.145               |
| Linear Least-Squares Fit to The Logarithmic Slope of Tail | 45.46                         | 45.52                       | 0.363                           | 0.337              | 0.181               | 0.168               | 9.060             | 0.332               |
| Weighted Average  |                               | 45.70 <sup>i</sup>          | Standard Deviation <sup>j</sup> |                    | 0.199               |                     |                   |                     |

<sup>a</sup>Unweighted average of half-life values.

<sup>b</sup>Weighted average of half-life values.

<sup>c</sup>Unweighted standard deviation of values from the unweighted average.

<sup>d</sup>Weighted standard deviation of values from the weighted average.

<sup>e</sup>Standard deviation in the unweighted mean of four values ( $SIGUU/\sqrt{4}$ ).

<sup>f</sup>Standard deviation in the weighted mean of four values ( $SIGWW/\sqrt{4}$ ).

<sup>g</sup>Sum of the unnormalized weights used to determine the weighted average.

<sup>h</sup>Standard deviation in the weighted average calculated from  $1/\sqrt{SUMW}$ .

<sup>i</sup>Weighted average of the WTAV values; weights used were based on the SIGMWW values.

<sup>j</sup>Estimated standard deviation is unweighted average of the SIGMWW values.

calculated as indicated in Table 15.

The deviations of the results obtained with D701 from the final weighted average were somewhat higher than observed for the other data sets. This is undoubtedly due to the high count rates associated with the thick source (see Section III.D.1.) which gave a very poor true to accidental coincidence ratio (T/A). The initial singles count rates for D701 were  $\approx 80$  kHz in the START channel (127L line) and  $\approx 3.5$  kHz in the STOP channel (11L line). The STOP channel rate was sufficiently low that no deviation from a constant background would be expected due to Poisson statistics (see reference (86)) on a  $1.0 \mu\text{sec}$  TAC range. However, the START channel rate was high enough to cause concern about instrumental effects. In spite of the poor T/A rates and possible rate-dependent instrumental effects the deviations were nearly within the final error assignment. This fact indicates that rate effects were ordinarily negligible.

The distribution D702 was obtained after the thick source had decayed to more reasonable count rates. The half-life results from this run were much closer to the final value. This fact provides some evidence that possible source thickness influence on the lifetime was probably negligible for all the other sources used in this work since they were much thinner (see Section III.D.1.).

The elimination of D701 from the weighted averages has negligible effect on the final value obtained.

A comparison of the result of this investigation with the values obtained by other experimenters is shown in Fig. 28. The numerical values are also tabulated in Table 16. The order of presentation is

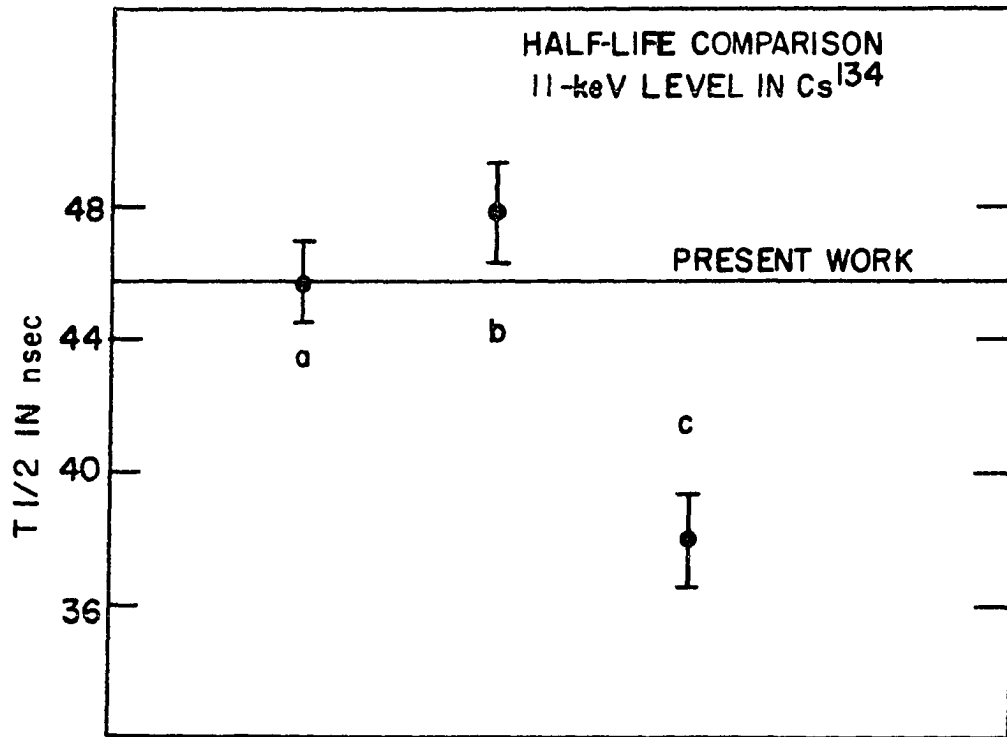


Fig. 28. Comparison of the half-life values of the 11-keV level in Cs<sup>134</sup> reported by different experimenters. (a. Present work, b. Lynch and Glendenin (98), and c. Blehschmidt et al. (94). The horizontal line indicates the value obtained in the present work.)

reverse chronological in both cases. Measurement 2 was made with back-to-back NaI(Tl) scintillation counters; measurement 3 was made with a parallel-plate avalanche counter opposite a scintillation counter. The present work is in fair agreement with measurement 2 by Lynch and Glendenin but disagrees with measurement 3 by Blechschmidt et al.

Table 16. Half-life values of the 11-keV level in Cs<sup>134</sup> reported by different experimenters

| Measurement | Half-life<br>(nsec) | Experimenters                   |
|-------------|---------------------|---------------------------------|
| 1           | $45.7 \pm 1.2$      | Present work                    |
| 2           | $47.8 \pm 1.5^a$    | Lynch and Glendenin (98)        |
| 3           | $37.9 \pm 1.4$      | Blechschmidt <u>et al.</u> (94) |

<sup>a</sup>The error was recalculated on the basis of a 95% confidence interval with the statistical error of 0.48% and the systematic error of 0.97% given in (98).

The general observations given in Section IV. A. regarding possible systematic errors apply also to measurement 3.

In the recent measurement by Lynch and Glendenin the NaI (Tl) scintillators provided adequate energy resolution but gave a rather broad, asymmetric, and tailing prompt curve which could conceivably produce a slope lifetime result a few percent high. Also the calibration method which was based on the accidental-coincidence distribution requires precise rate measurements corrected for deadtime effects and appears to have more potential for systematic error than the electronic method used in the present investigation. In addition, the statistical

accuracy of the present data is superior to that of Lynch and Glendenin.

In view of the precision of the present measurements and the considerable care taken to optimize system performance and to eliminate possible sources of systematic error it is believed that the value reported here is correct.

#### D. Indication of a Systematic Discrepancy

Besides the present investigation only two groups have measured more than one of the lifetimes studied here.

Begzhanov et al. (91) measured the half-lives of the first excited states in  $\text{Tm}^{169}$  and  $\text{Tm}^{171}$ . For  $\text{Tm}^{169}$  Begzhanov et al. obtained a value higher by a factor  $1.27 \pm 0.08$  than that of the present work. For  $\text{Tm}^{171}$  they report a value lower than that of the present investigation by a factor  $0.60 \pm 0.06$ . This inconsistency is not readily explained.

Blechsmidt et al. (94) have reported values for all three of the lifetimes studied in this work. The thesis of Blechsmidt (46) is the only source of information on the experimental work. Figure 29 presents the ratios of the values obtained by Blechsmidt et al. for the 8.4-keV level in  $\text{Tm}^{169}$ , the 5.0-keV level in  $\text{Tm}^{171}$ , and the 11-keV level in  $\text{Cs}^{134}$  to the corresponding values obtained in this investigation. The numerical values are tabulated in Table 17. It is seen that the differences between the two groups of measurements can be represented by a constant factor,  $0.80 \pm 0.03$ . The fact that the present results for the two Tm isotopes disagreed with Blechsmidt et al. by nearly a constant factor prompted the present measurement of the lifetime of the 11-keV level in  $\text{Cs}^{134}$  which provides further evidence of a systematic discrepancy.

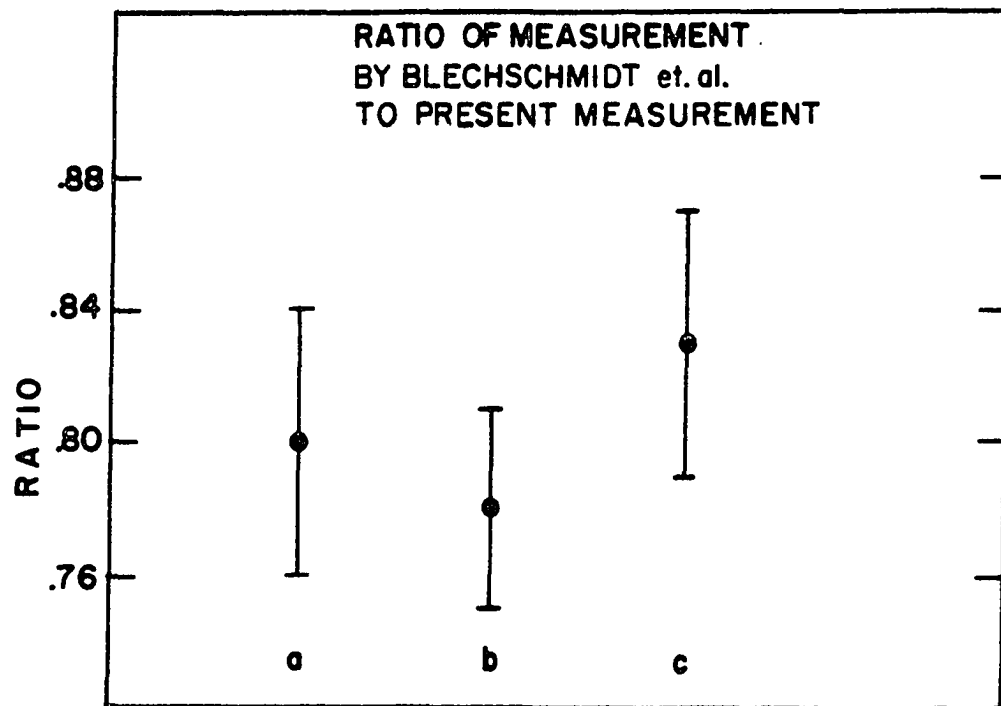


Fig. 29. Discrepancies between the measurements by Blechschiidt et al. and the present measurements (a. 8.4-keV level in  $\text{Tm}^{169}$ , b. 5.0-keV level in  $\text{Tm}^{171}$ , and c. 11-keV level in  $\text{Cs}^{134}$ )

Table 17. Ratios of the half-life values obtained by Blechschmidt et al. (94) to the corresponding values obtained in the present investigation

| Isotope               | Ratio                   |
|-----------------------|-------------------------|
| $Tm^{169}$            | $0.80 \pm 0.04$         |
| $Tm^{171}$            | $0.78 \pm 0.03$         |
| $Cs^{134}$            | $0.83 \pm 0.04$         |
| Weighted Average 0.80 | Standard Deviation 0.03 |

The most obvious source of a constant systematic discrepancy is the time calibration. The time calibration used in this investigation was carefully checked by two completely independent methods which gave results in agreement within error (see Section III.D.7.). The time calibration in the work of Blechschmidt (46) was obtained with calibrated delay cables. The propagation velocity specified by the manufacturer was checked but the method used was not indicated. Even if the cables were calibrated using the frequency-dependent standing wave method an error of 20% would not be likely. Therefore, the source of the constant factor discrepancy remains uncertain.



## V. DISCUSSION OF THE RESULTS

In this section is discussed the determination of the electromagnetic properties of a  $K = 1/2$  rotational band within the context of the unified model of Nilsson for odd-A deformed nuclei. The parameters determined in recent least-squares fits to the data of the ground state bands of  $\text{Tm}^{169}$  and  $\text{Tm}^{171}$  are used to calculate predicted values of the Tm level lifetimes investigated in this work. The general utility of a more accurate determination of the electromagnetic properties of the two  $K = 1/2$  bands considered is indicated. The desirability and feasibility of better lifetime measurements for some of the higher excited states in the two  $K = 1/2$  bands is noted. Also a recent calculation of the lifetime of the 11-keV level in  $\text{Cs}^{134}$  is noted.

### A. The $K = 1/2$ Rotational Bands

Two of the lifetime measurements reported in this work concern the first excited states in the odd-A deformed nuclei,  $\text{Tm}^{169}$  and  $\text{Tm}^{171}$ . In both cases the level investigated is a member of the  $K = 1/2$  ground-state rotational band based on the  $1/2 + [411]$  Nilsson single-particle orbital. Therefore, the electromagnetic properties are described by the four parameters  $g_R$ ,  $g_K$ ,  $b_0$ , and  $Q_0$  within the context of the unified model as indicated in Section II.

In principle, the four electromagnetic parameters can be determined from four suitably chosen measurements which are described by independent model equations. However, the situation is complicated by the large number of quantities that have been measured in both nuclei. In each case these measurements include at least three each of the following: magnetic

moments, lifetimes, mixing ratios, and transition- or gamma-intensity ratios. Thus the parameters are highly overdetermined. Further difficulty is presented in some cases by conflicting results which arise from unknown systematic errors in the measurements.

One approach to the problem of parameter determination is to perform a least-squares fit to all the experimentally measured quantities where conflicting measurements are averaged and a larger error assigned to the result. The quality of the fit could most likely be improved if some of the conflicting measurements could be eliminated in an unbiased manner. Ordinarily the wide range of sophisticated techniques applied to the various measurable quantities would make this impossible or highly impractical without effective collaboration of experts even if sufficient experimental detail was available. As a result dubious measurements are often incorporated into the fit.

In spite of these difficulties Kaufmann et al. (99) have recently determined parameters for the  $K = 1/2$  ground state rotational bands in  $Tm^{169}$  and  $Tm^{171}$  by means of least-squares fits to most of the available data. The parameters determined are capable of reproducing the experimental values with fair accuracy. At least one measurement that is probably incorrect was included in each of the fits. However, the resultant parameters should not be highly sensitive to one or two bad data. This assumption is reinforced by the fact that in a few cases subsequent measurements agree better with the fit predictions than the previous measurements. It is, therefore, suitable to compare the present lifetime measurements with the model predictions using parameters determined by Kaufman et al.

The least-squares fits of Kaufman et al. were performed in two ways. In the first fit the model equations were identical to those given in Section II. The second fit used model equations which were similar to those in Section II except for the incorporation of a spin-dependent quadrupole moment correction term which could arise if there were other single-particle configurations admixed into the  $1/2 + [411]$  orbital. Initial indications of a better fit with the inclusion of the quadrupole moment correction term were removed "in proof" because of more recent data. Hence, only the parameters determined by constraining the quadrupole correction to zero will be considered here. The investigation of possible quadrupole moment corrections requires data of better accuracy than is presently available and would be desirable.

#### 1. The 8.4-keV level in $Tm^{169}$

From the partial decay scheme given in Fig.10 it is seen that the 8.4 keV transition proceeds from the  $3/2+$  level to the  $1/2+$  level and should therefore be mainly an M1 transition with a possible E2 admixture. Thus the half-life can be determined from the model parameters by combining Equations 17 and 30. In addition to the magnetic parameters  $g_R$ ,  $g_K$ , and  $b_0$  one needs the transition energy and intensity, the mixing ratio, and the total internal conversion coefficient.

Since only the 8.4-keV transition depopulates the  $3/2+$  state,  $I_j = 1$ . The most accurate determination of the transition energy is  $(8.401 \pm 0.008)$  keV (100). An E2 admixture of  $(0.108 \pm 0.005)\%$  has been determined by Carlson et al. (100) from the M-subshell ratios in conjunction with the theoretical M-subshell internal conversion coefficients of Hager and Seltzer (101). From the data of Carlson et al. the total- to M- conversion ratio can be

determined to be

$$\frac{\alpha_{8.4}}{\alpha_M} \approx \frac{\alpha_M + \alpha_N + \alpha_0}{\alpha_M} = 1.24 \pm 0.02. \quad (41)$$

Combining this result with the theoretical value of  $\alpha_M^1$  obtained for the admixture given above yields  $\alpha_{8.4} = 266 \pm 11$ . The error in  $\alpha_{8.4}$  has been obtained by adding a 2% allowance for "systematic error" in the theoretical calculation to the quadratically combined errors associated with  $\delta^2$  and  $\alpha/\alpha_M$ .

The values of the magnetic parameters for  $Tm^{169}$  obtained by Kaufmann et al. with no quadrupole moment correction are given in Table 18. These values were used to predict the half-life of the 8.4-keV level. The calculated value and the result of the present experiment are in good agreement:

$$T_{1/2} = (4.15 \pm 0.20) \text{ nsec, model prediction;}$$

$$T_{1/2} = (4.04 \pm 0.06) \text{ nsec, present experiment.}$$

The error indicated on the model calculation is the result of application of the standard formulas for error propagation. Comparison with Table 6 shows that only three of the eight measurements agree with the model prediction, the present measurement, that by McAdams et al. (35), which was performed independently in this laboratory, and the first reported measurement by Beekhuis and de Waard (95), which has a rather

---

<sup>1</sup>The theoretical internal conversion coefficients were determined by interpolation in the tables of reference (101) using the computer program listed therein.

larger error assignment.

Table 18. The "best-fit" electromagnetic parameters of the  $K = 1/2$  ground state rotational band in  $\text{Tm}^{169}$  and  $\text{Tm}^{171}$  obtained by Kaufmann et al. (99) with no quadrupole moment correction

| Parameter | $\text{Tm}^{169}$         | $\text{Tm}^{171}$         |
|-----------|---------------------------|---------------------------|
| $g_R$     | $0.403 \pm 0.006$         | $0.398 \pm 0.028$         |
| $g_K$     | $-1.62 \pm 0.02$          | $-1.49 \pm 0.04$          |
| $b_o$     | $-0.142 \pm 0.005$        | $-0.18 \pm 0.02$          |
| $Q_o$     | $7.67 \pm 0.06 \text{ b}$ | $7.93 \pm 0.17 \text{ b}$ |

In another recent analysis of the electromagnetic properties of the ground state rotational band in  $\text{Tm}^{169}$  by Günther et al. (102) the life-times were excluded from the fit because it was felt that the uncertainty in the total conversion coefficients of the low energy M1 transitions was too large. This conclusion was based on the fact that an experimental determination by Känkeleit et al. (103) of the total conversion coefficient of the 8.4 keV transition using Mössbauer methods gave a result of  $\alpha = 325 \pm 35$  which is high compared to the semi-theoretical value,  $\alpha_{8.4} = 266 \pm 11$ , used above. The fact that a more recent Mössbauer determination by Wagner (104) gave  $\alpha = 220 \pm 50$  was apparently not taken into account. In view of the good subshell ratio fits obtained with the theoretical conversion coefficients of Hager and Seltzer, e.g. Carlson et al. (100), and lack of any evidence of discrepancy it is generally believed that the theoretical calculations are accurate to within two percent (105). For these reasons the exclusion of the life-times from the parameter fitting process seems unwarranted.

With the parameters determined by a fit to the data exclusive of the lifetimes, Gunther et al. calculated the half-life of the 8.4-keV level to be  $T_{1/2} = (4.85 \pm 0.28)$  nsec. An error of 5% was assumed for the semi-theoretical conversion coefficient. This  $T_{1/2}$  value is much too high. The lifetimes calculated for the other levels were also high. Much better agreement between the calculated and experimental lifetimes is provided by the parameters of Kaufmann et al. if one replaces the weighted average,  $(3.75 \pm 0.18)$  nsec, used for the 8.4-keV level half-life by the result of the present investigation.

## 2. The 5.0-keV level in $Tm^{171}$

The situation in the case of the 5.0-keV level in  $Tm^{171}$  is exactly analogous to that of the 8.4-keV level in  $Tm^{169}$  as can be seen by comparing the partial decay schemes in Fig. 10 and Fig. 18. The half-life predicted by the model can be calculated in exactly the same manner.

Since only the 5.0-keV transition depopulates the  $3/2^+$  state,  $I_j = 1$ . The most accurate determination of the transition energy is  $(5.025 \pm 0.006)$  keV (97). The most recent experimental value of the mixing ratio is  $\delta^2 = (0.042 \pm 0.007)\%$ . This value is the weighted average of two values obtained from remeasurement of the M-subshell ratios by Geiger et al. (106). The subshell ratios are  $M_{11}/M_1 = 0.39 \pm 0.03$  and  $M_{111}/M_1 = 0.42 \pm 0.04$ . The errors in the subshell ratios are statistical only. The error in the weighted average was assigned by the author to be the same percent error as was reported for a previous measurement (97). Since the error assigned is slightly greater than the change in the value it should adequately allow for possible systematic error.

The ratio  $\alpha/\alpha_M$  has not been experimentally determined for the 5.0

keV transition. However, the ratio generally has been found (105) to be  $1.24 \pm 0.02$  for a number of transitions of widely different  $Z$ , various energies, and several multiplicities including M1 and E2. It is convincing to note that  $\alpha/\alpha_M = 1.24 \pm 0.02$  for the 8.4-keV transition in  $Tm^{169}$  (100) and  $\alpha/\alpha_M = 1.25 \pm 0.03$  for the 21-keV transition in  $Tm^{169}$  (102). Therefore, the value  $\alpha/\alpha_M = 1.24 \pm 0.02$  is used for the 5.0 keV transition in  $Tm^{171}$ . Combining this value with the theoretical value of  $\alpha_M$  obtained for the mixing ratio given above yields  $\alpha_{5.0} = 1287 \pm 110$ . The error in  $\alpha_{5.0}$  was calculated in the same way as that in  $\alpha_{8.4}$ .

The values of the magnetic parameters for  $Tm^{171}$  obtained by Kaufmann et al. (99) with no quadrupole moment correction and the initial set of mixing ratios of Geiger et al. (97) are given in Table 18. These values were used to predict the half-life of the 5.0-keV level which was not included in the fit. The calculated value and the result of the present experiment are in good agreement:

$$T_{1/2} = (5.06 \pm 0.57) \text{ nsec, model prediction;}$$

$$T_{1/2} = (4.77 \pm 0.08) \text{ nsec, present experiment.}$$

The error indicated on the model calculation is the result of application of the standard formulas for error propagation. The higher percent error in this case is due partly to the greater errors in the magnetic parameters but mostly due to the 17% error in  $\delta^2$ . Comparison with Table 12 shows that only the present measurement of the 5.0-keV level lifetime agrees with the model prediction.

### 3. The utility of better accuracy

In Sections V.A.I. and V.A.II. it has been shown that the present

experimental measurements of the half-lives of the  $3/2^+$  excited states in  $\text{Tm}^{169}$  in  $\text{Tm}^{171}$  agree well with predictions based on the appropriate "best-fit" magnetic parameters,  $g_R$ ,  $g_K$ , and  $b_0$ , in conjunction with experimental mixing ratios and semi-theoretical internal conversion coefficients. These results and those of Günther et al. (102) for  $\delta^2(7/2 \rightarrow 5/2)$  and  $\delta^2(5/2 \rightarrow 3/2)$  in  $\text{Tm}^{169}$  improve the overall agreement with experiment provided by the fits of Kaufmann et al. (99). The general agreement verifies the approximate validity of the unified model equations at least from a phenomenological point of view.

In spite of the reasonable agreement between experimental values and the "best-fit" parameters of Kaufmann et al. (99) is worth noting that the experimental accuracy is still lacking in some respects. Hsu (107) has calculated the  $Q_0$  associated with the various individual rotational transitions in the  $K = 1/2$  bands of  $\text{Tm}^{169}$  and  $\text{Tm}^{171}$ . The range of  $Q_0$  values obtained is about 13 percent of the average in each case and the typical error on an individual determination is about 7 percent. If the rotational model is valid,  $Q_0$  should be constant so these variations may indicate that one or more values of the lifetimes, mixing ratios, branching ratios, or internal conversion coefficients is not sufficiently accurate. On the other hand Bohr and Mottelson have indicated (108) that the coupling of rotational and intrinsic motion implies a spin-dependent term in the expression for the  $K = 1/2$  reduced E2 transition probability which may amount to as much as 10 percent. Obviously, data of better accuracy is necessary to investigate this possibility. As was noted earlier Kaufmann et al.



found no evidence for such a quadrupole correction within the accuracy of the available data.

The need for increased accuracy also appears when one attempts to explain difficulties that arise in the comparison of the intrinsic parameters  $\underline{a}$ ,  $g_K$ , and  $b_0$  calculated from the Nilsson wave functions with the experimental values. Such a comparison is a sensitive test of the accuracy of Nilsson's Hamiltonian and wave functions.

One of the rather interesting inconsistencies that has been investigated concerns the experimental values of  $\underline{a}$  in contrast to the location of the excited intrinsic states  $7/2 + [404]$  and  $7/2 - [523]$  in  $\text{Tm}^{169}$  and  $\text{Tm}^{171}$ . The experimental values of  $\underline{a}$  fit by Hsu (107) are  $-0.77831 \pm 0.00015$  and  $-0.86276 \pm 0.0001$  for the  $1/2 + [411]$  bands of  $\text{Tm}^{169}$  and  $\text{Tm}^{171}$ , respectively. The values of  $\underline{a}$  calculated on the basis of the Nilsson wave functions are a function of the deformation parameter and the experimental values would imply a decrease in deformation from  $\text{Tm}^{169}$  to  $\text{Tm}^{171}$  (see reference (109)). On the other hand the intrinsic states  $7/2 + [404]$  at 316.2 keV and  $7/2 - [523]$  at 379.3 keV in  $\text{Tm}^{169}$  go over to 635.4 keV and 424.8 keV, respectively, in  $\text{Tm}^{171}$ . The change in energy separations and inversion of order of the excited intrinsic states would seem to require an increase in deformation (110).

This paradoxical behavior has been treated with moderate success by Feifrlík (110) by introduction of an interaction between quasi-particles which renormalizes the matrix element  $\langle K = 1/2 | j_+ | K = -1/2 \rangle$ . Hsu (107) introduced a short range force between the odd proton and extra two neutrons in  $\text{Tm}^{171}$  as a perturbation to the Nilsson Hamiltonian

and was able to obtain semiquantitative explanation of the behavior of  $\underline{a}$  and the level separations. He also was able to predict small changes in  $g_K$  and  $b_0$  but these are inconclusive due to inadequate experimental precision.

As is seen from Equations 10 and 11 the extraction of the experimental longitudinal and transverse spin g-factors implies knowledge of  $a$ ,  $g_K$ , and  $b_0$ . Bochnacki and Ogaza ( 5 ) have predicted values of the effective spin g-factors. Presently there is disagreement with the experimentally determined values, however, it appears that the difficulty may lie in the method of extraction of the experimental values (99). In view of the rather active interest in spin polarization effects ( 4 , 5 , 111, 112, 113 ) it is not unlikely that better extraction methods will be devised which will make accurate intrinsic parameter values desirable.

The intrinsic quadrupole moment  $Q_0$  depends on the distribution of charge within the nucleus via the intrinsic wave functions. Its calculation should, in principle, be able to yield valuable information about nuclear structure provided that the experimental and calculational accuracy match. The calculation of some quadrupole moments has been performed which would benefit from accurate experimental  $Q_0$  values. (114).

The collective gyromagnetic ratio  $g_R$  depends on the magnetic properties associated with the collective flow and gives a direct measure of the relative superfluidity of the proton system compared to that of the neutron system (115 ). The calculation of  $g_R$  depends on various assumptions about nuclear structure so that comparison of

theoretical values such as those of Prior et al. (115) with accurate experimental values is of some interest.

It should be apparent that there exists a wide variety of theoretical investigation which depends on accurate knowledge of the electromagnetic properties of the  $K = 1/2$  band in  $Tm^{169}$  and  $Tm^{171}$  as well as other nuclei for verification.

In future least-squares determinations of the electromagnetic parameters of the  $1/2 + [411]$  bands of  $Tm^{169}$  and  $Tm^{171}$  it is believed that the superior apparatus, the precision and statistical accuracy of the results, and the considerable care exercised to avoid systematic error justify the use of the lifetimes of the  $3/2+$  levels reported here rather than weighted averages of values that are quite likely to involve unknown systematic error.

#### 4. Some especially desirable measurements

It has been pointed out by Hsu (107) and is repeated here in the hope of stimulating some interest that the half-life of the 116-keV level in  $Tm^{171}$  appears to be too low for a consistent  $Q_0$  value throughout the  $K = 1/2$  band. Hsu suggested that a value of  $(68 \pm 3.4)$  psec would be more reasonable than the reported value of  $(55 \pm 13)$  psec (116).

In view of the stability of modern electronics and the advent of sophisticated time pickoff, stabilization, and pileup rejection circuitry and accurate data analysis techniques it seems that it would be very useful to have a single group carefully remeasure the lifetimes of the  $5/2+$  and  $7/2+$  states in  $Tm^{169}$  and  $Tm^{171}$ . This is especially true of the short-lived  $5/2+$  states which were measured

at a time when electronic equipment was most likely less stable than that presently available.

In addition it would be very desirable to have a more accurate value of the mixing ratio of the 5.0-keV transition in  $\text{Tm}^{171}$ . There is some indication that even the revised value (106) may be too low. The feasibility of obtaining better accuracy is uncertain, however, due to source thickness difficulties.

#### B. The Odd-Odd Nucleus $\text{Cs}^{134}$

As was indicated in Section IV.D. the measurement of the lifetime of the 11-keV level in  $\text{Cs}^{134}$  was undertaken to check out an indication of a constant factor discrepancy between the present Tm isotope measurements and those of Blechschmidt *et al.* (94). During the course of this work the measurement of Lynch and Glendenin (98) appeared. As was shown in Fig. 28 the two measurements agree within error but the present value is slightly lower.

Lynch and Glendenin were able to get an estimate of the internal conversion coefficient which was in agreement with the theoretical value obtained from the tables of Hager and Seltzer (101). They also reported an estimate by D. Kurath based on the odd-group model originally introduced by Schwartz (117). The calculated radiative mean life was  $\tau = 4040$  nsec while their measured value was 7314 nsec. Obviously, the theoretical accuracy is not sufficient at present to cause concern about the 4.6% difference between the present measurement and that of Lynch and Glendenin.

## VI. BIBLIOGRAPHY

1. A. Bohr and B. R. Mottelson, Kgl. Danske Videnskab, Mat.-Fys. Medd. 27, No. 16 (1953).
2. S. G. Nilsson, Kgl. Danske Videnskab, Mat.-Fys. Medd. 29, No. 16 (1955).
3. O. Nathan and S. G. Nilsson, "Collective Nuclear Motion and the Unified Model." In K. Siegbahn, ed., Alpha-, Beta- and Gamma-Ray Spectroscopy (North Holland Publishing Co., Amsterdam, Netherlands, 1965), Vol. I, Chap. X, p. 601.
4. Z. Bochnacki and S. Ogaza, Nucl. Phys. 69, 186 (1965).
5. Z. Bochnacki and S. Ogaza, Nucl. Phys. 83, 619 (1966).
6. S. A. Moszkowski, "Theory of Multipole Radiation." In K. Siegbahn, ed., Alpha-, Beta- and Gamma-Ray Spectroscopy (North Holland Publishing Co., Amsterdam, Netherlands, 1965), Vol. II, Chap. XV, p. 863.
7. A. Z. Schwarzschild and E. K. Warburton, Ann. Rev. Nucl. Sci. 18, 265 (1968).
8. R. E. Bell, "Coincidence Techniques and the Measurement of Short Mean Lives." In K. Siegbahn, ed., Alpha-, Beta- and Gamma-Ray Spectroscopy (North Holland Publishing Co., Amsterdam, Netherlands, 1965), Vol. II, Chap. XVII, p. 905.
9. A. Krusche, D. Bloess, and F. Münnich, Nucl. Instr. and Meth. 51, 197 (1967).
10. F. W. Büsser, J. Christiansen, H. P. Hermsen, F. Niebergall, and G. Söhngen, Z. Physik 187, 243 (1965).
11. K. W. Dolan, J. P. Hurley, and J. M. Mathiesen, Nucl. Instr. and Meth. 39, 232 (1966).
12. M. Bonitz, W. Meiling, and F. Stary, Nucl. Instr. and Meth. 29, 309 (1964).
13. G. Bellettini, C. Bemporad, C. Cerri, and L. Foà, Nucl. Instr. and Meth. 27, 38 (1964).
14. L. G. Hyman, R. M. Schwarcz, and R. A. Schluter, Rev. Sci. Instr. 35, 393 (1964).

15. G. Bellettini, C. Bemporad, C. Cerri, and L. Foà, Nucl. Instr. and Meth. 21, 106 (1963).
16. M. Bertolaccini, C. Bussolati, S. Cova, S. Donati, and V. Svelto, Nucl. Instr. and Meth. 51, 325 (1967).
17. G. Bertolini, V. Mandl, A. Rota, and M. Cocchi, Nucl. Instr. and Meth. 42, 109 (1966).
18. G. Bertolini, M. Cocchi, V. Mandl, and A. Rota, Proc. IEEE Trans. Nucl. Sci. NS-13, 119 (1966).
19. G. Present, A. Schwarzschild, I. Spirn, and N. Wotherspoon, Nucl. Instr. and Meth. 31, 71 (1964).
20. D. L. Smith, R. G. Polk, and T. G. Miller, Nucl. Instr. and Meth. 64, 157 (1968).
21. F. T. Porter, M. S. Freedman, F. Wagner, Jr., and I. S. Sherman, Nucl. Instr. and Meth. 39, 35 (1966).
22. I. S. Sherman, M. S. Freedman, F. T. Porter, and F. Wagner, Jr., Proc. IEEE Trans. Nucl. Sci. 11, 20 (1964).
23. W. C. Kaiser and J. A. M. de Villiers, Proc. IEEE Trans. Nucl. Sci. 11, 29 (1964).
24. M. F. McCann and K. M. Smith, Nucl. Instr. and Meth. 65, 173 (1968).
25. J. H. Neiler and P. R. Bell, "The Scintillation Method." In K. Siegbahn, ed., Alpha-, Beta- and Gamma-Ray Spectroscopy (North Holland Publishing Co., Amsterdam, Netherlands, 1965), Vol. 1, Chap. V, p. 245.
26. G. J. Hine and J. A. Cardarelli, Nucleonics 18, 92 (1960).
27. F. Du Chaffaut, P. Charmet, and R. Trabaud, Nucl. Instr. and Meth. 65, 285 (1968).
28. P. G. Sjölin, Nucl. Instr. and Meth. 63, 253 (1968).
29. J. Kirkbride, E. C. Yates, and D. G. Crandall, Nucl. Instr. and Meth. 52, 293 (1967).
30. P. G. Sjölin, Nucl. Instr. and Meth. 37, 45 (1965).
31. I. B. Berlman and O. J. Steingraber, Proc. IEEE Trans. Nucl. Sci. 11, 27 (1964).

32. G. Walter and A. Coche, Proc. IEEE Trans. Nucl. Sci. 11, 44 (1964).
33. K. Siegbahn, "Beta-Ray Spectrometer Theory and Design. Magnetic Alpha-Ray Spectroscopy. High Resolution Spectroscopy." In K. Siegbahn, ed., Alpha-, Beta- and Gamma-Ray Spectroscopy (North Holland Publishing Co., Amsterdam, Netherlands, 1965), Vol. 1, Chap. III, p. 79.
34. R. E. McAdams and E. N. Hatch, U.S. Atomic Energy Commission Report IS-1071 (1965).
35. R. E. McAdams, G. W. Eakins, and E. N. Hatch, Nucl. Phys. 82, 449 (1966).
36. S. G. Malmskog, Arkiv Fysik 35, 255 (1967).
37. P. Sparrman, A. Märelus, and J. Lindskog, Arkiv Fysik 32, 429 (1966).
38. J. S. Geiger, R. L. Graham, I. Bergström, and F. Brown, Nucl. Phys. 68, 352 (1965).
39. W. C. Parker and H. Slätis, "Sample and Window Technique." In K. Siegbahn, ed., Alpha-, Beta- and Gamma-Ray Spectroscopy (North Holland Publishing Co., Amsterdam, Netherlands, 1965), Vol. 1, Chap. VII, p. 379.
40. A. Ogata, S. J. Tao, and J. H. Green, Nucl. Instr. and Meth. 60, 141 (1968).
41. C. M. Lederer, J. M. Hollander, and I. Perlman, Table of Isotopes (John Wiley & Sons, Inc., New York, 1967), 6th ed.
42. O. C. Kistner, A. C. Li, and S. Monaro, Phys. Rev. 132, 1733 (1963).
43. Y. Y. Chu, O. C. Kistner, A. C. Li, S. Monaro, and M. L. Perlman, Phys. Rev. 133, B1361 (1964).
44. O. C. Kistner, S. Monaro, and A. Schwarzschild, Phys. Rev. 137, B23 (1965).
45. D. Bloess, A. Krusche, F. Münnich, Z. Physik 192, 358 (1966).
46. H. Blechschmidt, Lebensdauer-messungen an den untersten Anregungsniveaus von Tm<sup>169</sup>, Tm<sup>171</sup> und Cs<sup>134</sup> unter Verwendung von Parallelplatten-Lawinenzählern. Unpublished M.S. thesis, Universität Hamburg, Germany, 1961.
47. D. Bloess and F. Münnich, Z. Naturforsch. 18a, 1028 (1963).

48. K. Siegbahn, ' $\beta$ -Ray-Spectrometer Theory and Design. High Resolution Spectroscopy.' In K. Siegbahn, ed., Beta- and Gamma-Ray Spectroscopy (North Holland Publishing Co., Amsterdam, Netherlands, 1955), Chap. III, p. 52.
49. P. Sparman, J. Lindskog, and A. Märelius, Nucl. Instr. and Meth. 41, 299 (1966).
50. J. Lindskog, P. Sparman, A. Märelius, and T. Sundström, Arkiv Fysik 32, 417 (1966).
51. P. Sparman, Nucl. Instr. and Meth. 41, 305 (1966).
52. A. Bäcklin, B. Fogelberg, V. Berg, and S. G. Malmeskog, Nucl. Phys. A138, 429 (1969).
53. R. T. Nichols, A. V. Pohm, J. H. Talboy, Jr., and E. N. Jensen, U.S. Atomic Energy Commission Report ISC-345 (1953).
54. R. T. Nichols, A. V. Pohm, J. H. Talboy, Jr., and E. N. Jensen, Rev. Sci. Instr. 26, 580 (1955).
55. G. Schupp and E. N. Hatch, U.S. Atomic Energy Commission Report IS-590 (1963).
56. P. A. Tove, Rev. Sci. Instr. 27, 143 (1956).
57. T. R. Gerholm, Rev. Sci. Instr. 26, 1069 (1955).
58. M. Bonitz, W. Meiling, and F. Stary, Nucl. Instr. and Meth. 29, 314 (1964).
59. E. Breitenberger, Progr. Nucl. Phys. 4, 56 (1955).
60. R. A. Schrack, H. T. Heaton, II, and R. B. Schwartz, Nucl. Instr. and Meth. 77, 175 (1970).
61. S. J. Tao, J. Bell, and J. H. Green, Nucl. Instr. and Meth. 35, 222 (1965).
62. J. E. Griffin and W. W. Souder, Nucl. Instr. and Meth. 64, 80 (1968).
63. J. Lindskog and T. Sundström, Arkiv Fysik 24, 199 (1963).
64. H. Schneider and C. Weingardt, Nucl. Instr. and Meth. 40, 305 (1966).
65. J. Lindskog, K-G. Väliivaara, Z. Awwad, S-E, Hägglund, A. Märelius, and J. Phil, Nucl. Phys. A137, 511 (1969).



66. R. L. Graham, J. S. Geiger, R. E. Bell, and R. Barton, Nucl. Instr. and Meth. 15, 40 (1962).
67. J. Glatz, Nucl. Instr. and Meth. 79, 277 (1970).
68. S. Cova and M. Bertolaccini, Nucl. Instr. and Meth. 77, 269 (1970).
69. J. F. Boulter, W. V. Prestwich, and T. J. Kennett, Nucl. Instr. and Meth. 77, 163 (1970).
70. J. F. Boulter, W. V. Prestwich, and B. Arad, Can. J. Phys. 47, 591 (1969).
71. F. A. Johnson, Nucl. Instr. and Meth. 59, 237 (1968).
72. C. A. Baker, C. J. Batty, and L. E. Williams, Nucl. Instr. and Meth. 59, 125 (1968).
73. A. Langsford and P. E. Dolley, Nucl. Instr. and Meth. 59, 120 (1968).
74. Z. H. Cho, L. Gidefeldt, and L. Eriksson, Nucl. Instr. and Meth. 52, 273 (1967).
75. C. Hatcher, E G & G Nanonotes, Vol. 1, No. 2, Jan., 1964.
76. H. de Waard and H. Beekhuis, "Method for Calibrating and Testing Time to Pulse Height Converters." In P. H. Steilson, ed., Electromagnetic Lifetimes and Properties of Nuclear States. Proc. 1961 Gatlinburg Conf. (NAS-NRC, Wash., D.C., 1962), Publ. 974, p. 71.
77. P. Thieberger, Arkiv Fysik 22, 127 (1962).
78. W. O. Olson, H. H. Hubbel, Jr., and R. D. Birkhoff, U.S. Atomic Energy Commission Report ORNL-2569 (1958).
79. M. S. Freedman, F. T. Porter, F. Wagner, Jr., and P. P. Day, Phys. Rev. 108, 836 (1957).
80. E. Gatti and V. Svelto, Nucl. Instr. and Meth. 43, 248 (1966).
81. R. E. Bell, Nucl. Instr. and Meth. 42, 211 (1966).
82. Ortec, Inc., "Timing with Ge(Li) Detectors." Ortec, Inc. (Oak Ridge, Tenn.) Application Note 31 (1970).
83. M. Cocchi and A. Rota, Nucl. Instr. and Meth. 55, 365 (1967).

84. S. Donati, E. Gatti, and V. Svelto, Nucl. Instr. and Meth. 77, 179 (1970).
85. Yu. K. Akimov and S. V. Medved, Nucl. Instr. and Meth. 78, 151 (1970).
86. C. E. Turner, Jr., submitted to Nucl. Instr. and Meth.
87. C. E. Turner, Jr., U.S. Atomic Energy Commission Report IS-2253 (1970).
88. C. E. Turner, Jr. and R. A. Anderl, submitted to Nucl. Instr. and Meth.
89. R. A. Anderl and C. E. Turner, Jr., submitted to Nucl. Instr. and Meth.
90. R. A. Anderl and C. E. Turner, Jr., U.S. Atomic Energy Commission Report IS-2339 (1970).
91. R. B. Begzhanov, Kh. M. Sadykov, R. Kh. Safarov, Izv. Akad. Nauk Uzbek SSR, Ser. Fiz.-Mat. Nauk 1, 45 (1967).
92. T. Sundström, P. Sparman, J. O. Lindström, and J. Lindskog, Phys. Letters 6, 56 (1963).
93. U. Hauser, E. N. Hatch, K. Runge, G. Knissel, and G. Schneider, "Measurements of E1 Transition Probabilities in Several Deformed Odd-A Nuclei as a Study of Single Particle Motion." In P. H. Stelson, ed., Electromagnetic Lifetimes and Properties of Nuclear States. Proc. 1961 Gatlinburg Conf. (NAS-NRC, Wash., D.C., 1962), Publ. 974, p. 230.
94. H. Blechschmidt, J. Christiansen, H. P. Hermsen, Physik Verhandl. 11, 185 (1961).
95. H. Beekhuis and H. de Waard, Physica 24, 767 (1958).
96. P. Stephas and B. Crasemann, Phys. Rev. 164, 1509 (1967).
97. J. S. Geiger, R. L. Graham, and M. W. Johns, Bull. Am. Phys. Soc. 13, 672 (1968).
98. F. J. Lynch and L. E. Glendenin, Phys. Rev. 186, 1250 (1969).
99. E. N. Kaufmann, J. D. Bowman and S. K. Bhattacharjee, Nucl. Phys. A119, 417 (1968).
100. T. A. Carlson, P. Erman, and K. Fransson, Nucl. Phys. A111, 371 (1968).

101. R. S. Hager and E. C. Seltzer, Nucl. Data A4, 1 (1968).
102. C. Günther, H. Hubel, A. Kluge, K. Krien, and H. Toschinski, Nucl. Phys. A123, 386 (1969).
103. E. Kankeleit, F. Boehm, and R. Hager, Phys. Rev. 134, B747 (1964).
104. F. E. Wagner, Z. Physik 210, 361 (1968).
105. G. T. Emery (private communication, May, 1970).
106. R. L. Graham (private communication, April, 1970).
107. H. H. Hsu, Ph.D. thesis, Indiana University, 1970 (unpublished).
108. A. Bohr and B. R. Mottelson, Sov. Atom. Energy 14, 36 (1963).
109. B. R. Mottelson and S. G. Nilsson, Z. Physik 141, 217 (1955).
110. V. Feiflik, Izv. Akad. Nauk SSSR, Ser. Fiz. 30, 501 (1966) [English transl.: Bull. Acad. Sci. (USSR) 30, 510 (1966)].
111. Z. Bochnacki and S. Ogaza, Acta Phys. Polon. 27, 649 (1965).
112. Z. Bochnacki and S. Ogaza, Acta Phys. Polon. 31, 51 (1967).
113. Z. Bochnacki and S. Ogaza, Report No. 482/PL, Institute of Nuclear Research, Cracow (1966).
114. L. Yuan and C. Liang-Yuan, Zh. Eksperim. i Teor. Fiz. 42, 1219 (1962) [English transl.: Sov. Phys.—JETP 15, 845 (1962)].
115. O. Prior, F. Boehm, and S. G. Nilsson, Nucl. Phys. A110, 257 (1968).
116. T. Sundström, J. O. Lindström, P. Sparman, and J. Lindskog, Arkiv Fysik 26, 397 (1964).
117. C. Schwartz, Phys. Rev. 94, 95 (1954).

## VII. ACKNOWLEDGEMENTS

The author would like to express sincere appreciation to Dr. E. N. Hatch for his suggestion of the measurements presented in this dissertation and for his continued interest, encouragement, and support throughout the course of this project.

The author is also grateful to Dr. D. J. Zaffarano for his advice, confidence, and support, especially in the latter stages of this work.

Special thanks are also expressed to Mr. Robert Anderl for his invaluable assistance in taking and analyzing the preliminary data mentioned in Section X. and for his dedicated effort in the development of the sophisticated numerical analysis techniques for unfolding complex delayed-coincidence distributions.

Gratitude is also extended to: Mr. George Eakins for his help in the tedious task of source preparation and general assistance. Mr. Christian Weber for his skillful and ready assistance in electronic trouble-shooting and his design of the spectrometer current programmer. Mr. Roland Struss and Mr. Harold Skank for assistance in the design of the source rod. The Ames Laboratory Instrumentation Group for design, construction, maintenance, and calibration of various essential electronic equipment. The staff of the Ames Laboratory Research Reactor and the Health Physics Division of the Ames Laboratory for their assistance with source irradiations and handling. Mr. Kenneth Malaby for advice on the chemical aspects of source preparation. Dr. R. C. Lamb for the loan of much essential nanologic electronic instrumentation. Dr. G. T. Emery for valuable discussions regarding theoretical internal conversion coefficients and the total-conversion to M-conversion ratio. Dr. R. L. Graham for

providing the most recent results of M-subshell ratio measurements at Chalk River on the 5.0-keV transition in  $\text{Tm}^{171}$  prior to publication.

Finally, thanks are also given to the many unnamed individuals whose cooperation and concern aided the successful completion of this work.

## VIII. APPENDIX A: CALIBRATION OF THE SPECTROMETER

The method used to calibrate the magnetic spectrometer is indicated here briefly. The relationships among the spectrometer current and the momentum, total energy, and kinetic energy of the electron are given in Section III.D.3. (Equations 31, 33, and 34).

The calibration was obtained in the region 0 to 150 keV by use of the accurately known energies (41) of the internal conversion lines in the  $\text{Yb}^{169}$  decay. The  $\text{Yb}^{169}$  conversion lines are conveniently spaced in this region (see Fig. 30). For the operating resolution of 2% it was quite sufficient to locate the conversion line by the current corresponding to the peak count rate.

An unweighted linear least-squares fit was made to the known momenta and experimentally determined current locations of the well resolved  $\text{Yb}^{169}$  conversion lines in order to determine the constants  $\underline{a}$  and  $\underline{b}$  in Equation 31.

Fig. 30a shows a calibration scan for the low-energy-channel spectrometer. No preacceleration voltage was applied, of course. The baffle settings and source size and centering were the same as used in all the measurements described in this work. The calibration was established to be  $\eta = 0.110 \pm 0.010$ . The same data plotted versus electron kinetic energy is shown in Fig. 30b.

Fig. 30 is useful for comparing the momentum and energy resolutions which are related according to Equation 35. It can also be used to give a rough indication of the spectrometer currents associated with various conversion lines used in the present lifetime measurements. In the

current range involved in the present measurements the long term current stability was better than  $\pm 5$  milliamperes.

The spectrometer current was obtained by measuring the voltage drop across a precision 0.01 ohm resistor with an integrating digital voltmeter<sup>1</sup> (DVM) capable of at least five digit accuracy. The input impedance was  $10^6$  ohm for the 1 volt scale. The calibration of the DVM was checked periodically by the Ames Laboratory Instrumentation Group.

---

<sup>1</sup>Dymec, Model 2401B. (Input impedance  $1M\Omega$  on the 1V scale.)

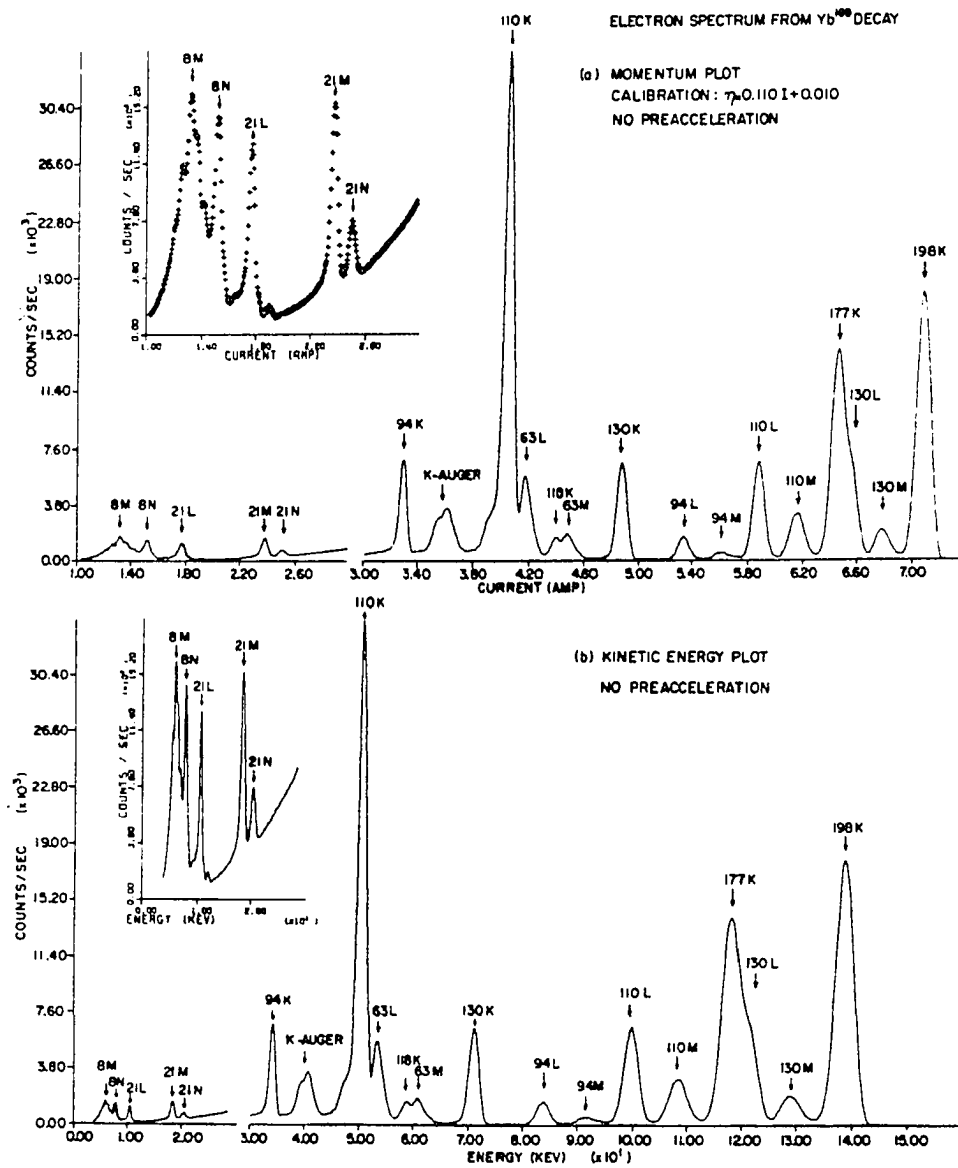


Fig. 30. Low-energy-channel spectrometer energy-calibration spectrum. (The calibration spectrum obtained from the  $\text{Yb}^{169}$  decay is plotted versus current in (a) and versus the deduced energy scale in (b). No preacceleration voltage was used.)



## IX. APPENDIX B: CALIBRATION OF THE HIGH VOLTAGE SUPPLY

In order to determine whether the energy shift of the electrons emitted by the radioactive source corresponded precisely to the applied source potential throughout the range of the Yb<sup>169</sup> conversion lines it was necessary to determine the calibration of the preacceleration voltage supply<sup>1</sup> to an accuracy of about one percent. This was accomplished by means of an accurately measured high voltage attenuator using an integrating digital voltmeter<sup>2</sup> (DVM).

In order to minimize attenuation ratio drifts due to thermal and voltage effects the attenuator was made with wirewound resistors. Two tubular high voltage resistors<sup>3</sup> each specified to be 20 megohms  $\pm$  1% and rated for 20 kV were used in series with a standard wirewound resistor specified to be 10 kilohms  $\pm$  1% to give an attenuation ratio of approximately 4000:1.

The attenuation ratio was measured accurately by placing a highly regulated 300 V power supply<sup>4</sup> across the attenuator. The supply voltage and the attenuated voltage across the 10 kilohm resistor were measured with the DVM and the ratio provided the attenuation ratio.

The preacceleration voltage supply helipot control was calibrated in approximately 5 kV increments from 0 to 35 kV. The preacceleration voltage supply output was connected across the attenuator for approximately twenty minutes to allow for thermal stabilization before the attenuated

---

<sup>1</sup> Specifications were indicated in Section III.C.

<sup>2</sup> Dymec, Model 2401B.

<sup>3</sup> Weston Electrical Inst. Corp., Newark, N.J.

<sup>4</sup> Ames Laboratory Instrumentation Group Design.

voltage measurements were made. The attenuation ratio was remeasured as soon as possible for each dial setting. In this manner a dial calibration reproducible and accurate to about one percent was established.

X. APPENDIX C: ESTIMATION OF TRANSIT  
TIME DISPERSION IN A CYLINDRICAL LIGHT PIPE

Consider a point source of isotropic light on the axis at one end of a cylindrical light pipe of length  $l$  and diameter  $d$ . Assume all light is lost except that which enters the pipe initially and is totally reflected. Assume also that all light which strikes the light pipe sides at an angle with the surface normal greater than  $\theta_c \equiv \arcsin(\frac{1}{n})$ , where  $n$  is the index of refraction of the pipe, is totally reflected with 100% efficiency. It is easily shown from the equality of the angles of incidence and reflection and geometrical considerations that the path length from the source to the exit face of the pipe for a reflected ray having an angle of emission  $\theta$  with the axis of the pipe is given by

$$p(\theta) = \frac{l}{\cos \theta} \quad . \quad (42)$$

This path length is identical to that of an undeflected ray from the source to the exit plane of the pipe. The result is easily verified from symmetry considerations. Note that the result is independent of the diameter regardless of whether the reflection is total or not.

The amount of light emitted at an angle between  $\theta$  and  $\theta + d\theta$  is proportional to the solid angle

$$d\Omega = 2\pi \sin \theta d\theta. \quad (43)$$

Note that this distribution is definitely not Gaussian. Only angles  $\theta$  between 0 and  $\pi/2 - \theta_c \equiv \theta_0$  result in total reflection. The mean path length is defined as

$$\bar{p} \equiv \frac{\int_0^{\theta_c} p(\theta) d\Omega}{\int_0^{\theta_c} d\Omega} \quad (44)$$

Using Equations 42 and 43 gives

$$\bar{p} = \frac{\ell \cdot \log_e (\sin \theta_c)}{\sin \theta_c - 1}, \quad (45)$$

or

$$\bar{p} = \ell \cdot \frac{n \log_e n}{n - 1} \quad (46)$$

For  $n = 1.5$  one gets  $\bar{p} = 1.22 \ell$ .

The variance  $\sigma_\ell^2$  in the path length is defined as

$$\sigma_\ell^2 \equiv \frac{\int_0^{\theta_c} (p(\theta) - \bar{p})^2 d\Omega}{\int_0^{\theta_c} d\Omega} \quad (47)$$

By use of Equations 42, 43, and 46 one obtains

$$\sigma_\ell^2 = \ell^2 \left\{ n - \left( \frac{n \log_e n}{n - 1} \right)^2 \right\} \quad (48)$$

For  $n = 1.5$  there results  $\sigma_\ell^2 = 0.0204 \ell^2$  and the estimated standard deviation in the path length is  $\sigma_\ell = 0.143 \ell$ .

The estimated standard deviation in transit time is simply

$$\sigma_t = \sigma_\ell / v \quad (49)$$

where  $v$  is the velocity of light in the light pipe and is related to the velocity of light in vacuum  $c$  by

$$v = \frac{c}{n} . \quad (50)$$

Therefore,

$$\sigma_t = \frac{n}{c} \sigma_l . \quad (51)$$

For  $n = 1.5$ , one gets  $\sigma_t = 0.215 \text{ } \mu\text{/c}$ .

# XI. APPENDIX D: DEPENDENCE OF THE HALF-LIFE ON PREACCELERATION VOLTAGE

It is worth noting here that a preliminary investigation of the half-life of the 8.4-keV level in  $\text{Tm}^{169}$  was made for preacceleration voltages of 0 to 25 kV in 5 kV increments. This work was done before the advent of the stabilization scheme, pileup rejection, semiautomatic electronic calibration, linearity correction, solid-state preacceleration voltage supply, electron detection optimization, and source shield screen. At that time the  $2\tau_0$  was approximately 3 nsec.

A series of delayed-coincidence distributions were obtained from 8M-110L coincidences at the source voltages given above. Approximate prompt curves were obtained at the same source voltages from 21L-110L coincidences. Slope analysis of the delay curves gave lifetime results which varied by 20% in a monotonically decreasing fashion as the source voltage was increased from 0 to 25 kV.

It was observed that the prompt curves had tails, which became less noticeable at higher preacceleration voltages, on the side associated with the lower energy electrons. It was found that the prompt curve slope could be described by a two component exponential function on the side associated with the low energy transition. The main component corresponded to a half-life of about one nsec and accounted for over 93% of the events in all cases. The tail component corresponded to a half-life of about 6 nsec and involved from 7% to 2% of the events over the preacceleration range of 0 to 25 kV.

Subtraction of a rough estimate of the prompt admixture from the delay curves influenced the slope analysis in a negligible fashion. It

was felt, therefore, that the convolution of the tailing prompt curve with the proper decay distribution should explain the variation in the slope-analysis half-life results. For this reason the development of the numerical maximum-likelihood unfolding techniques was undertaken and pursued in parallel with efforts to improve the performance of the experimental system.

Unfolding analysis of the data described above eventually provided half-life results which varied randomly within a range of  $\pm 5\%$  about the average. This fact strengthened the hypothesis that the slope-analysis half-life variation was due to the time resolution function variation and not due to any true half-life modification associated with the application of an electrostatic potential to the source. The more accurate data in Table 2 of Section IV. A. give further evidence of the validity of this assumption for preacceleration voltages varying from -10.5 kV to -24 kV (see Table 1). For the later data the experimental conditions had been improved to the point that no significant variation of the half-life results obtained by different analysis methods was observed even for source voltages as low as -10.5 kV (cf. Tables 2, 3, and 4).

The prompt tailing can be explained from the nature of the pulse height distributions associated with the low-energy-electron detection during the preliminary investigation. At that time the photopeak was submerged in the low amplitude rise associated with the longer lived excited states of the scintillator. The trigger threshold was located in the low amplitude rise which was responsible for the tail component. The amount of prompt tailing decreased as the fraction of photopeak pulses above the trigger

threshold increased with increasing preacceleration voltage.

The results of the preliminary investigation of the half-life of the 8.4-keV level in  $\text{Tm}^{169}$  as a function of the preacceleration voltage were not used in the determination of the final value reported in this work. The preliminary result was in agreement with the final value reported in Section IV. A., but was excluded from the final determination because of the poorer precision of the individual values, the much larger uncertainty in the time calibration, the absence of nonlinearity correction, and the generally inferior experimental conditions as compared to those described in Sections III. C. and III. D.